Title: Emerging Metallic Systems for Additive Manufacturing: *In-situ* Alloying and Multi-metal Processing in Laser Powder Bed Fusion

Authors: S.L. Sing[+], S. Huang[+], G. D. Goh, G. L. Goh, C. F. Tey, J. H. K. Tan & W.Y. Yeong[*]

Singapore Centre for 3D Printing, School of Mechanical & Aerospace Engineering, Nanyang Technological University

[+]*These authors contributed equally to this review article*

[*]*Corresponding Author*
Designation:
Associate Professor, School of Mechanical and Aerospace Engineering, Nanyang Technological University, Singapore
Associate Chair (Students), School of Mechanical and Aerospace Engineering, Nanyang Technological University, Singapore
Programme Director (Aerospace and Defence), Singapore Centre for 3D Printing, Nanyang Technological University, Singapore
Deputy Director (Technical), HP-NTU Digital Manufacturing Corporate Lab, Nanyang Technological University, Singapore
Co-Director, NTU Institute for Health Technologies, Nanyang Technological University, Singapore
Email: wyyeong@ntu.edu.sg
Tel: (+65) 6790 5130

Contents

Abstract

While significant progress has been made in understanding laser powder bed fusion (L-PBF) as well as the fabrication of various materials using this technology, there is still limited adoption in the industry. One of the key obstacles identified is the lack of materials that can truly manufacture functional parts directly with L-PBF. This paper covers the emerging research on *in-situ* alloying and multi-metal processing. A comprehensive overview of the underlying scientific topics behind them is presented. The current state of research and progress from different perspectives (the materials and L-PBF processing parameters) are reviewed in order to provide a basis for follow-up research that leads to the development of these approaches. Defects, especially those associated with these two material processing routes, are also elucidated by discussing the mechanisms of their formation, including the main influencing factors, and the tendency to occur. Future research trends and potential topics are illustrated. The final part of this paper summarizes findings from this review and outlines the possibility of *in-situ* alloying and multi-metal processing using L-PBF.

Keywords: Additive manufacturing; 3D printing; Powder bed fusion; Selective laser melting; Processing parameters; *In-situ* alloying; Multi-material; Machine learning

1. Introduction

Laser powder bed fusion (L-PBF), also commonly known as selective laser melting (SLM), is an additive manufacturing (AM) technique [1, 2] that has shown promising potential when applied to alloys [3] and ceramics [4, 5]. It facilitates near-net-shape manufacturing as the process starts from the preparation of computer-aided design (CAD) data files which are subsequently aligned with processing parameters and meshed into two-dimensional (2D) stacked layers by computer software. The production process includes a loop of depositing layers of powder onto a substrate plate or previously processed layers, selectively melting the powder with a high energy laser beam

according to each layer profile, lowering the platform by one-layer thickness, and then recoating a new layer of powder. The process ends with the deposition and melting of the last sliced layer of the three dimensional (3D) components [6]. Figure 1 illustrates the schematic of L-PBF process and principles. The white fonts indicate the machine parts and the black ones are controllable parameters.

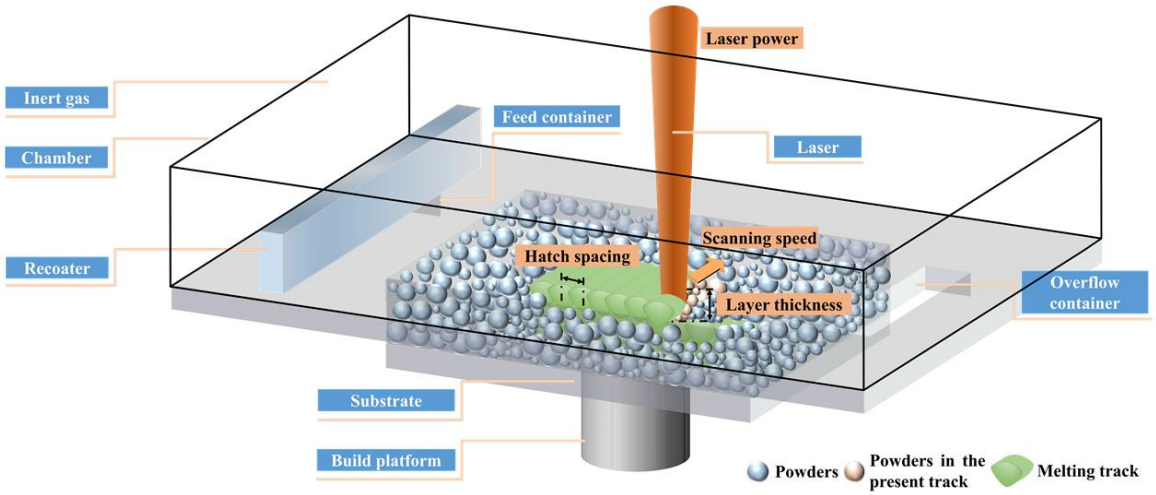

Figure 1 Schematic of SLM build chamber and process. The white fonts illustrate the machine components while the black fonts illustrate the key processing parameters [7].

L-PBF allows quick 3D printing of parts with complex geometries directly from powders without the time-consuming mold design process [8-11]. Near-net shape manufacturing makes them suitable for end applications or at least minimizes the extent of post-processing. However, polishing and heat treatment are sometimes essential for L-PBF parts [12]. L-PBF results in superior property in parts compared to counterparts produced by conventional methods due to the ultrafine and graded microstructure attributed to the rapid cooling and solidification cycles (with cooling rate of 10^3 to 10^6 $^oC/s$) during the process [13-15]. While L-PBF exhibits promising potential in the production of parts with unique structure and properties even with metallic glass

and metal matrix composite at a fair cost [16-19], there is still limited applications of this process in the industry. One of the main challenges is the limitation of materials available for L-PBF. As mentioned, there has been extensive work done on L-PBF processed materials, most of these alloys were designed for conventional methods. The widely known established materials for L-PBF are stainless steel, tool steel, Ti6Al4V, and AlSi10Mg. Hence, there is a need for new alloys designed specifically for L-PBF. The capability of L-PBF to process powder mixtures has opened new and exciting material research opportunities, especially for metal matrix composites which have been researched widely. "*In-situ* alloying" is a term coined for using L-PBF to simultaneously fabricate functional parts and to create alloys via mixed powder feedstock. This strategy has the potential for rapid design and verification of new alloys. Moreover, the functionality of a part typically requires more than one discrete material within the part. Hence, multi-metal processing is also an important function of L-PBF. While there are great promises, defects unique to LPBF remain a significant concern. These include rough surface, porosity, and residual stress, etc. Therefore, to achieve the L-PBF processing of multi-metal and *in-situ* alloying, a thorough understanding of both materials and L-PBF processing parameters is necessary.

Several reviews that focused on the knowledge of the L-PBF process of metals or alloys are available [20-23]. The usage of powder mixtures instead of pre-alloyed powder incur changes in the physical properties of materials, thus affecting the melt pool's thermal and rheological behavior, resulting in the shift of L-PBF processing window. A comprehensive understanding of the fabrication process and its relationship with part's performance is necessary, and this work seeks to gain a thorough understanding of the associated scientific and technological knowledge.

This review focuses on the state-of-the-art approaches within the perspectives of L-PBF, namely the *in-situ* alloying and multi-metal processing strategies. Other additive manufacturing

techniques are not within the scope of this review. Physical phenomena in L-PBF will first be introduced to offer a basic understanding of the scientific challenges of these two approaches. An in-depth review of the fabrication consideration related to *in-situ* alloying and multi-metal processing, including the materials and related processing parameters, is then presented. Emphasis on parts' physical properties and powder preparation techniques for *in-situ* alloying are placed in this review. The review also addresses the defects unique to L-PBF associated with these emerging materials systems. The final part of this paper outlines the potentials and challenges for future research in these areas.

2. Laser Powder Bed Fusion

L-PBF involves many physical phenomena such as absorption and reflection of laser radiation, heat transfers, phases transformation, fluid flow, vaporization, emission of materials, and chemical reactions. Concurrently, powder to liquid and liquid to solid transitions happens [24, 25]. It is crucial to understand these physical phenomena and their relations to the successful manufacturing of defect-free parts using L-PBF.

Heat absorption occurs during the interactions between laser and powder. Photons from a laser beam are reflected numerous times, however, only a small fraction of its energy is absorbed by the surface of the powder particles [26]. As such, the laser and powder characteristics are both critical in affecting the L-PBF melt pool formation and geometry [27]. The power density distribution of laser source which often follows axisymmetric Gaussian profile is given by:

$$P_d = \frac{fP}{\pi r_b^2} \exp\left(-f\frac{r^2}{r_b^2}\right) \quad (1)$$

where f is the distribution factor, P is the total power of the heat source, r_b is the radius of the heat source and r is the radial distance of any point from the axis of the heat source. From Equation (1), the laser type and laser diameter, also known as spot size, are accounted for by f and r_b,

respectively. These have been reviewed elsewhere [22]. As the laser characteristics are often not as easily varied as powder characteristics, due to them being machine-specific, emphasis in this discussion would only be placed on the controlled laser parameters such as power and scanning speed. It is interesting to note that the laser beam can penetrate deeper into a powder bed than into a bulk material of the same composition due to the multiple photons reflections and absorptions [28]. Laser and powder interactions for *in-situ* alloying and multi-metal processing during L-PBF will be further discussed in later sections.

Heat transfers including heat conduction, convection, and radiation, occurs simultaneously with fluid flow. Fluid flow can be explained using gravity, buoyancy, Marangoni flow, and vaporization. In L-PBF, Marangoni flow and vaporization are more significant than gravity and buoyancy, hence, the latter are less discussed [29]. Marangoni flow is surface tension driven [30-32] and happens due to the pulling of liquid with low surface tension towards liquid with higher surface tension. In the melt pool, temperature or composition gradients may generate surface tension difference which results in Marangoni flow [33]. As lasers with Gaussian profiles are typically used in L-PBF, the center of the melt pools has the highest temperature. Thus, the fluid flow within the melt pools tends to be radially outward [21]. Marangoni number *Ma*, which is used to measure the strength of the convective flow, is given below:

$$\mathrm{Ma} = -\frac{\mathrm{d}\gamma}{\mathrm{d}T}\frac{L\Delta T}{\mu\alpha} \tag{2}$$

where μ is the dynamic viscosity, α is the thermal conductivity of the material, L is the characteristics length of the melt pool (typically taken as the width of the melt pool), ΔT is the difference between the maximum temperature inside the pool and the solidus temperature of the material, and $\frac{\mathrm{d}\gamma}{\mathrm{d}T}$ is the sensitivity of the surface tension with respect to temperature.

The material vaporizes extensively when the temperature exceeds its boiling point, and the generated recoil pressures drive the fluid motion in return. High recoil pressure results in the removal of molten material by expulsion while low recoil pressure facilitates smoothing of the melt pool in L-PBF [34-36]. Keyhole mode is formed when high recoil pressure is exerted on the melt pool with the laser beam penetrating the material up to a certain layer thickness in L-PBF. Additionally, selective evaporation of volatile elements changes the local and global material composition [25, 37]. This is especially important for *in-situ* alloying and will be discussed in later sections.

It is important to understand the physical phenomena, hence, a thorough understanding of the variation in material properties due to the influence of processing parameters is important. The key processing parameters involved in L-PBF include laser power (P), scanning speed (v), hatch spacing (h), layer thickness (d). Extensive research has been carried out on various alloys to study their effect on part microstructures and properties [38-40]. The relationship between densification and processing parameters for *in-situ* alloying and multi-metal processing resembles the one in typical processing of pre-alloyed powders, except there are additional complications for the emerging systems. Such complications that are dependent on the processing parameters would be detailed in later sections.

The individual parameters P, v, h, and d can be combined into one equation:

$$\varepsilon = \frac{P}{v \cdot h \cdot d} \tag{3}$$

where ε represents volumetric energy density [41]. Since each material has specific laser absorbance and thermal properties, extensive experimental work must be carried out to obtain a processing window for new material systems that can lead to the production of parts with desired

properties. Due to the specific nature of these processing windows, performance degradation can occur if they are applied to other materials [42, 43].

Energy input determines the heat transition modes during L-PBF. Keyhole mode and/or conduction mode (Figure 2), distinguished by whether the boiling point is exceeded in the melt pools can occur during L-PBF. Also shown in Figure 2, a typical melt pool can be divided into three zones including deposition zone (DZ) on the top, re-melting zone (RZ) on the nether part, and heat-affected zone (HAZ) in the peripheral area of the melt pool. The length of RZ in keyhole mode is larger compared to conduction ones, penetrating deeper into the previous layers.

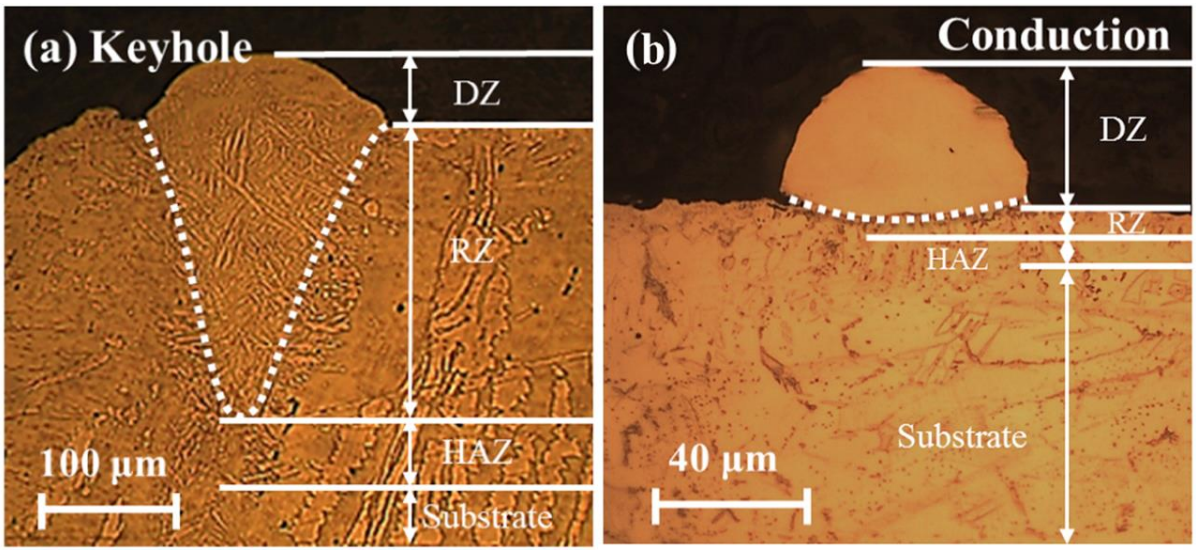

Figure 2 Macro-morphology of (a) keyhole and (b) conduction melt pools [44].

These two heat transition modes are related to the densification behavior in a L-PBF process. Yang *et al.* plotted a parameters map for high relative density parts and revealed a limited region for keyhole mode whilst a wide region for conduction mode [44]. Significant vaporization of materials and resultant keyhole pores lead to relatively high porosity for parts formed from keyhole mode. Stable melt tracks with fewer defects are more attainable in conduction mode. Yadroitsev *et al.* asserted that the maximum temperature of melt pools significantly increases with laser power and only slightly decreases with scanning speed [45]. However, Yang *et al.* investigated the

threshold for keyhole mode and highlighted the importance of laser energy density associated with scanning speed, laser power, and layer thickness, among which scanning speed is the most significant factor, followed by laser power and layer thickness [44]. Lower scanning speed indicates longer interactions between laser and materials with higher energy input which may facilitate keyhole mode. Higher laser power, which results in higher energy input per second, and thinner layer thickness, which results in lesser materials, show a similar tendency to facilitate keyhole mode [46]. Extremely low scanning speed, high laser power, and thin layer thickness result in instability of the scanning tracks. In such cases, L-PBF is accompanied by an increase of the melt volume but a decrease in the melt viscosity. Irregularity appears as the Marangoni effect becomes more significant. The vapor recoil pressure also results in distortion of the melt tracks. The irregularity of the melt tracks, which leads to poor powder depositions, and keyhole pores lead to low relative density. Overlapping hatches are expected to eliminate defects upon repeated re-melting of the part during subsequent laser scanning. Hatch spacing, which is the distance between the laser passes, is a significant variable in determining the energy density. Hence, the porosity and pore morphology vary due to different overlapping conditions of laser scanning tracks in L-PBF. Likewise, the layer thickness is essential to layer fusion and hence, relative density. When a thicker layer thickness is used, more input energy is needed in melting the powder particles and less heat is left for re-melting of the previous layer. This results in poorer interlayer bonding and more residual pores. Qiu *et al.* simulated melt pool behavior and asserted that the interaction between the laser beam and melt pool is particularly violent when thick powder layers were processed. This is characterized by significant melt splashing and the increased velocity of melt flow within the melt pools. The increase in porosity and surface roughness as a result of the increase in powder layer thickness is also validated by experiments [47].

Mishra *et al.* showed that there exists a simple linear relation of hatch spacing or layer thickness to the overlapping cross-sections of the melt pools and thus to the relative density [48]. Many research reported a direct increase in relative density with the hatch spacing or layer thickness [49-51]. However, in some research, there exists a threshold for hatch spacing [52, 53] and layer thickness [54, 55] respectively. Below this threshold, decreasing them would lower the relative density of the parts. Tang *et al.* established that sufficient overlap of melt pools to avoid incomplete melting is obtained if the following geometric criterion is fulfilled [56-58]:

$$\left(\frac{h}{W}\right)^2 + \left(\frac{d}{D}\right)^2 \leq 1 \quad (4)$$

where h is the hatch spacing, d is the layer thickness, W is the melt pool width, and D is the melt pool depth.

As concluded in research done by Yang *et al.*, high densification is more achievable in conduction mode as a wider region for parameter selection is available [44]. Nevertheless, careful optimization is necessary to avoid defects and imperfection.

The melt pool dimensions become too small when the wetting ability is not enough, the contact area between the melt pool and the substrate then becomes considerably limited. This leads to unfavorable wetting, flowing, and spreading characteristics. Melt pools with greater circumference-to-length ratios are supposed to show a more stable behavior [24, 59]. Therefore, balling occurs due to the longer melt pools which tend to become discontinuous with necking. This transition is also associated with laser power and layer thickness as they also affect the energy density. Lower laser power leads to lower energy input and resembles higher scanning speed. Although larger layer thickness enables a bigger melt pool [47, 54, 60], the melt pool is far away from the substrate, leading to a relatively smaller contact area between the melt pool and substrate that results in the balling effect. The balling effect would be discussed in later sections.

Detailed discussions about the formation of different regions within the process window of a material have been addressed elsewhere [22]. The determination of processing parameters for different alloys, during *in-situ* alloying and multi-metal processing, thus requires in-depth investigations and would be discussed in later sections.

3. *In-situ* Alloying using Laser Powder Bed Fusion

3.1 Aluminum and its Alloys

In-situ alloying of aluminium based alloys has been employed to accomplish several tasks. It has been mainly used for producing 3D printable aluminium alloys with low thermal expansion, crack-free, and can be age-hardened.

The addition of silicon into aluminium is known to improve its 3D printability by reducing the coefficient of thermal expansion (CTE). A study on eutectic Al12Si (wt%) has been done via *in-situ* alloying in which mixed elemental powder has been utilized [61]. The method of homogenizing the powder blend is by using a tumbling mixer. By adjusting the L-PBF parameters to manipulate the rate of cooling, silicon solubility in aluminium can be manipulated. X-ray diffraction (XRD) data shows that employment of low power or high scanning speed can lead to a faster cooling rate and improve silicon solubility (Figure 3).

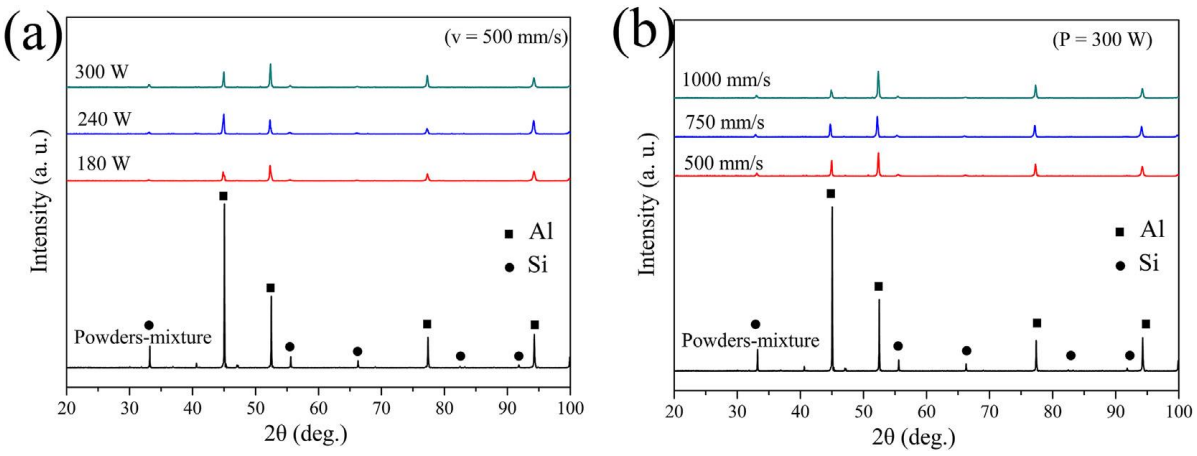

Figure 3 XRD analysis of the powder mixture and SLM processed samples with variations of (a) laser power and (b) laser scanning speed.[61]

The microstructure of this alloy mainly consists of aluminium rich α-Al phase and silicon phase. Fine microstructures can be seen but it becomes coarser with increasing energy density, ε (Figure 4). The coarsening mechanism can be attributed to nano-sized silicon agglomeration and rejection of silicon from aluminium due to longer melt pool retention. The tensile properties are highly dependent on the microstructure - low ε leads to crescent shape porosity while high ε leads to silicon agglomeration, both of which deteriorate the ultimate tensile strength (UTS) and ductility.

Meanwhile, *in-situ* alloyed Al18Si (wt%) was studied along with its wear properties. [62]. A maximum relative density of 96 % was obtained. Instead of using elemental power blend, pre-alloyed Al12Si (wt%) powder was mixed with silicon to obtain the desired composition. Part with best wear property was found to be those containing the most amount of nano-sized silicon. The wear resistance was found to be superior to that of hot extruded classical hypereutectic AlSiCu alloy [63]. Due to the *in-situ* alloying process, it is inevitable that either unmelted silicon or large silicon precipitates are formed when ε is too low or too high. The best wear resistance can be achieved when the porosity is reduced to a minimum and the majority of silicon are retained in nano-size. In a study, AlSi10Mg powder was blended with silicon powder to achieve the desired total silicon contents of 25 wt% (Al25Si) and 50 wt% (Al50Si) [64]. It is found that parts with high relative densities of more than 99 % can be achieved, however, the optimal processing parameters are dependent on the silicon content. Furthermore, considerable refinement of the microstructure and primary silicon particles have been achieved compared to cast materials. The tailorability of CTE with adjustment of silicon content has been shown. The CTE is reduced by 0.2×10^{-6} 1/K per wt% silicon, which gave a total CTE reduction of 43 % for Al50Si.

Contrary to conventional belief, there was an inverse relationship between wear resistance and primary silicon phase size. The larger silicon phase was speculated to form fine silicon particles layer due to cracking and dislodging when subjected to wear, acting like a shield [65]. It was shown that the primary silicon phase size is related to the cooling rate and a slow cooling rate leads to a larger primary silicon phase from L-PBF [66]. The same authors also subjected the *in-situ* alloyed Al50Si to heat treatment at a temperature between 300 and 600 ^{o}C, followed by water quench [67]. It was found that the porosity increases after a heat treatment at the temperature of 550 °C and 600 °C. Moreover, as-built Al50Si did not show a lamellar eutectic structure, but the characteristic eutectic structure appears after a heat treatment process at 600 ^{o}C (which is above the eutectic temperature). Like the effect of the sustained melt pool, heat treatment leads to silicon diffusion out from the supersaturated Al(Si) phase. With increasing heat treatment temperature, silicon crystallite size increases, and the mean residual stress was reduced. The observed silicon crystallite size as well as residual stress are also homogenized after heat treatment in all heat-treated samples.

As compared to pre-alloyed powder as feedstock, *in-situ* alloying of Al12Si requires higher ε to achieve similar relative density [68], possibly due to the positive enthalpy of formation. The highest relative density obtained via *in-situ* alloying (99 %) is still lower than that of pre-alloyed feedstock (99.5 %) for Al12Si used in the study. For parts of similar relative density, those produced via pre-alloyed feedstock possess finer cellular microstructure (Figure 4) [69], while *in-situ* alloyed ones have nano-sized agglomeration that resembles annealed parts (due to relatively higher energy density needed). The significant differences in melting point and positive enthalpy of formation between aluminium and silicon lead to the need for higher ε when *in-situ* alloyed, which can limit the type of obtainable microstructure due to the narrower processing window.

Moreover, the amount of unmelted silicon particles in *in-situ* alloyed part is more prominent (Figure 5). The effect of these unmelted particles is discussed in later sections.

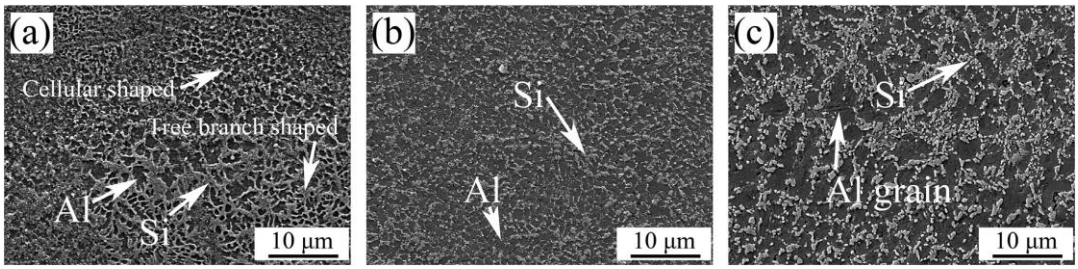

Figure 4 SEM images of microstructure of L-PBF processed Al-12Si with several laser power (a) 180 W, (b) 240 W and (c) 300 W. [61]

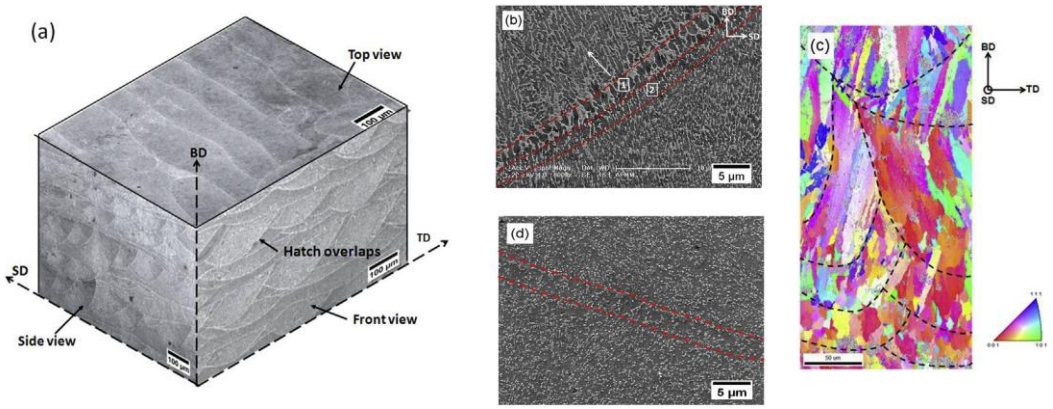

Figure 5 (a) Representative microstructure of the as a solidified alloy. The phase contrast in these microstructures is Si - grey and Al - white. (b) High magnification SEM image obtained on the BD-TD plane of the AS alloy, revealing cellular solidification within each of the laser melted pool. Hatch overlap region is marked by 1, and region 2 shows coarsening of Si phase just outside these overlaps. The phase contrast is Si -white and Al -grey. (c) Inverse pole figure map obtained on the BD-TD plane of the AS specimen. Black solid lines indicate some of the melt pool borders. (d) High magnification SEM image for the HS alloy (captured from the BD-TD plane), revealing a uniform distribution of Si particles [69].

Despite successes in printing AlSi based alloys that were originally designed for casting, wrought aluminium alloys remain a challenge to be processed with L-PBF. Wrought aluminium alloys (such as the 2000, 5000, 6000, and 7000 series) are highly in demand in the AM industry due to their strength as a result of precipitation hardening. The issue is that alloying components that enable precipitation hardening also leads to a larger solidification range in the wrought aluminium alloys. This subsequently leads to hot tearing during the solidification of columnar L-PBF parts due to epitaxial grain growth from the previous layer. Small equiaxed grains are

preferred over columnar grains for wrought aluminium parts produced by L-PBF to accommodate thermal contraction strain that leads to hot cracking. Nevertheless, the conquest usually revolves around material-specific parameters optimization. Achieving small equiaxed grains remains a challenge. Essentially, Martin *et al.* picked up the challenge of printing Al 7075 and 6061 by inducing heterogeneous nucleation sites to achieve equiaxial fine grains via the addition of 1 vol% nano-sized hydrogen stabilized zirconium [70]. Zirconium forms Al_3Zr nucleation phase when melted with aluminium which can act as nucleation sites. However, pre-alloying of wrought aluminium alloys with zirconium via gas atomization process cannot solve the challenge as rapid grain coarsening can occur during the atomization process. As such, *in-situ* alloying provides a viable alternative. The study by Martin *et al.* used electrostatic assembly technique of zirconium on pre-alloyed Al 7075 and 6061 powders to achieve homogenous mixture and prevent settling. Figure 6 shows the resultant particle after electrostatic assembly. The usage of pre-alloyed wrought aluminium alloy powder + 1 vol% zirconium resulted in crack-free Al 6061 (Figure 7) and Al 7075 (Figure 8) parts are also provided. Al 7075 was also fabricated with the addition of silicon to eliminate hot cracking [71]. The addition of 4 wt% silicon refines grains and lowers the CTE to achieve crack-free parts. Grains in the <200> orientation was reduced and superseded by the <111> orientation. However, hot cracking prevention via silicon addition is at the expense of ductility as compared to wrought Al 7075 that is not modified. Also, subsequent T6 heat treatment on the silicon modified Al 7075 dissolve the fine microstructure and deteriorates strength.

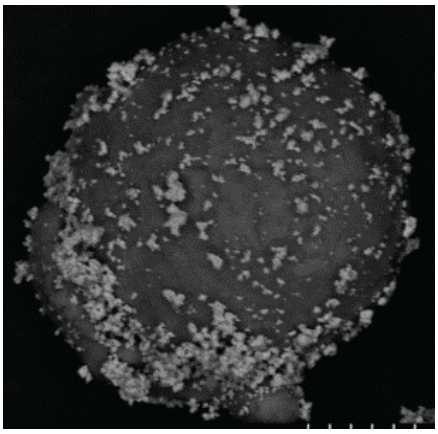

Figure 6 Nanoparticle Enhanced Powder (nano-sized Zr on wrought Al alloy powder) [70].

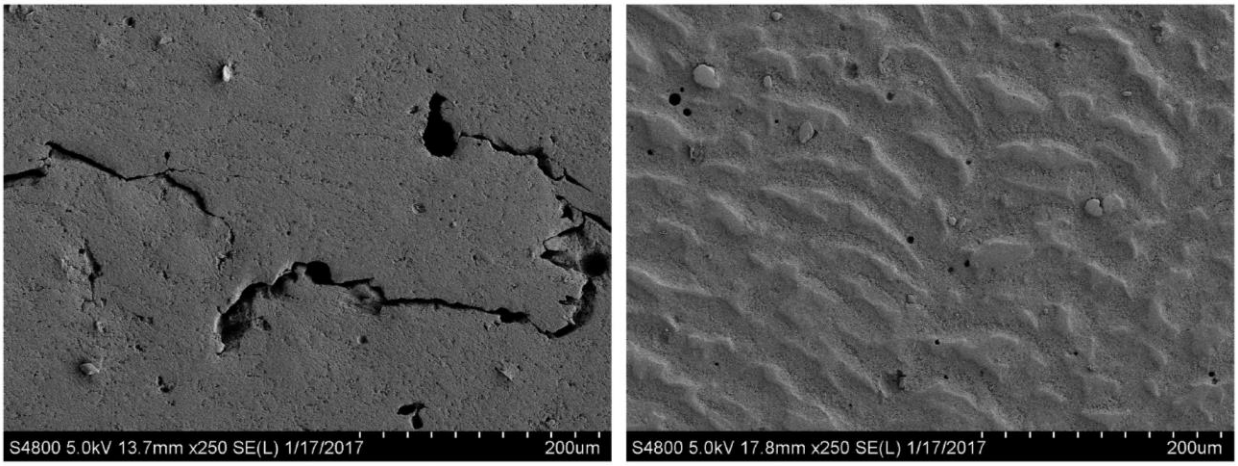

Figure 7 Micrographs of etched Al6061, processed as received. Large cracks are observed in the absence of Zr (left). With the addition of Zr nanoparticles, no cracking is observed, but there is some residual porosity (right). Rows indicate increasing magnification [70].

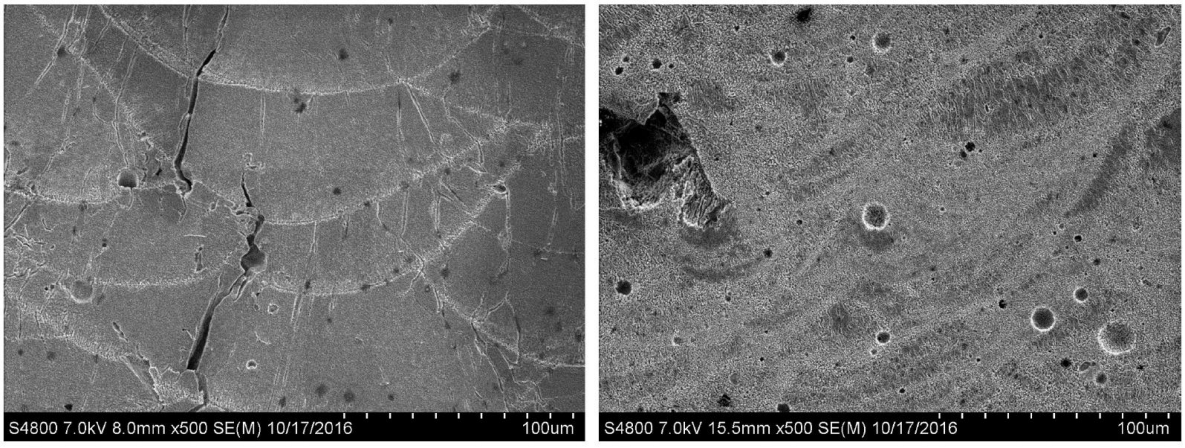

Figure 8 Micrographs of etched Al7075, processed as received. Large networks of cracks are observed in the absence of Zr (left). With the addition of Zr nanoparticles, no cracking is observed, but there is some residual porosity (right). Rows indicate increasing [70].

Zirconium was also added to AlCuMg powder to reduce cracks that are formed during L-PBF [72]. Formation of cracks is prevented and pronounced structural modification is observed due to precipitation of Al_3Zr. These precipitates act as effective heterogeneous nuclei which led to grain refinement. The addition of zirconium also led to an increase in tensile strength and yield strength, but a decrease in elongation.

Due to the flexibility of the *in-situ* alloying technique, the Al-xCu alloys system has been *in-situ* alloyed with L-PBF as an effort for compositional optimization before opting for gas atomization process [73]. The melting point difference in aluminium and copper leads to incomplete diffusion of copper which is subsequently seen as macro-elemental segregation. The inherent short melt pool duration during L-PBF also adds to the problem of incomplete copper diffusion. Compositional and microstructural gradient can be seen around the partially diffused copper particles. In general, the solidified melt pools consist of three distinct zones – the high cooling rate zone, the low cooling rate zone, and the heat-affected zone. Among all compositions tested, Al33Cu (wt%) exhibits the highest compressive strength of about 1000 MPa. The compressive failure of these alloys is controlled by the shear mode buckling of lamellar eutectic structure. Hence, the addition of copper leads to a nano-scale eutectic structure that is beneficial for improving the compressive strength. The Al33Cu contains high Al_2Cu phase content and a larger volume fraction of fine eutectic structure, resulting in high compressive strength. Samples from L-PBF with pre-heated powder bed also contains more Al_2Cu intermetallic, resulting in 50 % UTS improvement and better elongation despite having a coarser microstructure as compared to the one without preheating [74]. In another study by Bartkowiak *et. al*, the *in-situ* alloying of Al-xCu was approached with a powder blend of bigger aluminium particles with smaller copper particles (3 μm) [75]. The powder blending process was done with a tumbling mixer and resulted

in a homogenous blend without powder agglomeration. However, only single tracks had been studied and it was shown that the powder mixture achieved homogenous microstructure with no visible macro-segregation after laser melting. There was also no porosity observed in the melt tracks. A similar approach was also done on Al-xZn within the same research and homogenous cross-section single tracks were also obtained.

Aside from application-specific materials development, interesting utilization of the *in-situ* alloying process on the development of anchorless selective laser melting (ASLM) has also been done. Support structures are typically needed in an L-PBF process to prevent the warpage of overhang structures resulting from residual stress, but it is not required in ASLM. In principle, ASLM can be achieved by preheating the powder bed to a high temperature (about 50 % of the melting point of material) to achieve stress relief [76, 77]. However, solid-state sintering of unprocessed powder can occur at this high temperature and lead to powder recoating issues. To overcome this problem, mixed and blended powders with a higher melting point than the alloyed product can be used. One choice of raw powder to be used is the pre-cursor powder of eutectic/hyper/hypo eutectic alloy. In-fact, *in-situ* alloying of Al12Si had been used to demonstrate ASLM [76]. In the study, the L-PBF processing capability of pre-alloyed and *in-situ* alloy Al12Si has been compared. The Al12Si elemental powder blend can withstand substrate pre-heating of 380 ^{o}C but the pre-alloyed Al12Si agglomerates after preheating at a temperature of only 100 ^{o}C. With the high pre-heating temperature, 10 mm horizontal unsupported overhang structures with only 1 mm upward warpage at the tip (Figure 9) were successfully fabricated. Furthermore, ASLM was also achieved via *in-situ* alloying of pre-alloyed Al1.2Mg (wt%) and Si14.8Cu6.5Ni(wt%) mixed to form Al 339 [77]. *In-situ* alloying with a preheating temperature of 380 ^{o}C successfully produced a horizontal unsupported overhang of 10 mm with only 0.1 mm warpage. Meanwhile,

an attempt to use pre-alloyed Al339 powder with 380 ^{o}C preheating temperature led to powder agglomeration and resulted in recoater collision during L-PBF.

The previous works relevant to *in-situ* alloying of aluminium based alloys with L-PBF are compiled in Supplementary Materials Table S1.

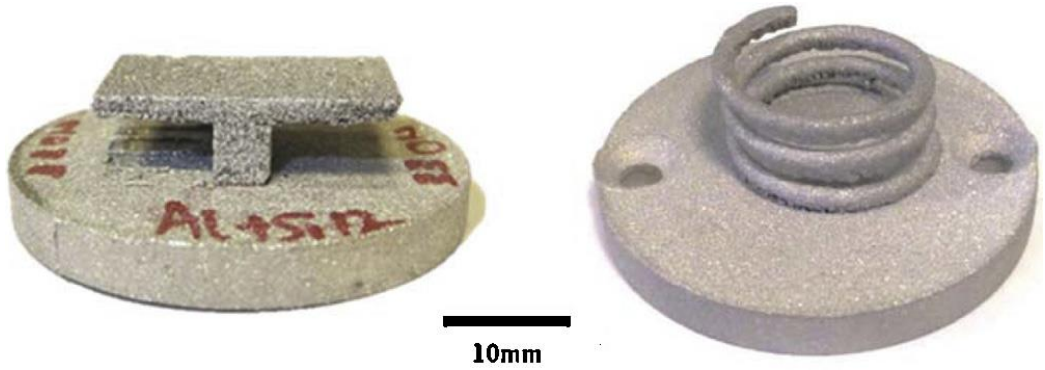

Figure 9 Unsupported overhang components produced using the ASLM process from elemental Al + Si12 powder

3.2 Titanium and its Alloys

3.2.1 Ti6Al4V Based

Using Ti6Al4V in original composition, the effect of precursor powder types (mixed powder for *in-situ* alloying or pre-alloyed powder) on microstructures and properties have been studied for L-PBF [78]. In the study, pre-alloyed Ti6Al4V powder was used as a benchmark. Three different elemental powder mixtures were then prepared for study, namely: (1) simply mixing powders of similar size, (2) mixing large titanium powder with smaller vanadium and aluminium powder, and (3) satellite smaller vanadium and aluminium particles on larger titanium powder. It was found that the usage of (2) and (3) powder mixtures for L-PBF gave better density, homogeneity, and hardness as compared to the usage of (1). However, the powder mixture (3) did not fare as well as the powder mixture (2), mainly because the technique was not optimized in which the elemental vanadium powder used in this study is not small enough to adhere to the titanium powder.

Nevertheless, the key finding is that proper mixing and dispersing of small alloying particles with parental elements can produce parts comparable to that of pre-alloyed powder feedstock.

Using a similar technique as Simonelli *et al.* [78], the same group attempts to suppress the highly columnar prior-β formation of Ti6Al4V through the addition of iron, which promotes columnar to equiaxed transition (CET) [79]. The choice of element addition was based on the growth restriction factor (*Q*) in which high *Q* favours constitutional supercooling that can lead to CET. Iron is a viable choice as it demonstrates relatively high *Q* value, exhibits unfavourable kinetics to form unwanted intermetallic compounds with titanium, and exhibits similar thermo-physical properties as titanium. The iron addition of up to 3 wt% leads to significant grain refinement with little increase in benefits at 4 wt% (Figure 10). The iron rejection during solidification inhibits side growth of columnar grain which reduces the competitive growth mechanism. Consequently, more columnar grains persist, leading to grain refinement and less prominent texture as compared to L-PBF built Ti6Al4V. The addition of 3 wt% iron leads to retention of metastable β grains and forms desirable laminar α + β microstructure (while maintaining fine prior beta) upon suitable heat treatment.

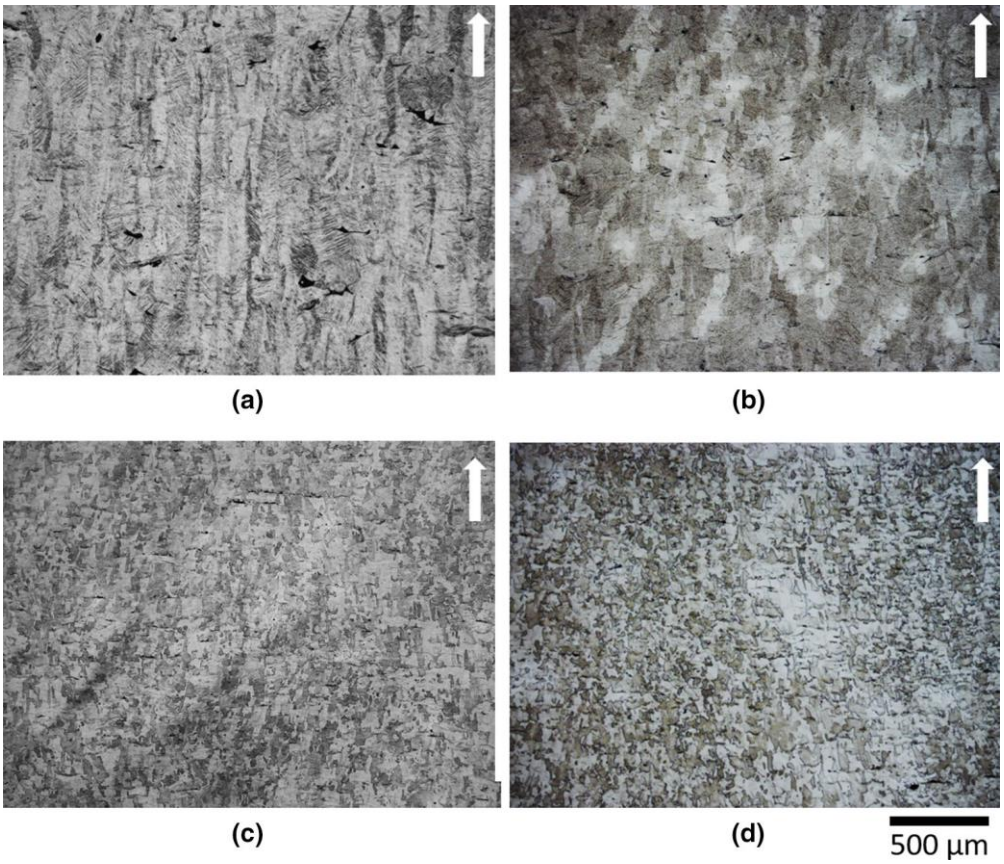

Figure 10 Optical micrographs of as-built samples revealing the microstructure: (a) Ti-6Al-4V, (b) (Ti-6Al-4V)-2Fe, (c) (Ti-6Al-4V)-3Fe, and (d) (Ti-6Al-4V)-4Fe. The build direction is indicated by the white arrows [79].

To extend the existing L-PBF materials library, an attempt to manufacture Ti6Al4V+10Mo (wt%) had been done [80]. Without the addition of molybdenum, epitaxial growth from partial re-melting accompanied by stable planar solidification leads to large columnar β grains in Ti6Al4V. However, no columnar β grain was formed after molybdenum addition as it leads to instability of the planar solidification front and induces cellular solidification. As a result, the growth of β grains is toward the melt pool centre. The as-built Ti6Al4V+10Mo (wt%) was found to be fully β phase. Incompletely diffused molybdenum particles smaller than 10 µm were found to be randomly distributed throughout the matrix but are too minute to be picked up by XRD. The incomplete diffused molybdenum can lead to molybdenum-rich zones in which the β phase is fully stabilized. Depending on the temperature of heat treatment followed by quenching, the microstructure can

consist of either α+β or fully β phase. With the heat treatment process, the homogeneity of Ti6Al4V+10Mo (wt%) can be improved, and it gets better with higher temperatures. Similar work was also done by mixing molybdenum and iron (which are both β titanium stabilizer) into Ti6Al4V to form Ti10V2Fe5.5Al (wt%) [81]. With different heat treatment processes, it was shown that the degree of α and β phases can be tailored to achieve a wide variety of mechanical properties.

Functionalization of implants through the improvement of anti-microbial properties had been done via *in-situ* alloying of Ti6Al4V+1Cu (at%) [82]. The UTS of Ti6Al4V improved from 1243 to 1550 MPa after the minor addition of copper. Copper addition also resulted in decreased *E. coli* growth by an order of magnitude and decreased *S. aureus* growth by two orders of magnitude. A similar study was also done by Maxpherson *et.al* using Ti6Al4V+5Cu (wt%) [83]. It was found that copper addition leads to a microstructural change from α' to extremely fine α+β Widmanstätten structure. Traces of Ti_2Cu were also detected in the matrix that leads to strength improvement. In addition, Ti_2Cu also serves to promote antibacterial properties. *In-situ* alloyed Ti6Al4V+5Cu (wt%) shows moderate anti-bacterial property which is inferior to that of casted counterpart, which can be caused by the high cooling rate of L-PBF that leads to lesser Ti_2Cu. Maxpherson *et.al* also did studies on *in-situ* alloyed Ti6Al4V+0.5Ag (wt%). The resultant alloy shows minimal changes in microstructure but leads to three times increased ductility while retaining the same strength as Ti6Al4V. The silver addition did show anti-bacterial property but is inferior to the *in-situ* alloyed Ti6Al4V+ 5Cu (wt%) parts.

To improve corrosion resistance, nano-sized platinum was added into pre-alloyed Ti6Al4V powder [84]. A novel dual centrifugal mixer was used in this study to avoid the possibility of powder agglomeration (low energy blender) and particle morphology change (when a planetary ball mill is used). The bending of one batch of powder can be done in just several minutes with

nano-sized platinum being “doped” evenly on the surface of Ti6Al4V particles (Figure 11). *In-situ* alloying of Ti6Al4V+Pd powder mixture resulted in homogenous platinum distribution with occasional platinum rich areas in the form of lines (Figure 12). Platinum addition does not affect the mechanical properties significantly but leads to improvement in corrosion properties. It can eliminate the active anodic region by shifting the corrosion potential into the passive region for Ti6Al4V, achieving improved corrosion resistance.

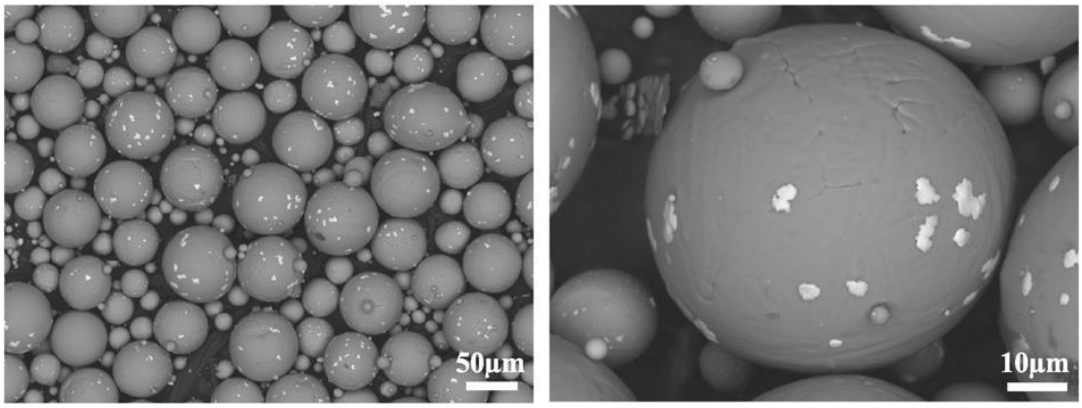

Figure 11 Backscattered electron SEM images showing the Pd powder (bright region) “doped” on Ti6Al4V powder [84]

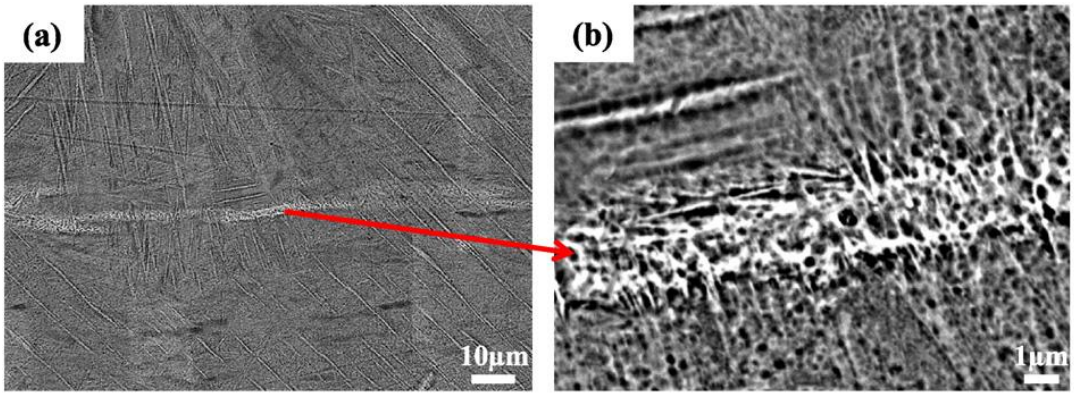

Figure 12 Back scattered electron SEM images showing (a) microstructure and (b) magnified region of as-SLMed Ti6Al4V-0.2Pd where Pd rich region can be seen as bright region [84]

In short, *in-situ* alloying of Ti6Al4V with elements like molybdenum, iron, silver, copper, and platinum have been done to develop new materials that improve biomedical related properties and

to reduce the texture strength. Moreover, the pre-alloyed Ti6Al4V system had been chosen as a benchmark to study the effect of precursor powder on the quality of products made via *in-situ* alloying. A table to summarize notable works relevant to *in-situ* alloying of Ti6Al4V derived alloys with L-PBF can be found in Supplementary Materials Table S2.

3.2.2 Titanium with β stabilizers

In-situ alloying of titanium alloys with β stabilizer via L-PBF is mainly for the making of biomedical implants. Biomedical titanium alloys with β stabilizer are the largest group of alloys to undergo *in-situ* alloying. Biomedical implants play an important role to replace missing, damaged or weakened biological structures [85]. Their impact on life is paramount for their ability to improve people's quality of life and even extend a person's life span. Unfortunately, structural implants like hip joint replacements cannot always outlast a human's life. For instance, a comprehensive review by Ridzwan *et al.* shows that almost 10 % of hip joint replacements done need to undergo revision surgery and this number can increase depending on the patient's condition. More than half of these revision surgeries are due to the loosening of implants and can largely be attributed to the effect of "stress shielding" [86]. The "stress shielding" effect is in accordance with the Wolff's law which states that the bone in a healthy person or animal will adapt to the loads in which it is placed [87]. Most of the current commercial implant materials, e.g. 316L stainless steel, CoCrMo, and Ti6Al4V were intended for other industries like the aerospace and marine industries. They are not specifically designed as implant materials, thereby potentially causing problems to the receiving patients. CoCrMo and 316L stainless steel have high elastic moduli of more than 200 GPa while that of human cortical bone range from 17.6 to 28 GPa [88], potentially leading to a detrimental problem of osteolysis. Despite having a lower elastic modulus for Ti6Al4V, around 130 GPa [89], it is still many times higher than that of human cortical bone.

This will lessen the load being borne by the bone, leading to bone resorption and ultimately implant loosening. Moreover, implant loosening can also be attributed to other causes like wear, high joint space fluid pressure, bacterial infection, and genetics [90]. In addition to implant loosening, the alloying elements in these commonly used implant materials have been associated with cytotoxicity, for example, nickel in 316L stainless steel, cobalt, and chromium in CoCrMo, as well as aluminium and vanadium in Ti6Al4V. The potential harm brought about by these elements is not further discussed here since a comprehensive review on the toxicity of these elements has been done by Wapner [91].

To improve the quality and longevity of implants, one of the directions is the development of new materials. Therefore, new β-titanium alloys composed of non-toxic elements such as niobium, tantalum, zirconia, molybdenum, and tin (Figure 13) were since designed to achieve lower elastic modulus, greater strength and better corrosion resistance [92]. β-titanium stabilizers like niobium and tantalum have high biocompatibility and are the primary choices of elements for consideration when it comes to biocompatible β-titanium alloys. Elements like zirconia, molybdenum, and tin can be added to modify phases and microstructures of resultant alloys if needed.

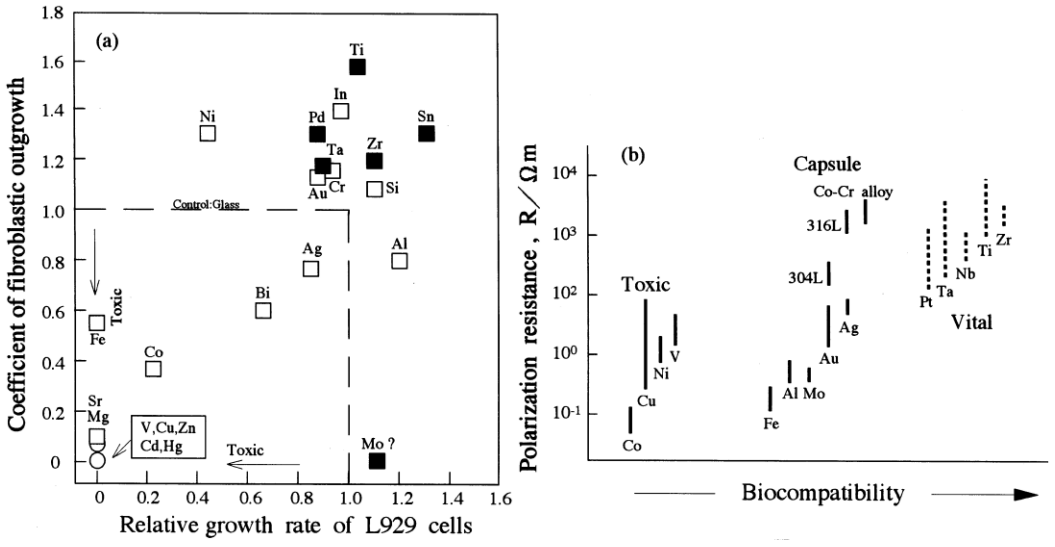

Figure 13 Biocompatibility of metals (a): cytotoxicity of pure metals, and (b): relationship between polarization resistance and biocompatibility of pure metals, CoCr alloy, and stainless steels [92].

An alternative way of implant's bone modulus matching can be realized via proper manufacturing route to introduce porosity [93], lattice structure [39, 94, 95], or achieve topological optimization [96]. With the free-form fabrication capability of AM, systematically induced lattice structures (like homogenous porous material) and near-net-shape topologically optimized implants can be realized. When paired with suitable alloy systems (such as low modulus β-titanium), AM can potentially produce functionally graded implants to meet stiffness and strength criteria while achieving excellent osseointegration property at the same time. L-PBF is one of the AM techniques that is suitable.

Low modulus β-titanium is often metastable and requires a high cooling rate during the manufacturing process to retain the β phase [97]. It is often difficult to achieve a uniform cooling rate in a bulk part manufactured with conventional manufacturing techniques like casting and forging. L-PBF is inherently designed for this due to its quench-like rapid laser melting and cooling cycle, aside from being able to manufacture a near-net-shape β-titanium part straight from a CAD design. L-PBF's unique thermal characteristics and history offer the opportunity to tailor the microstructure of an alloy, potentially achieving different material properties as compared to those produce via conventional methods [98].

In-situ alloying using L-PBF has been popular to achieve β-titanium using powder mixtures. This is due to the following reasons: (1) as opposed to using pre-alloyed powder, *in-situ* alloying of powder mixture allows for flexible and rapid adjustment of alloy compositions. Different alloy compositions can be designed and manufactured within a short time frame for a quick study on the link between compositional variation and material properties. Optimal compositions for many

alloys have not yet been found for L-PBF which allows more research opportunities using *in-situ* alloying, (2) pre-alloyed β-titanium powder containing refractory β stabilizers such as niobium, tantalum, and molybdenum is not easily available due to the huge differences in melting point and density between the stabilizers and titanium. The differences in material properties lead to challenges during the typical gas atomization process that manufacturing the pre-alloyed powder feedstock. Moreover, small batch production of pre-alloyed powder can be expensive. *In-situ* alloying has the potential to enable compositionally graded components. However, it is good to take note that achieving components with compositional gradient remains a challenge for L-PBF which will be discussed further for multi-metal processing in later sections.

Past studies showed that promising properties can be obtained for β-titanium alloys produced via *in-situ* alloying. *In-situ* alloying of β-titanium typically focused on the reduction of elastic modulus to reduce the stress shielding effect. The reduction of elastic modulus had been done with several approaches which include (1) optimization of β-stabilizer addition into titanium, (2) addition of other element(s) into binary titanium alloys with existing β-stabilizer and (3) porosity induction in β-titanium alloys. Despite the lack of pre-alloyed powder, the study on alloys of different compositions as a mission to search for optimal biomedical materials is possible due to the flexibility of *in-situ* alloying. The approaches for elastic modulus reduction were done via *in-situ* alloying with L-PBF and the key findings of each research are as follow:

(1) Optimization of β-stabilizer addition into titanium

Low Young's modulus with enough strength can be, in principle, obtained when full β-phase is retained with minimal alloying components [38]. Past studies had shown that this minimal point can be obtained at 25.5 at% or 40 wt% niobium addition for binary TiNb alloys upon quenching.

Below the stated minimum niobium addition, undesired α'' and ω phases will be formed, decreasing yield strength and increasing the Young's modulus. Above the stated minimum niobium addition, full β-phase can be retained, and the Young's modulus will increase slowly with additional niobium. As such, most of the past studies on L-PBF uses minimal niobium addition of 40 wt% to retain single β-phase. Experimentally, the minimum Young's modulus was found to be at the composition of Ti42Nb (wt%) [99]. Parameters optimization issues aside, most research done on L-PBF of TiNb are on completely metastable β instead of near β compositions. In a typical binary low modulus titanium alloy with non-intermetallic forming β stabilizing element, it is known that two instances of Young's modulus minima can be typically seen with varying amount of β stabilizer (Figure 14). The second minimum of near 42 wt% niobium is of greater interest in the community for its lower modulus as compared to that of the first minimum. Depending on the thermal history, titanium alloy can exhibit phases like α, α', α'', metastable β, stable β, and ω through the addition of beta stabilizer [100-102]. The α and α' phases can be associated with as-quenched alloys with the minor addition of niobium while α'', β, and ω phases can be associated with that when niobium addition is near that of fully β stabilized composition [97]. The α' and α'' martensites, as well as the metastable ω phase, are formed when the alloy is rapidly quenched in which their formations are highly dependent on the amount of β-stabilizer added [103].

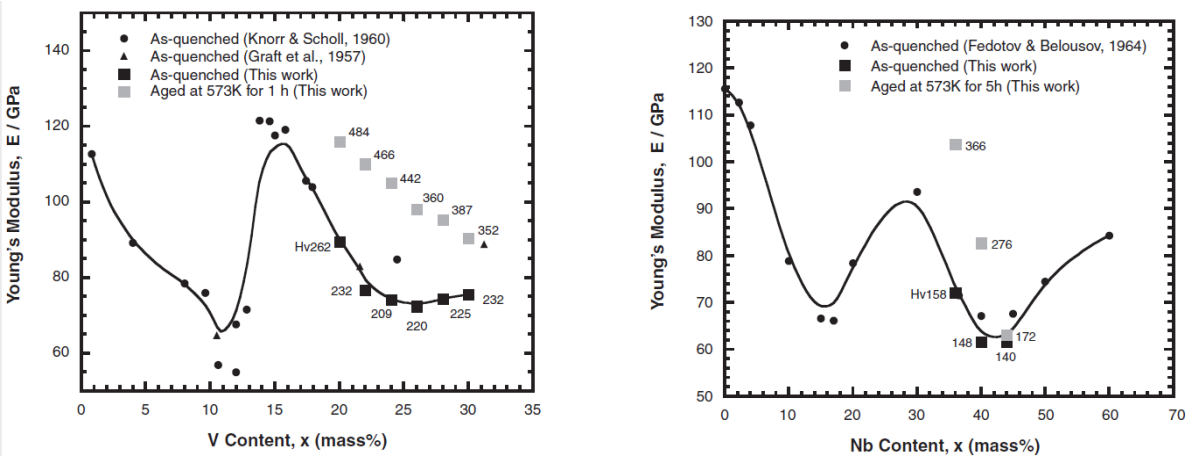

Figure 14 Young's modulus variation of as-quenched titanium-based alloy with the addition of beta stabilizer [99]

In-situ alloyed Ti-xNb using L-PBF where x = 0, 15, 25, 45 at% were studied by Wang *et.al* [104]. It was found that Ti25Nb has the lowest Young's modulus among other compositions tested due to its correspondence to full β retention with minimal niobium addition. This composition also demonstrated the best *in-vitro* appetite forming capability, possibly due to it having the highest volume fraction of β-titanium phase, which is associated with appetite nucleation. The addition of more niobium leads to more un-melted niobium volume and decreases the volume fraction of the β-titanium phase. Nevertheless, the *in-situ* alloyed Ti40.5Nb (wt%) does achieve a comparatively low average Young's modulus of 77 GPa despite the existence of unmelted Nb particles [105]. Meanwhile, a study by Huang *et. al* utilizes *in-situ* alloying to study Ti-xTa alloy of different compositions (x = 0, 10, 30, 50 wt%) [106]. The study found that Ti30Ta possesses the lowest modulus (71 GPa) and the highest yield strength (920 MPa) among all compositions. The composition is a near β composition where the phase constituent is α'' dominated, indicating that it is not necessary to retain the full β phase for elastic modulus minimization. By keeping the volumetric ε at a constant, it was found that the type of porosity changes from keyhole induced porosity to lack of fusion porosity. The additional tantalum particles at higher compositions require additional energy to melt, hence leading to insufficient energy for melting and fusing between

layers when the volumetric ε were kept constant. Tantalum addition also leads to more unmelted tantalum particles which can act as inoculants, causing the prior β-grains to undergo a columnar to equiaxed transition. A similar study by Zhao *et. al.* investigated a narrower range of *in-situ* alloyed Ti-xTa compositions (x = 6, 12, 18, 25 wt%) [107]. The composition for elastic modulus minimization was found to be at Ti25Ta, a composition similar to the study by Huang *et. al.* [106]. The Ti25Ta alloy is α' phase dominated, which is the same as that reported by Brodie *et. al.* [108]. Despite being far from β-stabilized compositions, *in-situ* alloyed Ti25Ta shows a low elastic modulus of 89 GPa with a high yield strength of 1029 MPa. It was also found that Ti25Ta has the best corrosion resistance in ringer's solution among all other compositions tested due to the formation of stable Ta_2O_3 passive film. The Cl^- anion in ringer's solution can intensify the anodic dissolution of TiO_2 passivating film. The addition of tantalum causes a rise in Ta_2O_5 passive layer, leading to better promising candidate for biomedical implants application. Despite having the unmelted tantalum, in the study done by Sing *et al.*, tantalum dissolution has been proven to be sufficient for the retention of low modulus β-phase. The *in-situ* alloyed Ti50Ta successfully achieved a low elastic modulus of 75.77 GPa with a high yield strength of 882.77 MPa [109].

With laser re-melting, the texture strength of Ti42Nb is reduced where prior β-grains close to that of equiaxed grains can be observed. Re-melting-induced texture weakening leads to an improvement of yield strength from 426 to 545 MPa while maintaining an elastic modulus of 65 GPa. The strength improvement comes with a reduction of elongation property from 25 % to 11 %. These mechanical properties were achieved despite the alloy consisting of mostly α' phase [110]. Another notable finding in this study is on the better choice of ε in the range of 362 J/mm^3 for the *in-situ* alloyed titanium-tantalum system, a much higher value as compared to a previous study by Sing *et. al* (144 J/mm^3) [109]. Laser re-melting strategy certainly shows promising

potential to advance the *in-situ* alloying using L-PBF. The main drawback of the strategy is the significantly increased build time, primarily due to the additional time needed for laser scanning.

The study on near β titanium-niobium system is limited and only two studies were done via *in-situ* alloying with L-PBF. One research team had printed parts with the composition of Ti35Nb (wt%) as an effort to study the effect of inhomogeneity on mechanical and corrosion properties [111]. The as-fabricated and solution-treated (1000 ^{o}C at 24 hrs followed by air cooling) samples were compared in the study. XRD analysis shows that the as-printed part is of majority β phase with unmelted niobium particles, achieving a Young's modulus of 84.7 GPa. It is speculated that the concentrated laser energy source is the cause of incomplete melting/diffusion of niobium particles. Meanwhile, the solution-treated sample shows similar XRD analysis result but without the XRD peaks from niobium, indicating that better homogeneity was achieved. Large unmelted niobium particles act as arrest zones for shear bands and eventually act as stress concentrators for grain bound sliding, leading to poor ductility of as-printed parts as compared to heat-treated parts (38.5 to 47.3 %). A slight decrease in yield strength was detected after the heat treatment. The heat-treated part also shows better corrosion resistance due to its better chemical homogeneity. Unfortunately, no information on the change in elastic modulus was shown after heat treatment. In another study, near β Ti20Nb (at%) was manufactured and traces of α'' martensite were seen in XRD [112]. It was found that the martensite traces decrease with increased ε, which is caused by better dissolution of niobium into the matrix. No further studies were done on the alloy system in that research, possibly due to the presence of unmelted niobium. There is a general lack of study on as-fabricated near β binary titanium alloy systems and their mechanical behaviour are not well understood.

Although not explicitly stated as an alloy designed for low modulus biocompatible implant, the work on the *in-situ* alloyed titanium-rhenium system has laid the groundworks for the future L-PBF research on the system. Rhenium has almost twice the melting point of titanium (3185 ^{o}C and 1668 ^{o}C), which leads to incompletely melting of rhenium particles that can be reduced with increasing ε [113]. The addition of 5.66 wt% rhenium in titanium greatly increases the yield strength (461 to 1038 MPa) while also reduces the elastic modulus (119 to 103 GPa). However, the ductility of the alloy is largely sacrificed down to a value of only 2 %. The phase constituent after rhenium addition is mainly of α' phase as the rhenium addition in the study is insufficient to retain the β phase. Further studies on titanium-rhenium alloys were made on 2 and 4 wt% rhenium addition into titanium [114]. It was found that rhenium addition can lead to the refinement of lath phase α/α' microstructure which can be one of the factors behind the strength improvement. The nature of rhenium as β-Ti stabilizer leads to β phase retention around the incompletely diffused rhenium particles with the formation of the brittle ω phase. The ω phase, coupled with refined microstructure and enhanced oxygen level from rhenium addition eventually leads to brittle fracture characteristic. The brittle characteristic deteriorates fatigue crack growth resistance of TiRe when compared to titanium. For the alloy system to be useful in structural application, further studies are required to ensure its safe use with predictable failure from fatigue loading.

In some cases, *in-situ* alloying technique serves as a quick tool to screen through the effect of element(s) addition on a part's biocompatibility. Using *in-situ* alloying, Wang *et. al.* found that the addition of niobium into titanium leads to better *in-vitro* apatite forming capability as compared to its pure titanium counterpart [104]. A similar study shows that seeding of MC3T3-E1 osteoblast precursor cell line on *in-situ* alloyed Ti25Nb (wt%) leads to better cell spread and proliferation when benchmarked with titanium parts, in addition to a superior in-vitro appetite forming

capability [115]. Furthermore, *in-situ* alloyed Ti25Nb (wt%) scaffold demonstrated impressive immunomodulatory properties [116]. The scaffold was also implanted into rabbit's tibia and shown to better promote bone regeneration and osseointegration as compared to the pure titanium counterpart. As for Ti50Ta (wt%), Huang *et. al.* found that using the same lattice structures, Ti50Ta possesses similar biological responses to titanium and Ti6Al4V based on the cell proliferation tendency of osteosarcoma cell line SAOS-2 [106]. Meanwhile, Yan *et. al.* demonstrated that Ti15Ta10.5Zr does not induce infection and osteomyelitis in the surrounding of rat's tibia after five weeks of implantation in rat tibia's fracture [117]. All of these observations point toward the promising potential of *in-situ* alloyed titanium-based alloys as a biocompatible material for implant applications.

Pre-alloyed titanium with β-stabilizer is still not widely available and has very limited attempts to study on them. Despite that, a study on Ti45Nb (wt%) where pre-alloyed powder feedstock was used has been made [118]. XRD patterns on the L-PBF part show β-titanium peaks with broadening characteristics possibly due to residual stress in the part. The part showed a compressive strength of 723 MPa. Unfortunately, no Young's modulus was reported in the study. Another study was done on Ti42Nb (wt%) processed by L-PBF using pre-alloyed powder [119]. Parts built were more homogenous (contains no un-melted niobium) than those manufactured via *in-situ* alloying and they have a relative density of more than 99.5 %. Figure 15 shows the polished surface of Ti42Nb and occasional microstructural inhomogeneity can be seen in Figure 15(c). This feat can be achieved with a relatively low E_d of 40 J/mm^3 as compared to those done via *in-situ* alloying (214 J/mm^3 when optimized [105]). Full-β matrix was obtained and the alloy also shows better compressive yield strength as compared to tensile yield strength (674.08 MPa to 831.58 MPa).

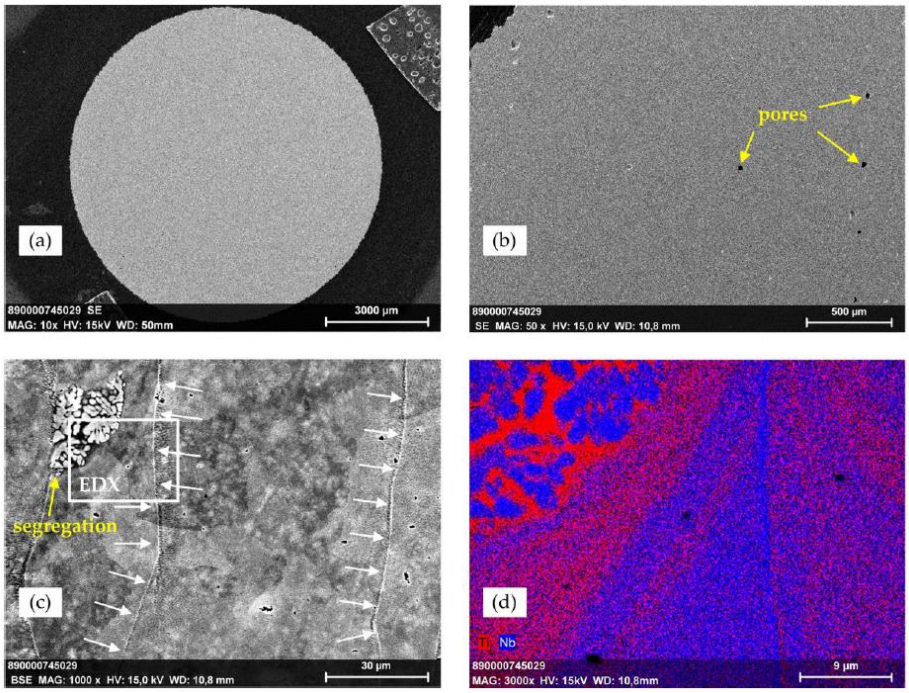

Figure 15 SEM-EDS image of polished Ti-42Nb tensile test specimen a) 10x SE mode b) 50x SE mode c) 1000x BSE mode and d)EDS mapping of region shown in (c)

(2) Addition of other element(s) into binary titanium alloy with existing β-stabilizer

The addition of tin to near β titanium-niobium composition (forming Ti37Nb6Sn (wt%)) has been experimented with to achieve parts with low elastic modulus [120]. The tin addition suppresses hard and brittle ω precipitation in TiNb of near β composition, in which the precipitation can lead to an increase in Young's modulus. The study also found that increased tin leads to more preferential [100] grain growth towards the build direction. The optimal ε value was found to be at 125 J/mm^3 where the lowest Young's modulus (66GPa) and high yield strength (~775MPa) were obtained. It is interesting to take note that, unmelted niobium particles with an average size of more than 30 µm were found to initiate secondary crack at the boundary, hence compromising the ductility. It was further suggested that the low modulus of this alloy can be attributed to the uniform α''-colony within the β-matrix. Another study utilizes *in-situ* allying to develop new material for biomedical application by the addition of zirconium into titanium-

tantalum alloy [117]. Ti5Ta-xZr (x = 1.5, 5.5, 10.5, 15.5 wt%) were studied and it was found that zirconium can stabilize the β phase in these alloys. The phase constituent of Ti15Ta10.5Zr is almost pure β, exhibiting an impressively low elastic modulus value of 42.93 GPa. A high yield strength of 768.61 MPa is also obtained, demonstrating the vast potential of TiTaZr alloys system as a candidate for biomedical implant material. Despite the outstanding properties, there are limited studies on the *in-situ* alloying process involving zirconium. The speculated reason is due to the tendency of zirconium powder to undergo autoignition in the atmosphere, hence needing proper facilities and intensive care to handle.

(3) Induced porosity in β-titanium alloy

Macro-porous Ti40Nb (40 wt%) bulk L-PBF samples were produced via *in-situ* alloying of mechanically alloyed (MA) powder [93]. A relatively slow scan speed of 35 µm/s was used in the study. Traces of α and α'' phases are found to be embedded in a β matrix based on transmission electron microscopy (TEM) observation. No macro-segregation of niobium particles were reported due to the powder preparation technique. Owing to the porous structure (~17%), elastic modulus as low as 33 GPa was achieved. Nevertheless, there is no information reported on tensile mechanical strength. Sing *et al.* also used in-situ alloying to fabricate titanium-tantalum porous structures and concluded that the L-PBF parameters can affect the physical and mechanical properties of these structures [39]. In another study of *in-situ* alloyed porous titanium-molybdenum, it was discussed that the porosity level of the manufactured part has a significant influence on corrosive properties [121]. The part's corrosion resistance was found to be higher in parts with lower porosity. Nevertheless, the parts with lower porosity values were also found to be more homogenous with lesser un-melted molybdenum particles. It is hence difficult to conclude

that porosity value alone had caused the change in corrosion resistance, as compositional segregation can also play a part in such corrosion resistance properties.

To summarize, most low modulus biocompatible titanium alloys manufactured by L-PBF were done using *in-situ* alloying. However, all β-titanium stabilizers used are refractory and porosity-segregation dilemma remains as a challenge to be solved. More research in this area is needed in order to address the porosity-segregation dilemma and better understand the suitability of *in-situ* alloyed biocompatible titanium alloys as implant candidates. A table to summarize notable previous works relevant to L-PBF titanium alloys with biocompatible β-stabilizer (mostly *in-situ* alloyed) can be seen in Supplementary Materials Table S3.

3.2.3 Other Titanium Systems

Aside from the widely used Ti6Al4V alloy and trending biomedical titanium alloys with β-stabilizer, other titanium alloys were also explored for *in-situ* alloying using L-PBF. The Ti-185 alloy is a high strength and economical titanium alloy but the formation of β-flecks (macro-segregation of iron) via ingot casting restricted its commercial use. As such, an attempt to produce Ti-185 with L-PBF has been made due to its rapid cooling rate that can potentially suppress the macro-segregation of elements [122]. As the composition is relatively new for L-PBF, a ball-milled powder mixture was used in the study. It was found that the L-PBF Ti-185 resulted in good mechanical properties (1890 MPa compressive strength and 11 % elongation) due to the absence of β-flecks, fine-grained structure, high dislocation density, distribution of nano-sized α-phase within β-matrix and high oxygen content. Heat treatment on the samples was also conducted and it leads to homogenous spreading of α-phase that further improves the mechanical properties (2380 MPa compressive strength and 26 % elongation).

Although scarce, research on *in-situ* alloying of nickel-titanium, has also been explored as a cost-effective alternative to pre-alloyed nickel-titanium powder. Work has been done by Wang *et. al* to study the feasibility of making nickel-titanium parts via *in-situ* alloying with different AM techniques [123]. The rapid solidification of melt pools inherent to L-PBF promotes the formation of TiNi, which is responsible for the shape memory effect in nickel-titanium shape memory alloys. However, this also led to the formation of unwanted brittle phases as well as metastable phases. On the other hand, a study by Zhang *et al.* shows that *in-situ* alloying of nickel-titanium is feasible when the scanning speed is slow enough for densification (more than 99.5 % relative density) and homogenization to form TiNi phase [124]. With increasing scanning speed, an unwanted Ti_2Ni phase can form. No further study on recovery strain has been made, prompting the need for more research on the topic.

Furthermore, compositionally modified nickel-titanium alloy was done through the addition of niobium, mainly as an attempt to improve the alloy's toughness and biocompatibility [125]. Alloy with the composition of Ni44.0Ti12.2Nb (at%) was achieved via the mixture of prealloyed Ni-Ti powder and Nb powder. Samples were then built via L-PBF and annealed at a temperature of 850 ^{o}C for 0.5 h. The retained Nb particles causes Nb diffusion that accelerates the formation of eutectic phase and β-Nb phase. The ultra-fine eutectic phase and nanoscaled β-Nb phase formation eventually leads to excellent compression properties of 1640 MPa (YS) and 39 % (compressive strain), a significantly improvement as compared to the as-cast counterpart (YS of 960 MPa). A recovered strain of 8.2 % was recorded from compressive unloading, up from a compressive strain of 21 %. The elastic strain recovery is of 5.6 % and the hyperelastic strain recovery is of 2.6 %. Preliminary studies by Grigoriev *et. al.* [126] and Polozov *et. al.* [127] manufactured Ti2AlNb-based (O phase) intermetallic part via *in-situ* alloying with L-PBF. To achieve optimization of

such an intermetallic part, *in-situ* alloying was first done with Ti5Al (wt%), followed by Ti6Al7Nb (wt%) and finally Ti22Al25Nb (at%). Two types of laser were utilized for these studies: the Gaussian profile laser (400 W, 80 μm spot diameter) and the top-hat profile laser (1000 W, 700 μm spot diameter). Grigoriev *et. al* found that at constant volumetric ε, high powered top-hat laser (950 W) can achieve *in-situ* alloyed Ti5Al with better homogeneity but it is also more prone to cracking. However, Polozov *et. al.* found that the usage of Gaussian profile laser at 275W with constant ε can achieve alloy composition nearer to the designed composition due to milder aluminium evaporation. They then studied the *in-situ* alloying of Ti6Al7Nb and found the presence of partially molten niobium which can be reduced with heat treatment at 1350 ^{o}C (or more than 1200 ^{o}C [128]). The resultant Ti6Al7Nb exhibited an ultimate tensile strength of 850 MPa which is similar to that made by metal injection moulding with sintering. Unfortunately, the L-PBF Ti6Al7Nb exhibits poor elongation properties of only 2 % which might be caused by the large pores formed. A large amount of partially melted niobium is found in in-situ alloyed Ti22Al25Nb by Grigoriev *et.al*. Further heat treatments were done to manipulate the volume fraction of O phase where the hardness value increases with O phase fraction from 338.6 HV (as built) to 353.3 HV (1250 ^{o}C homogenized) towards 358. 3HV (1250 ^{o}C homogenized, 950 ^{o}C aged). Further study by Polozov *et. al.* shows that the heat treatment time can influence the extent of niobium dissolution and O phase volume fraction (Figure 16). Nevertheless, the Ti22Al25Nb built here is not usable for engineering applications due to the significant number of cracks present in the bulk samples.

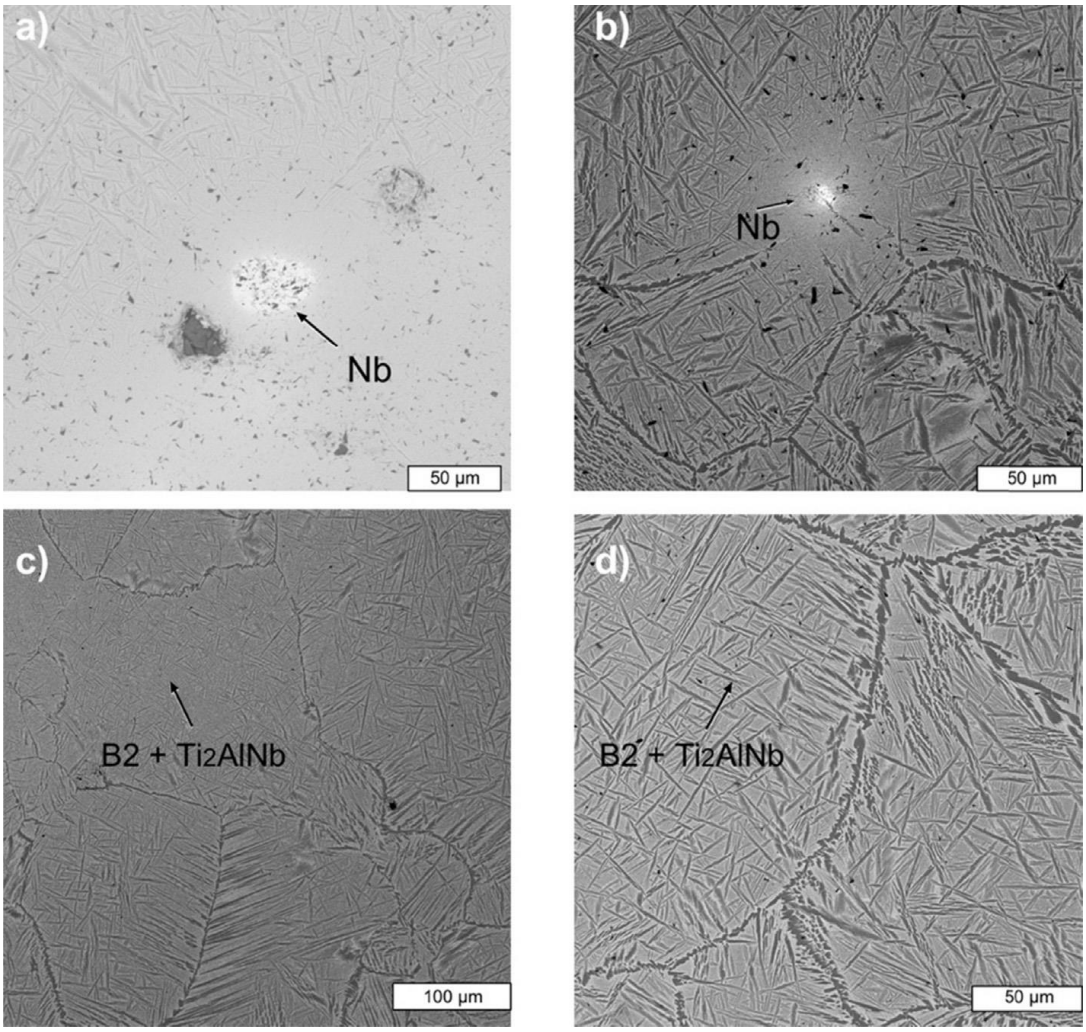

Figure 16 The microstructure of the Ti-22Al-25Nb specimens after undergoing different heat treatment conditions: (a) 1250 °C, 2.5 h; (b) 1250 °C, 4 h; (c) 1350 °C, 2.5 h; (d) 1350 °C, 3.5 h [127].

To reduce the anisotropy of L-PBF parts, Barriobero-Vila *et. al.* approached the problem through the addition of a rare earth element, lanthanum [129]. *In-situ* alloying of Ti2La (wt%) exhibits less pronounced texture with a combination of equiaxed α grains and elongated tortuous α grains. Instead of the typical columnar β to α transformation, the reduced texture strength of Ti2La due to the formation of α nucleation at the solidification front. Further heat treatment of T2La leads to new α phase formation and extensive globularization, along with microstructural refinement that can be controlled by adjusting the cooling rate as seen in Figure 17. The main microstructure forming mechanism of Ti2La begins with the poor solubility of lanthanum in

titanium α/β, which leads to lanthanum rejection to L_1/β interface that causes constitutional supercooling where α nucleation happens via a peritectic path. A similar effect of lanthanum addition on the microstructure was demonstrated with *in-situ* alloying of Ti1.4Fe1La (wt%). This shows the potential in avoiding epitaxial growth during L-PBF.

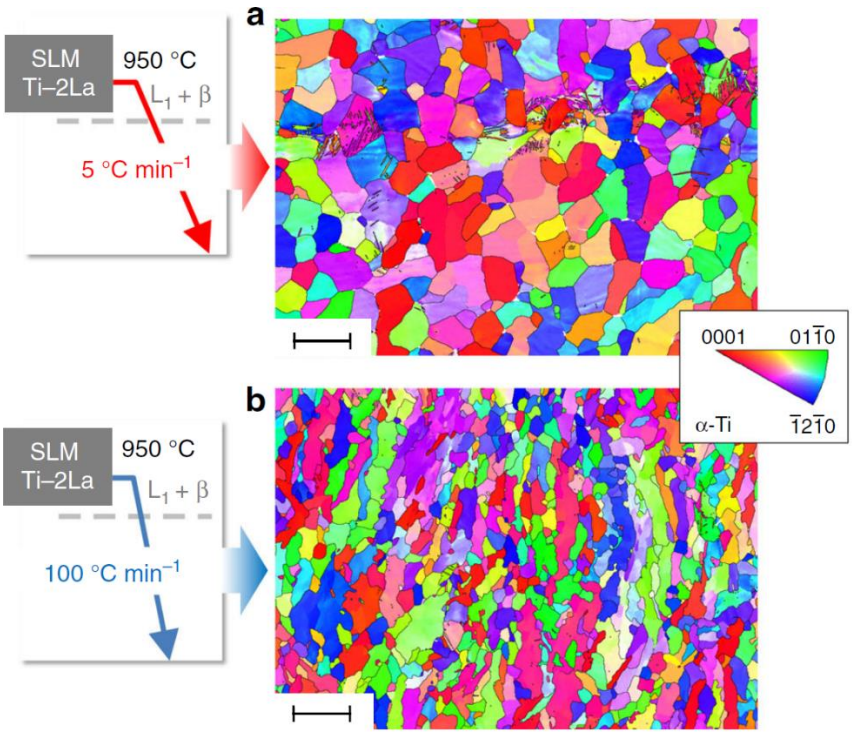

Figure 17 Electron backscatter diffraction (EBSD) mapping showing the effect of heat treatment on SLM as-built parts from 950 °C (L_1 +β field) down to room temperature, forming finer α grains with increasing cooling rate: (a) cooling with a 5 °C min^{-1}, (b) cooling with a 100 °C min^{-1}. The scale bars indicate a length of 50 µm. Black lines in EBSD mapping indicate high angle grain boundaries (>10°) [129].

The compilation of other Ti alloys not classified as Ti6Al4V based or titanium with β stabilizer manufactured via *in-situ* alloying can be seen in Supplementary Materials Table S4.

3.3 Other Material Systems

While aluminium and titanium-based alloys make up most of the research done for *in-situ* alloying for L-PBF, there are some works done on noteworthy materials using this technique as well. The research trend mirrors those using pre-alloyed powders, which aims to expand the materials library for L-PBF.

FeNiSi soft magnetic alloy was manufactured using *in-situ* alloying by L-PBF. Coated powder (Figure 18) is used instead of powder mixture to combine the advantages of chemical homogeneity and lower cost [130]. With low scanning speed, racks appeared in the fabricated samples which led to poor ductility. On the other hand, large irregular pores appeared with higher scanning speed. It is also found that the soft magnetic properties of the samples became worse with increasing laser scanning speed due to macro-structural (porosity) and crystallography (grain size) effect.

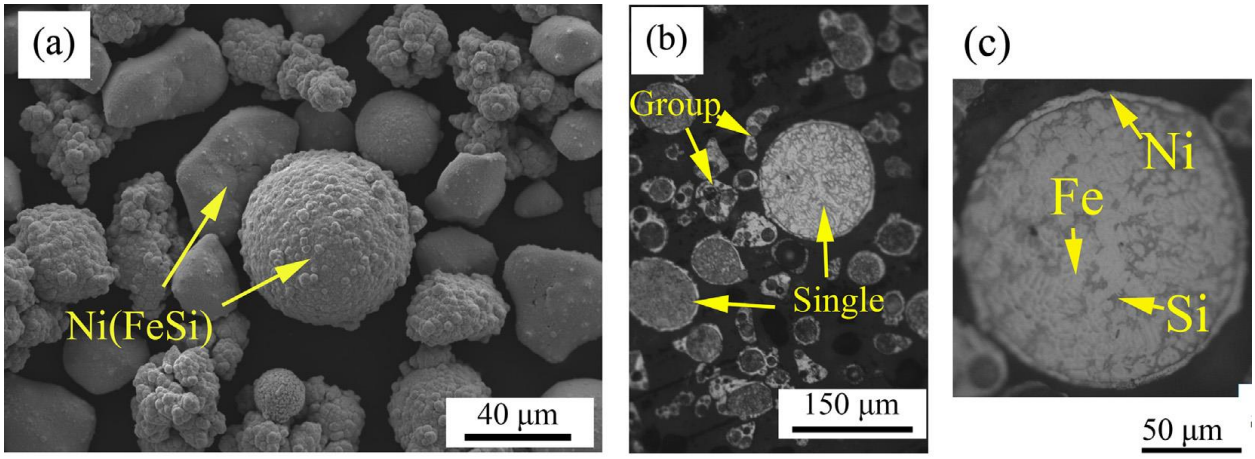

Figure 18 Surface morphologies, (b) and (c), cross-sections of nickel-coated high silicon steel powder.

In-situ alloying by L-PBF is used to study the effect of different contents of aluminium in Mg3Zn (ZK30) alloy [131]. While aluminium has low solubility in magnesium, it is shown that L-PBF can improve the solid solubility due to the rapid solidification and cooling rate. During solidification, the solute produces constitutional supercooling at the liquid/solid interface due to the slow diffusion which results in grain refinement. In a similar study done using dysprosium instead of aluminium, it was also found that grain size decreases significantly with increased dysprosium contents [132]. Grain refinement is influenced by grain nucleation and grain growth. Due to dysprosium additions, the MgZnDy phase has a higher melting point compared to $MgZn_2$, which is also formed during L-PBF. This leads to lower temperature differences between the

secondary MgZnDy phase which precipitated first and the α-magnesium matrix. In another study done using the MgAl alloys system, it is found that equiaxed grain is transformed from dendrites under a high temperature gradient [133]. High scanning speed leads to a high liquid cooling rate that results in refinement of the solid phase. Titanium has also been added to magnesium alloy AZ61 to improve corrosion resistance by promoting the formation of aluminium enriched α eutectic phase and suppressing the formation of Mg_7Al_{12} phase [134].

Even with near full density, L-PBF produced zinc has relatively poor strength and needs to be improved. With minor addition of alloying elements, the mechanical properties of Zn can potentially be improved. *In-situ* alloying of Zn with Mg was done by Yang *et. al.* [135]. As compared to pure zinc, the Zn3Mg (wt%) has significantly enhanced mechanical properties due to grain refinement and precipitation strengthening. The elastic modulus of the alloys also gradually increases with magnesium addition, whereby a value of 48.2 ± 4.2 GPa can be obtained for Zn3Mg. Zinc alloys with 1 to 4 wt% addition of magnesium also have a suitable degradation rate and good cytocompatibility. The degradation rates of these alloys are between 0.10 ± 0.04 mm $year^{-1}$ and 0.18 ± 0.03 mm $year^{-1}$, whereby the recommended value is 0.5 mm $year^{-1}$ or lesser [136]. Better corrosion resistance can also be obtained with magnesium addition via grain refinement and the release of Mg^{2+} that would result in the formation of inert Mg hydroxyl carbonate. The improvement of mechanical properties via magnesium addition was clearly observed. The mechanical properties of Zn3Mg are better as compared to pure zinc, even when the pure zinc has near 100 % relative density (Zn3Mg only has 98.2 % relative density).

Another choice of alloying element for mechanical properties enhancement is silver [137]. Like the addition of magnesium, zinc can be strengthened with silver due to the formation of precipitate and grain refinement via the effect of constitutional supercooling. Depending upon the amount of

silver, the corrosion rate of the Zn-xAg alloy can be decreased or increased. Minor silver addition leads to grain refinement which increases corrosion resistance. However, too much silver can lead to excessive $AgZn_3$ precipitation and leads to galvanic corrosion.

A summary of *in-situ* alloying of other material systems is tabulated in Supplementary Materials Table S5.

4 Multi-metal Processing Using Laser Powder Bed Fusion

In L-PBF, the powder is deposited layer by layer onto a powder bed and a laser beam is utilized to selectively melt regions within each layer to form 3D parts. Conventional L-PBF does not have a similar level of flexibility as directed energy deposition (DED) for multi-metal processing due to the lack of proper deposition mechanisms. Hence, there has not been much research on multi-metal printing using L-PBF. A brief overview of other multi-metal processing methods is given in Supplementary Materials Section 2.

To date, fabrication of different multi-metal parts using L-PBF have been explored such as Inconel 625/steel [138], tantalum-tungsten/steel [138], tool steel/copper-chromium-zirconium [139], tool steel H13/copper [140], aluminium alloy/copper alloy [14], 316L stainless steel/copper alloy [141], TiB_2/Ti6Al4V [142], 316L stainless steel/MS1 maraging steel [143], Fe/Al12Si [144]. Besides L-PBF, electron beam powder bed fusion (EB-PBF) has also been used for fabricating Inconel 718/316L stainless steel [145] and Ti6Al4V/copper [146] multi-metal parts. The presence of welding features of these parts is substantially smaller than those fabricated by conventional welding methods. For ease of discussion, the sections are divided into the material used as structural material i.e. material with the higher strength, with the other materials in the multi-metal systems considered as functional material, i.e. material used to enhance the functionality of the parts and is added onto the structural material.

4.1 Steels

In a study conducted using 316L stainless steel/C18400 copper alloy, a substantial amount of iron and copper diffusion was observed at the interface, which suggests good metallurgical bonding [14]. The diffusion of elements was assisted by the convective forces within the melt pools. Due to the rapid cooling in L-PBF, the melt pools underwent supercooling, which means that the heat removal rate exceeded the heat of fusion releasing rate. However, no further study was done on L-PBF process parameters.

Similar results were obtained in studies using 316L stainless steel/Cu10Sn [147, 148]. Respective optimised parameters for 316L stainless steel and Cu10Sn were used and microscopic cracks were found near the boundary of the interface and 316L stainless steel but not at the boundary between the interface and Cu10Sn. This is attributed to the difference in physical properties between steel and bronze, such as the coefficient of thermal expansion which caused the tearing of the steel. Furthermore, dendritic crack that is substantially perpendicular to the boundary of the interface and 316L stainless steel also observed due to the higher thermal conductivity of Cu10Sn which concentrated a large amount of heat in the interface which led to gradual increase in thermal stress, causing the cracks to propagate [148]. FE-SEM images of the interface are shown in Figure 19.

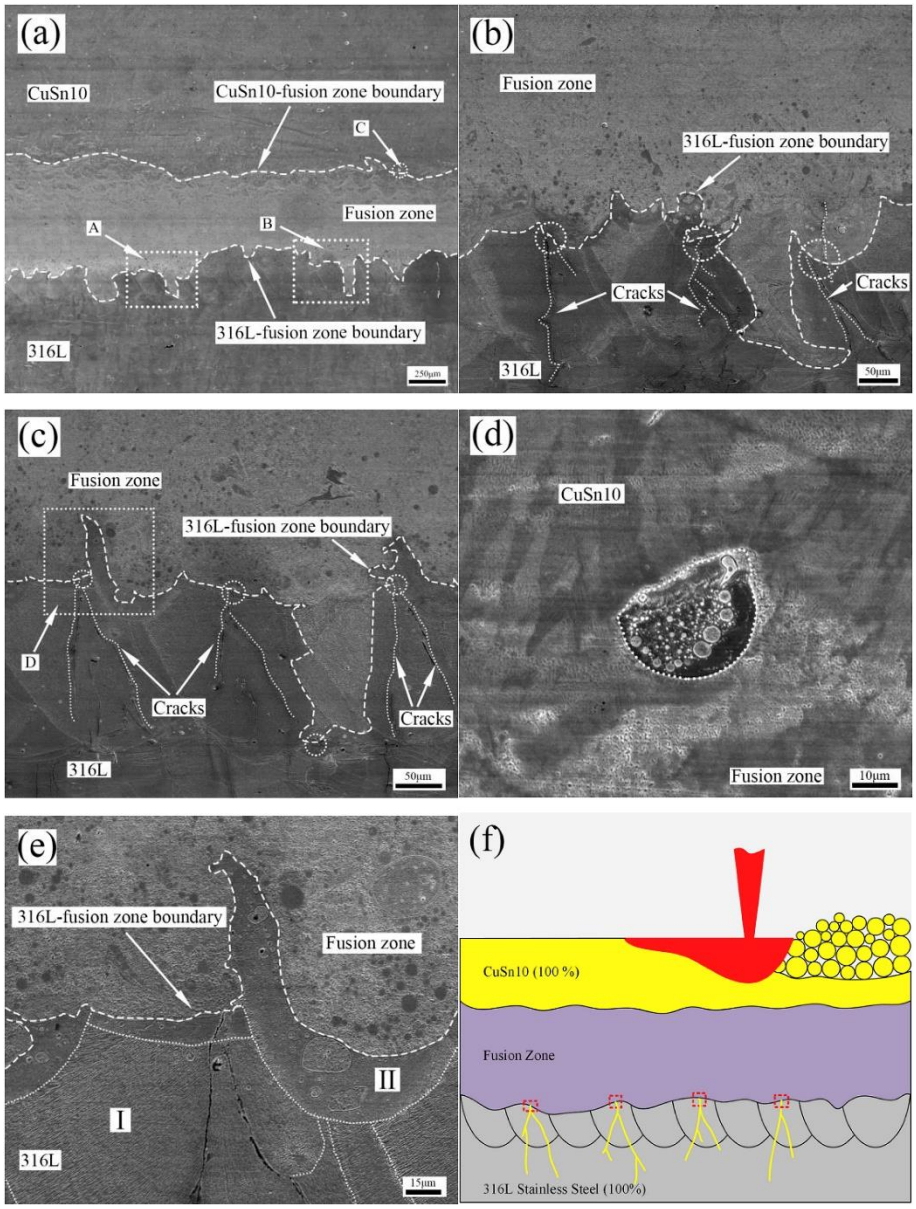

Figure 19 FE-SEM images showing the interface microstructure of SLM-formed steel/bronze: (a) entire fusion zone (100 ×), (b) area A of entire fusion zone (500 ×), (c) area B of entire fusion zone (600 ×), (d) area C of entire fusion zone (3000 ×), (e) area D of (c) (1500 ×), (f) schematic diagram of dendritic cracks [148].

Form the XRD results, it could be concluded that no intermetallic compounds are formed at the interface (Figure 26 (a)). The microhardness decreases from the 316L stainless steel region through the interface to the Cu10Sn region (Figure 26 (b)). Similar observations were made using the 316L stainless steel/C18400 material combination [14].

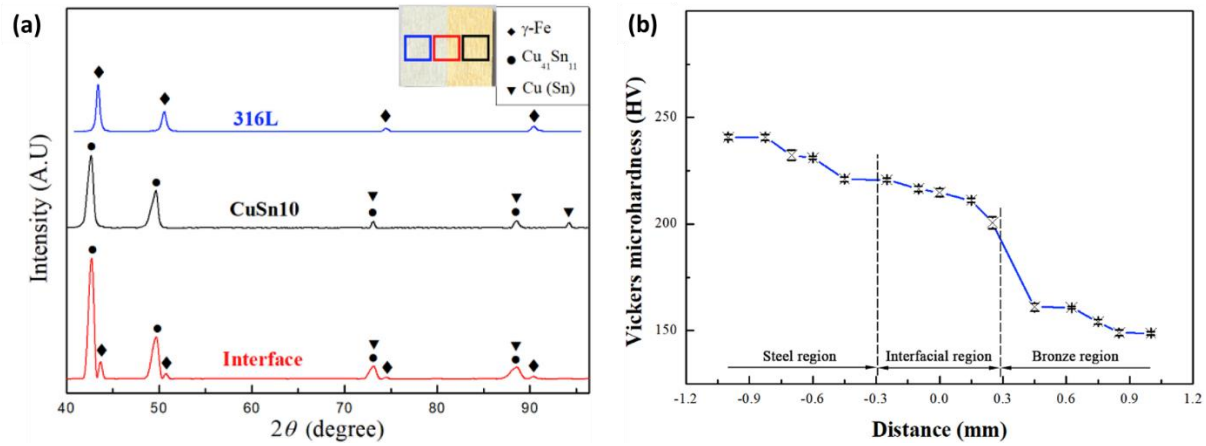

Figure 20 (a) XRD pattern of the 316L stainless steel, Cu10Sn and interface (b)Vickers microhardness along the interface [148].

A similar study was conducted on the fabrication of 316L stainless steel/Cu10Sn multi-metal components using L-PBF. The optimised parameters from other studies were used for 316L stainless steel while they optimise the parameters for Cu10Sn fabrication on 316L stainless steel [149]. Multi-metal samples formed using the optimised parameters are shown in Figure 21. Using optimised parameters for interface formation can results in good interfacial bonding with minimal cracks formation. It is also concluded that the multi-metal specimens could withstand a considerable degree of torsional stress in bending and shear directions.

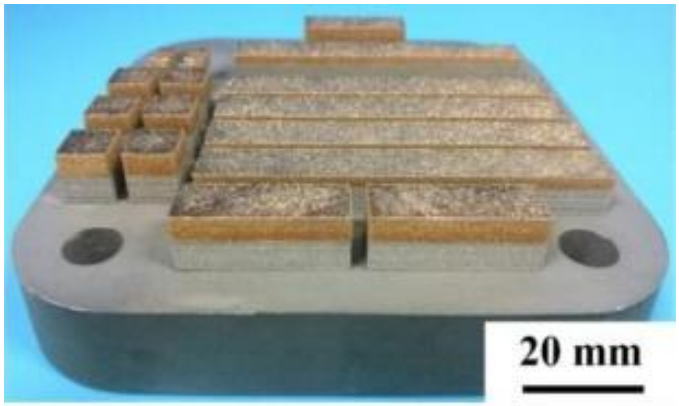

Figure 21 316L stainless steel/Cu10Sn multi-metal parts formed by L-PBF [149].

Morphology of CuSn/18Ni300 multi-metal system was also studied (Figure 22). Two kind of melt pools were observed in the 18Ni300 region which include columnar and cellular cells. These cells grew from the melt track boundaries and stopped growing when they reached the interface. At the interface, some small pores can be observed.

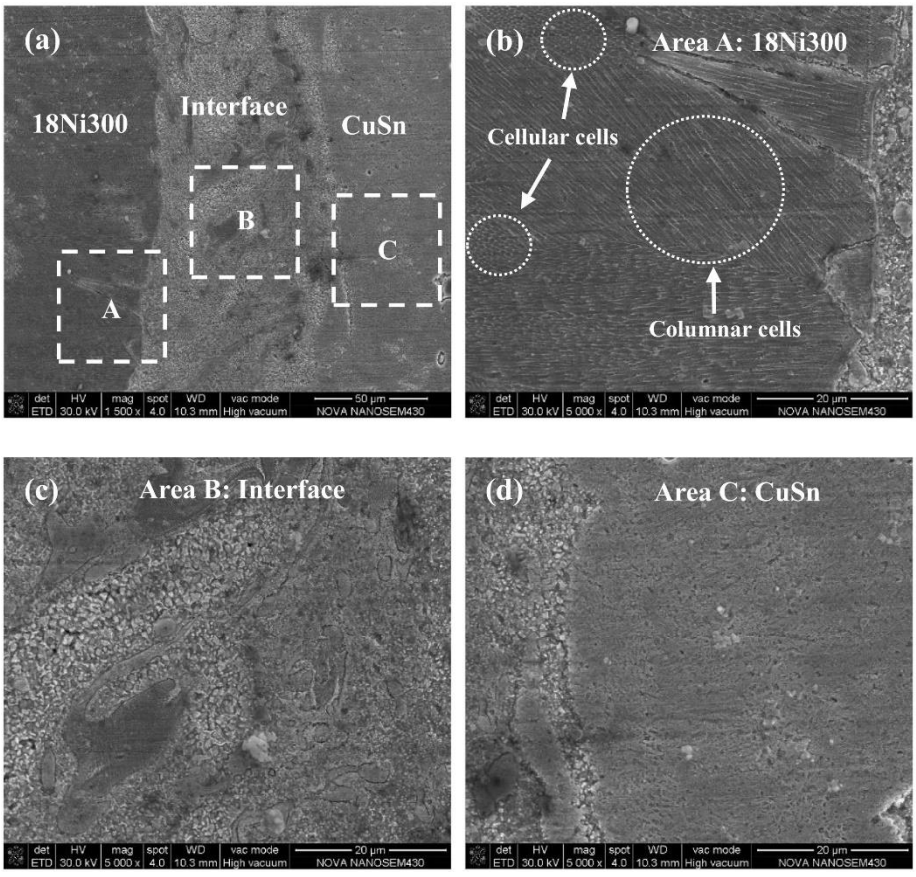

Figure 22 Morphology of CuSn/18Ni300 multi-metal system (a) CuSn/18Ni300 interface (b) high magnification of area A (c) high magnification of area B (d) high magnification of area C [150].

Using SEM-EDS, the mixing of α-Fe and α-Cu phase is observed at the interface, with some iron, copper, nickel, chromium, and titanium found in the CuSn region, indicating that diffusion has occurred during L-PBF (Figure 23).

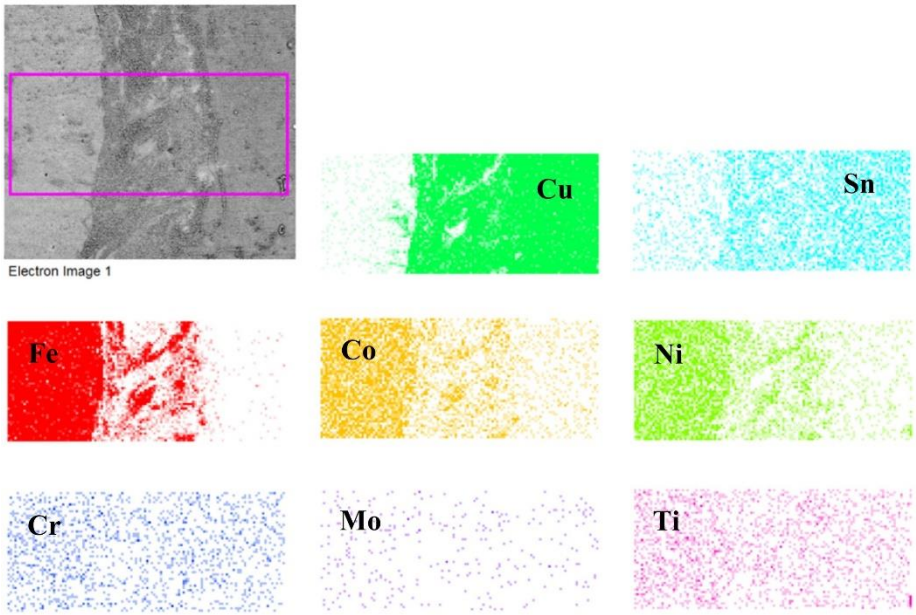

Figure 23 EDS results of CuSn/18Ni300 interface [150].

Bai *et al*. investigated the interface of the 316L stainless steel/C52400 copper system at both sides, i.e. at both the regions nearer to 316L stainless steel and C52400 as well [151]. Cracks are observed at the interface near the 316L stainless steel side due to stress mismatch, regardless of which material is deposited first (Figure 24).

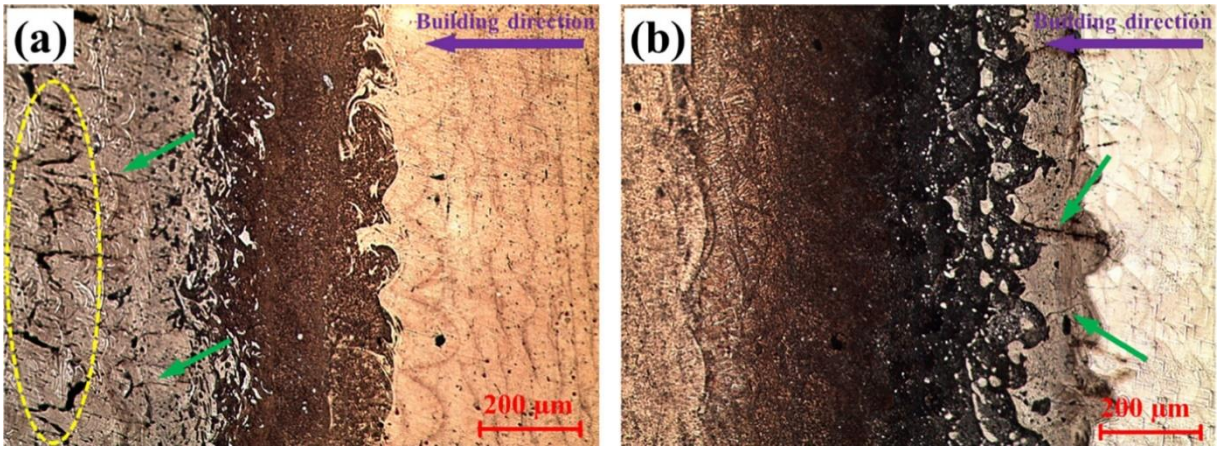

Figure 24 Cracks distribution at (a) the C52400/316L interface and (b) 316L/C52400 interface [151].

It can be known that C52400 is brought to the 316L side and vice versa at each of the interfaces which results in the mixing of both materials. However, the same material tends to segregate due to the difference in their surface tension and the rapid cooling (Figure 25).

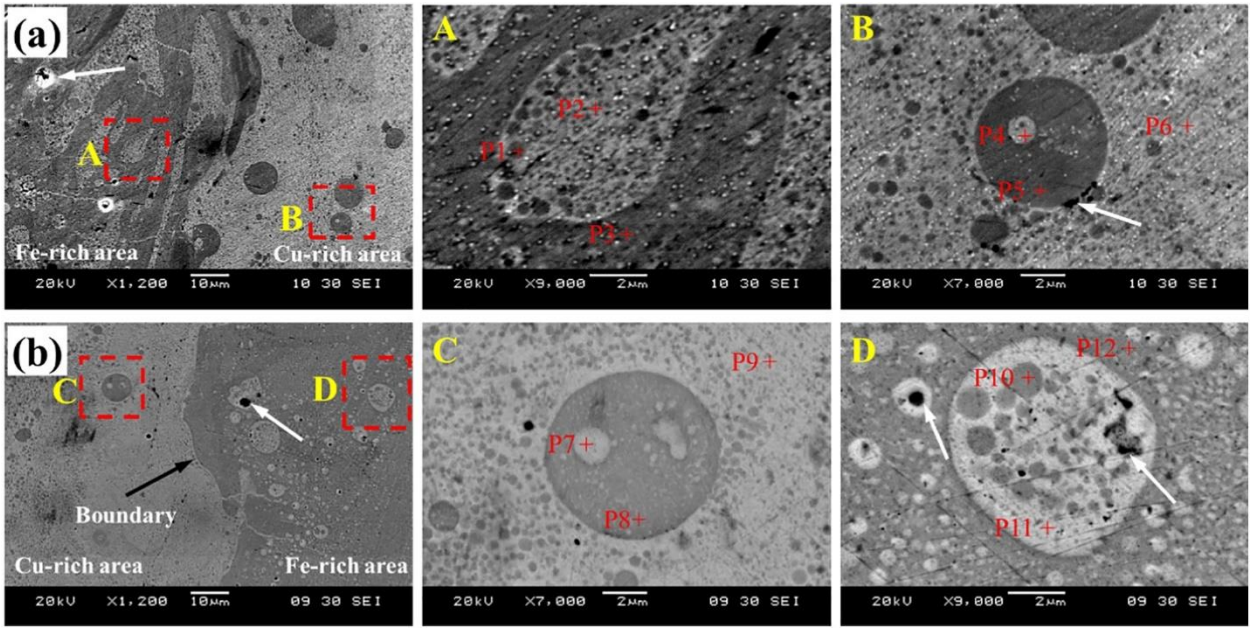

Figure 25 (a) Melt behaviour at the 316L/C52400 interface (b) at the C52400/316L interface [151].

Similarly, both interfaces are studied for the Inconel 718/316L stainless steel system using the sandwich design where Inconel 718 is built between 316L stainless steel [152]. It is shown that at both interfaces, uneven morphology is observed which can increase the total interface area and joint strength. Likewise, cracks are observed at the 316L stainless steel sides close to the interfaces.

Shakerin *et al.* studied the deposition of maraging steel onto H13 tool steel using L-PBF to form MS1-H13 bimetals. It was concluded that a very narrow interface was formed between the two types of steel without any cracks or discontinuities [153]. The EBSD analysis of the interface revealed a continuous joining between the two materials. The maraging steel exhibits a very fine microstructure in the first layer solidified on top of the H13 due to the rapid heat transfer form the melt pools to the substrate. After a few layers, the microstructure become slightly coarser due to

the higher temperature of the previously deposited layers (Figure 26 (a)). Further analysis using SEM clearly shows an interface region between the two materials and seems like the precipitates in the H13 were coarsened due to partial melting and subsequent mixing with molten powder, hence forming a partially melted zone (Figure 26 (c)) which also happens in fusion welding. Beyond the interface, the MS1 microstructure consists of similar morphology with melt pools accommodating coarse and fine equiaxed cells as well as columnar cells of submicron sizes.

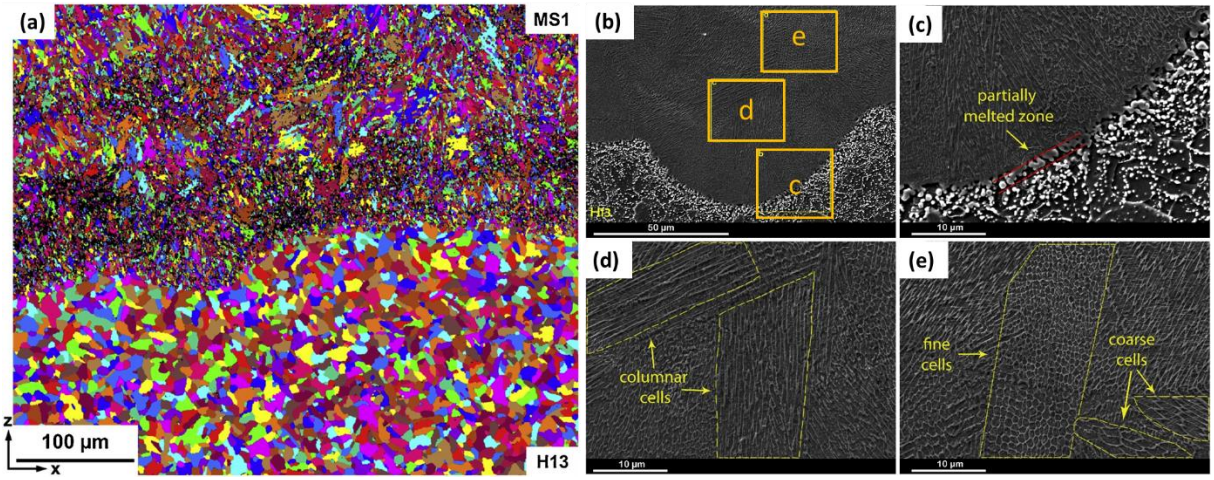

Figure 26 (a) EBSD unique color grain map and (b) scanning electron micrographs of the MS1-H13 interface with (c), (d) and (e) as magnified images of the different zones.

L-PBF techniques are favourable for the printing of intricate overhanging features such as those found in lattice structures [2, 154, 155]. This is because the overhanging regions can be supported by the unconsolidated powders bed from previous layers. Besides, L-PBF has better in-plane print resolution due to its smaller laser spot diameter of ~0.08 to 0.1 mm. Fabrication of lattice structures using multi-metal by L-PBF has been shown using 316L stainless/Cu10Sn (Figure 27) [149].

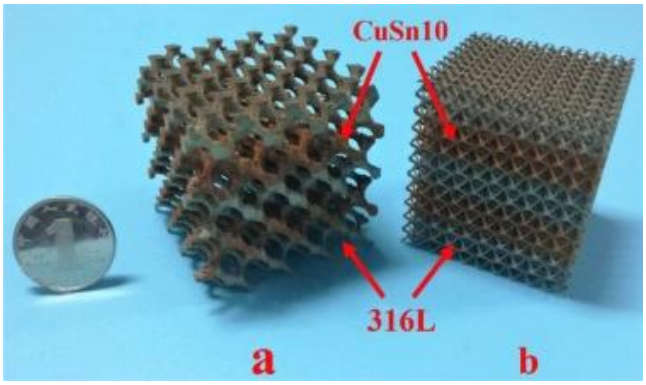

Figure 27 316 L/Cu10Sn lattice structure specimens with different unit sizes [149].

4.2 Aluminium and its Alloys

Demir & Previtali studied the multi-metal processing feasibility using pure iron and Al12Si. In the samples, the main defect within the deposited material appears as large cracks rather than porosity due to the lack of fusion or excessive melting. The proportion of cracks is influenced only by laser power and is attributed to the formation of FeAl intermetallic [144]. A study was conducted using AlSi10Mg/C18400 copper alloy system to investigate the interface characteristics [141]. FIB imaging was used to observe the interface which identified distinct copper-rich and aluminium-rich regions with an intermixed region at the interface due to the movement of elements assisted by diffusion (Figure 28). This is indicative of the dilution effect that are also observed in other multi-metal processing studies.

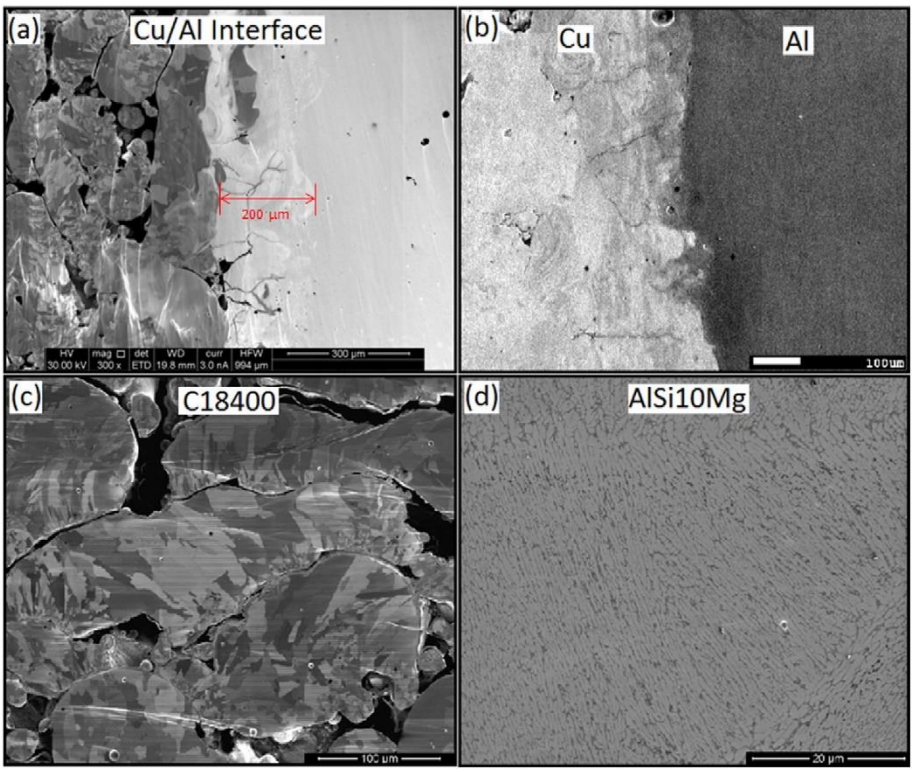

Figure 28 FIB image of Cu/Al interface; (b) SEM image of Cu/Al interface; (c) FIB image of copper; (d) SEM image of AlSi10Mg [141].

Like the 316L stainless steel/Cu10Sn system, cracks were also found in segments of the interface for the AlSi10Mg/C18400 system which is also attributed to the difference in thermal coefficients. However, using XRD, it is concluded that Al_2Cu intermetallic is formed which aggravated the cracks formation. The intermetallic compounds formed in the interface also led to anomalous readings for microhardness due to the precipitation of such compounds that are harder but more brittle (Figure 29).

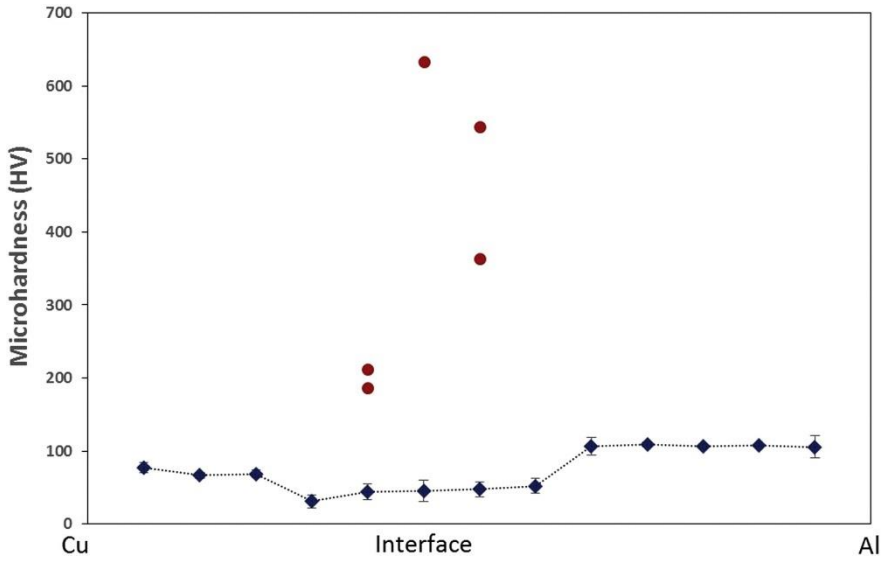

Figure 29 MIcrohardness variation along the Al/Cu interface [141].

Böhm *et al.* derived a theoretical model for the composition profile for multi-metal processing by L-PBF using AlSi10Mg and pure aluminum [156]. The model takes into account the dilution ratio as a function of the penetration depth of the melt pool, which is in turn dependent on the process parameters. A schematic of the resulting staircase composition profile across the interface due to the remelting of prior layers is shown in Figure 30.

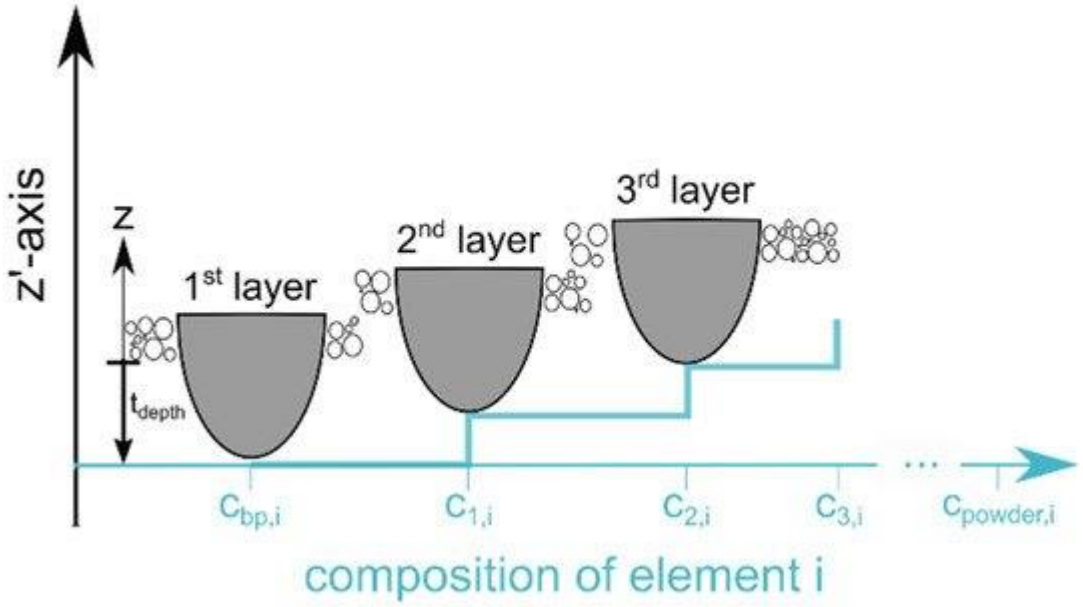

Figure 30 Staircare composition profile is depicted of the layers within the interface [156].

Multi-metal parts are fabricated by L-PBF of AlSi10Mg on AlCuNiFeMg substrate. SEM-EDS elemental analysis was conducted along the interface and it showed that successful partial melting of the substrate and the mixing of the AlSi10Mg with the AlCuNiFeMg occurred, resulting in sound metallurgical bonding at the interface [157].

4.2 Titanium and its Alloys

In order to understand the effect of processing parameters for multi-metal processing, Wang *et al.* studied the formation mechanisms of TiB_2 tracks on Ti6Al4V by L-PBF [158]. The melt pool geometries and surface morphology of the melt tracks were analyzed. It is found that the shape of the melt pools depends on the laser-powder interaction. When energy transfer efficiency is larger than the material absorptivity, keyhole is formed, leading to the formation of deep and narrow melt pools.

Wei *et al.* studied the formation of multi-metal system using Ti5Al2.5Sn/Ti6Al4V. Due to the optimized parameters used, good metallurgical bonding was observed at the interface without any

pores, cracks and lack of fusions [159]. At the interface, diffusion of elements is observed as indicated by the gradual decrease in tin from Ti5Al2.5Sn to Ti6Al4V region, and vice versa for the vanadium (Figure 31).

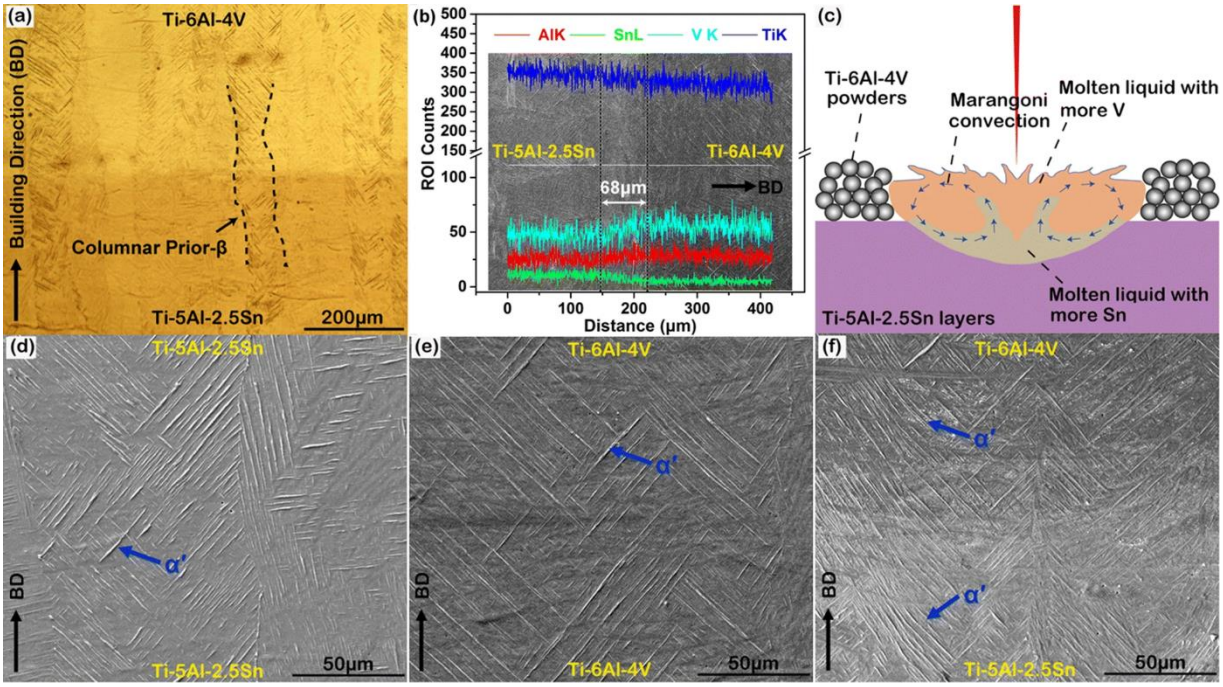

Figure 31 Microstructure characterizations of the as-built Ti5Al2.5Sn/Ti6Al4V multi-metal sample (a) OM image (b) EDS line scanning result showing the element distribution around the Ti5Al2.5Sn/Ti6Al4V interface (c) Schematic diagram showing the formation mechanism of the element diffusion (d) SEM image of the Ti5Al2.5Sn layers (e) SEM image of the Ti6Al4V layers and (f) SEM image showing the microstructure around the Ti5Al2.5Sn/Ti6Al4V interface [159].

Due to the presence of the interface, there is no abrupt change in the microhardness between the two titanium alloys (Figure 32), which agrees with the results observed with other material systems.

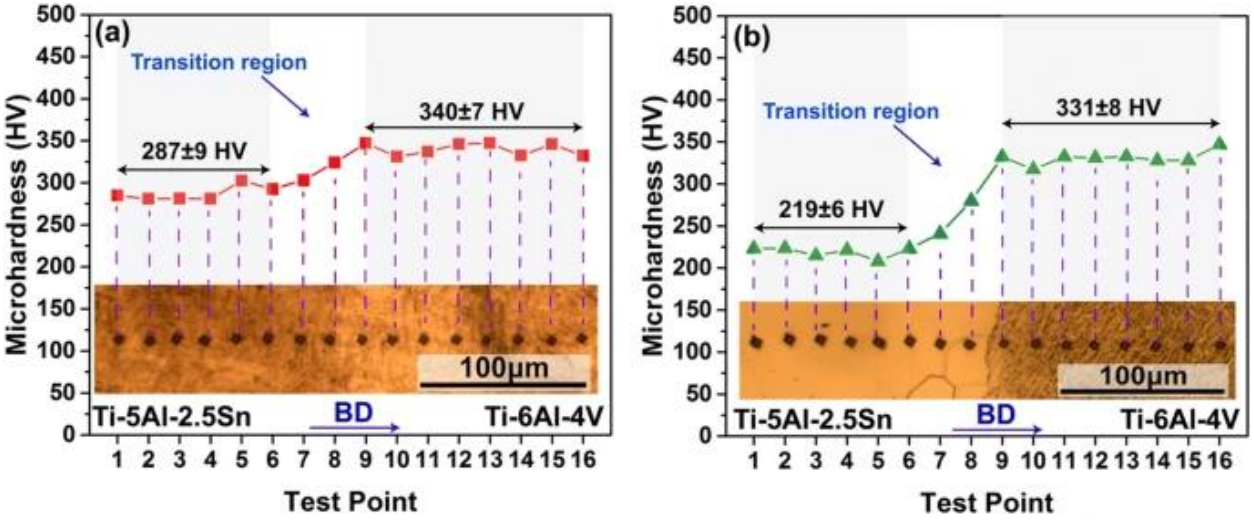

Figure 32 Microhardness distributions around the Ti5Al2.5Sn/Ti6Al4V interface of the dissimilar titanium alloy samples under different processing states: (a) as-built (b) after heat treatment [159].

The multi-functional concept for L-PBF produced parts is shown possible by fabrication of cellular structures using NiTi/Ti6Al4V multi-metal system [160]. This allowed the allocation of specific functions that are localized and the design concept for a multi-metal hip implant is shown in Figure 38. SEM images show the successful transitions from NiTi to Ti6Al4V with nano-indentation results showing an interface region between the two materials.

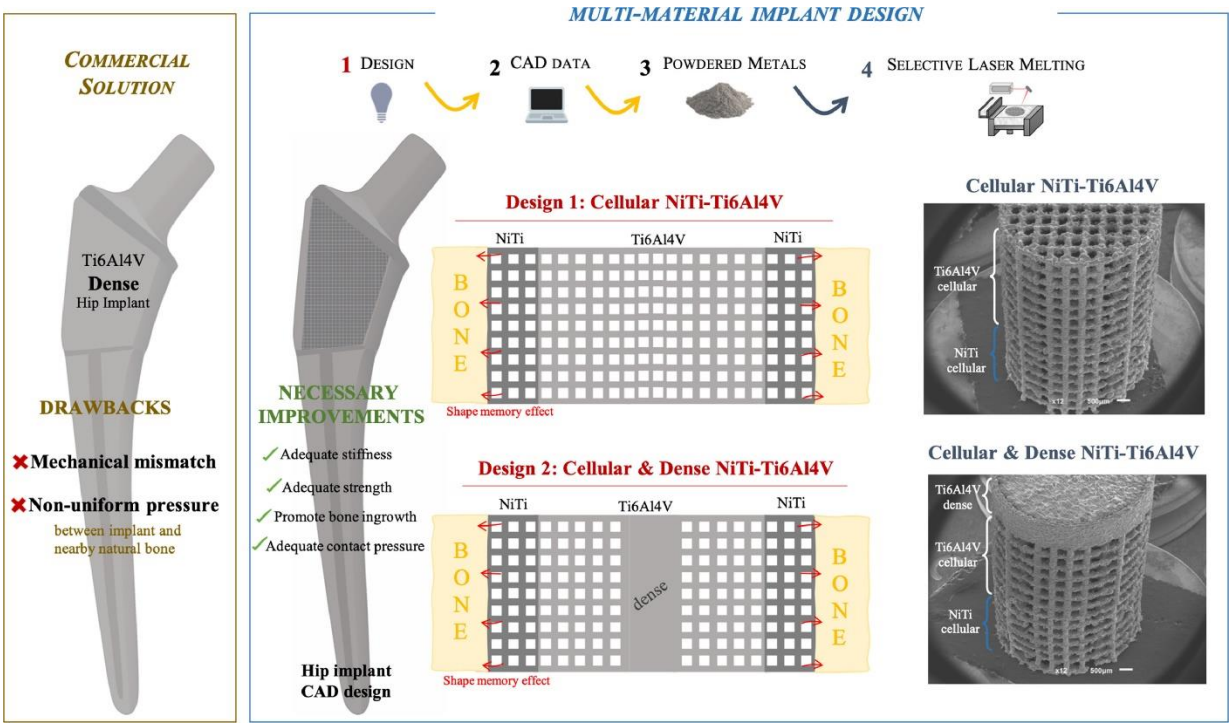

Figure 33 Design concept of a NiTi/Ti6Al4V multi-material hip implant [160].

5 Challenges in *In-Situ* Alloying and Multi-Metal Processing by Laser Powder Bed Fusion

Functional applications of L-PBF parts largely depends on whether they are defect-free. However, many metallurgical defects in L-PBF, such as balling, porosity, cracking, and oxide inclusions remain as challenges. Furthermore, with *in-situ* alloying and multi-metal processing, there are additional complications such as loss of alloying elements, intermetallic phases, and unmelted particles. Though efforts have been made to develop the solutions, many unknowns are still involved. In the remaining parts of this section, each of these defects is elucidated by highlighting the mechanism of their formation, main influencing factors, and the potential remedial measures.

5.1 Balling

Balling is a phenomenon which decreases the surface quality of L-PBF parts. It is a typical L-PBF defect and can be divided into two types: (1) ellipsoidal balls of about 500 μm that are formed

as a result of broken melt tracks. These are resulted from the insufficient wetting ability to the substrate previous layer, as discussed previously. Both severe oxidations of the melt pool or low energy input could also result in worsened wetting characteristics [60]. Hence, the atmosphere during L-PBF is typically controlled by flooding of inert gases, such as argon or nitrogen. Stacking of these large balls results in scratching of the recoating blade or roller and hinders the movement of the recoater, thus, stop the production process. (2) The spherical balls of about 10 μm are formed due to a reduction in surface energy of liquid at short length scales by splashing of melt pools [161]. Both types of balls impede the uniform deposition of new powder on the previous layer and tend to cause defects, such as porosity and crack, which would be addressed in later sections.

Balling effect is mainly affected by the wetting characteristics of the melt pools, which are in turn affected by the processing parameters. Hence, the selection of these parameters must take into consideration the material physical properties. Balling effect also depends on the powder preparation methods which determine the powder feedstock quality. The feedstock affects the thermal absorptivity and transfer behavior which can cause significant evaporative recoil pressure in the melt pools. This causes melt instability, which results in balling [162].

Balling can deteriorate the surface quality of L-PBF components, hence, in addition to parameters optimization, re-melting, and post-process treatment, including polishing, may be needed.

5.2 Porosity

Porosity is a common feature in many metallurgical processes, which include L-PBF. The pore-forming mechanisms for L-PBF include lack of fusion porosity caused by insufficient melting and gas entrapment. Lack of fusion is due to insufficient overlapping of melt tracks or penetration of the laser into the powder layers due to low laser power, high scanning speed, large hatch spacing, and large layer thickness. The sources of entrapped gases can be the gas used to flood the chamber

(shielding gas), vapor due to vaporization of the powder bed, and gases trapped within the powder particles during the powder production [163]. Gas entrapment can also be due to turbulent flow in the melt pools.

Porosity is also commonly encountered in *in-situ* alloying with L-PBF and is shown in a study by Fischer *et. al* [105]. Ti40.5Nb (wt%) was studied and a laser with discontinuous scan mode was used. As the volumetric ε increases, the cause of porosity transits from lack of fusion to having a minimum amount of porosity and finally to keyhole formation. The increment in ε changes the melt pool formation mechanism from conduction mode to keyhole melting, subsequently causing an increased aspect ratio of the melt pool and lead to a higher probability of keyhole porosity formation. An illustration of the effect of melt pool aspect ratio on keyhole porosity is shown in Figure 34.

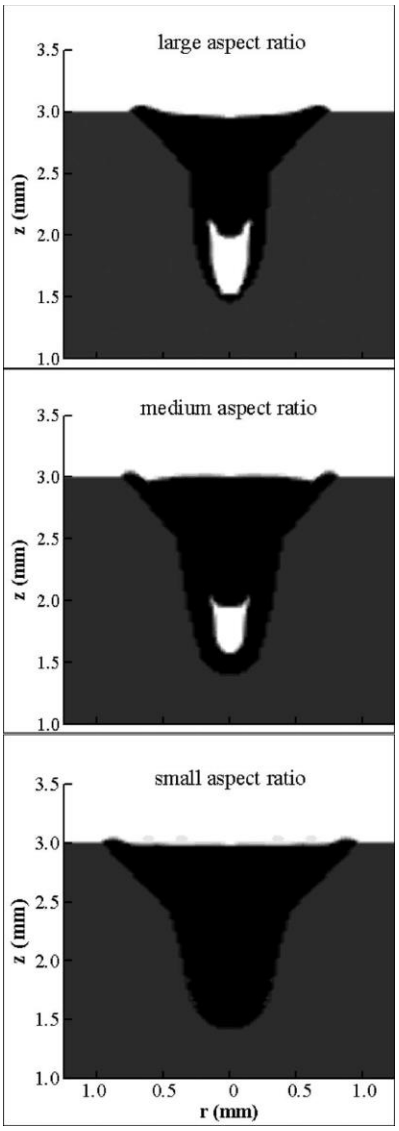

Figure 34 The effect of melt pool depth-to-width ratio on pore formation [164] The effect of melt pool depth-to-width ratio on pore formation [164].

It is found that for mixed powders, each component powders must be melted to enable chemical mixing in a liquid state as compared to using pre-alloyed powder [64]. For the case of aluminum-silicon alloys system, silicon has a higher melting point which makes it more difficult to create sufficient melt pools when the silicon fraction increases. Higher laser power is necessary to melt the silicon powder which can cause melt pool instability and results in the keyhole induced porosity (Figure 35). Melt pool instability is due to fluid forces that leads to effect such as Reyleigh instability, causing discontinued melt tracks.

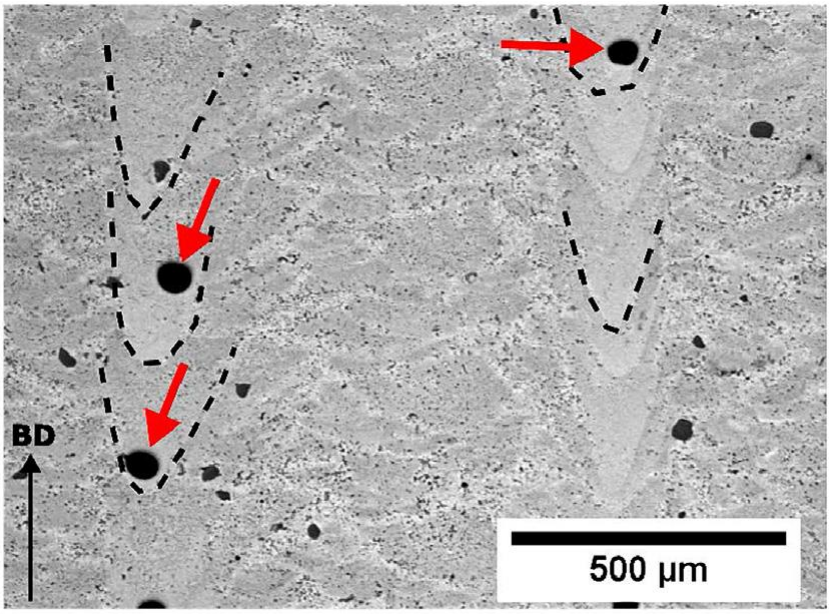

Figure 35 Micrograph of AlSi25 sample produced at 400W and 2000 mm/s, some melt pools are marked by dotted lines, and keyhole porosity is indicated by red arrows, BD is building direction [64].

The two main pore-forming mechanisms can be identified by the location of the pores, with the former type outside the melt pool while the latter inside the melt pool. Bubbles or pores are formed in a way to balance the vapour pressure with surface forces, resulting in surface movements [165]. Both types can be resulted from the change in the melt pool flow pattern which is controlled by forces such as gravitational force, vapor pressure and thermal capillary forces exerted on the metallic/gaseous interface. The aforementioned balling effect deteriorates the recoating of the new layer and may result in unmelted powder particles entrapped in defective positions such as the neighbouring melt tracks.

Cave-like pores and open pores formed on the top surface of the track is illustrated in Figure 36. The cave-like pores appear to be formed by the unstable melt flow moving away from laser scanning direction where the melt was solidified in the air before fusion with the previous layer thus creating a hole beneath. Open pores or discontinuities on the L-PBF produced surfaces could be due to the splashing of the melt pools or lack of materials filling in at some localised sites. The

cave-like pores mainly remain as pores because of the coverage, while the open pores could be either filled with melt materials during the next scanning or remain as pores. Simulations done by Qiu *et al.* [165] and Khairallah *et al.* [166] proved the existence of these pores due to the unstable melt.

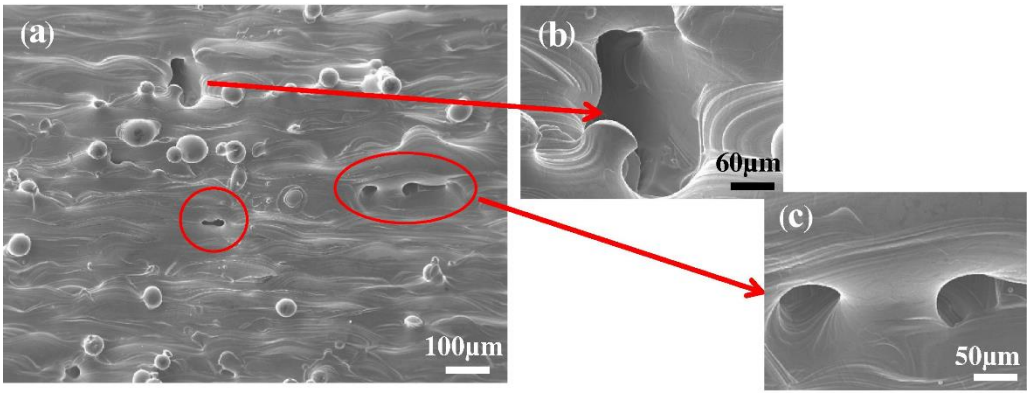

Figure 36 SEM micrographs showing the variation of the top surface structure of as-SLMed Ti-6Al-4V samples with powder layer thickness 60 μm [47].

Materials vaporization during L-PBF results in keyhole pores formation. These pores are typically reported to be spherical and located at the tail end of the melt pools if they failed to escape [167]. Figure 37 illustrates the entrapping process of keyhole pores and their positions for laser welding. Large bubbles were intermittently formed at the bottom of the keyhole as the shape and depth of the keyhole fluctuated violently. They end up floating and remain as pores in the rear of the melt pools if they fail to escape before the melt pool solidify.

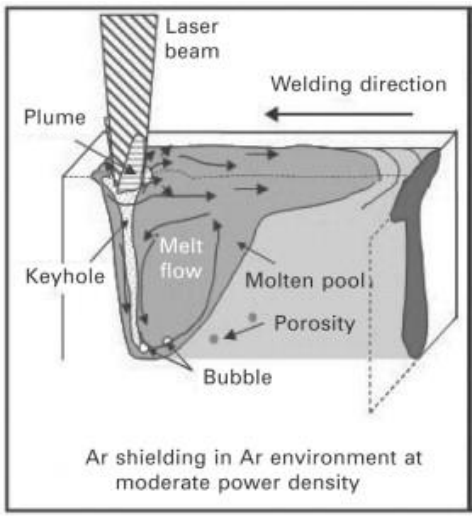

Figure 37 Schematic representation of melt flows in the melt pool and weld bead geometry, showing keyhole pore formation and distribution [168].

Surface moisture on the powder particles can release hydrogen during L-PBF. Hydrogen gas is mainly released near the solidification front of the melt pool as the dissolution of hydrogen decreases with decreasing temperature (Figure 38). For a high solidification rate, i.e. high scanning speed, the solubility is increased [169]. Hydrogen porosity can be reduced when internal drying process is used [65, 169]. Internal drying process can be achieved by re-melting with a lower laser power used during the first scanning. In such a case, a higher drying temperature is attained which lowers the moisture level, thus achieving internal drying process and reducing the pore density. Gases entrapped inside the powder particles during the powder atomization process can lead to pores as the gas is easily entrapped in the melts and can be eliminated by refining the powders [163].

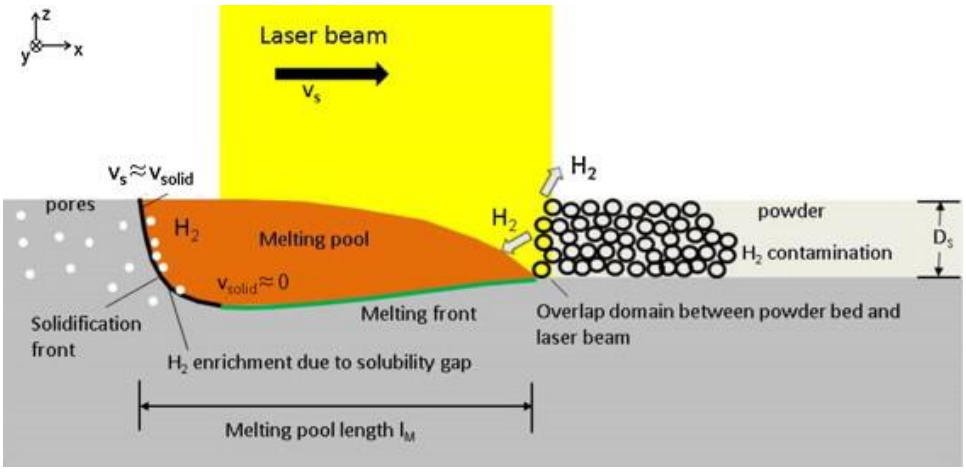

Figure 38 Schematic overview of the interaction zone between laser radiation and powder [169]. Schematic overview of the interaction zone between laser radiation and powder [169].

The above porosity formation discussions are all based on the stability of the melt pools and/or the fluid flow forces. In addition, Gu *et al.* also used different shielding gases (argon, helium, and nitrogen) to demonstrate the importance of melt flow on gas formation [170]. The unstable fluid flow in the melt pool can be identified by the range of the parameters. Kasperovich *et al.* showed that scanning speed has the most dominant influence on the porosity fractions (Figure 39) [167]. The laser power has a significant effect on the resulting defect densities and also shows a distribution with an optimal parameter range allowing minimal defects (Figure 39c). High scanning speed and low laser power are associated with the lack of fusion pores while keyhole pores are attributed to low scanning speed and high laser power. While the hatch distance was found to be least sensitive (Figure 39b), it should be noted that only the porosity in the melt pools is analysed.

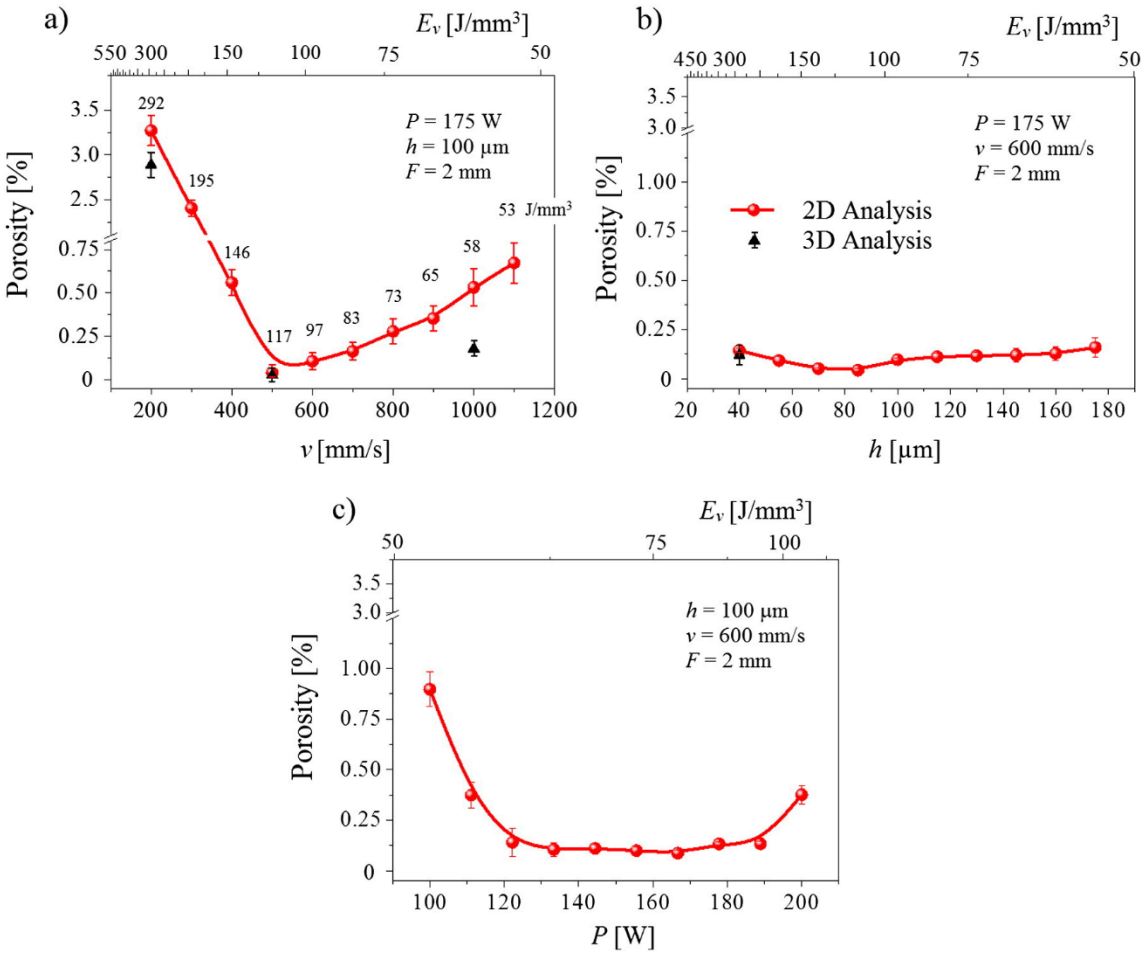

Figure 39 Influence of the SLM process parameters on the total porosity (2D measurements) as a function of (a) scan speed v, (b) hatch spacing h, and c) laser power P. The volume energy density Ev, is included in the upper abscissae [167].

5.3 Crack

The crack types in L-PBF can be categorized into hot crack and cold crack. Hot crack, also known as solidification crack, can be formed at the late stage of solidification when grains form continuous skeletons. Two phenomena account for hot crack initiation, (1) temperature differences during solidification with large temperature range resulting in insufficient convection in the liquid region and (2) solid deformation. Crack initiation and growth are prevented and the effect of entrapped liquid is reduced by fine equiaxed semi-solid structures which allow easier grain rotation and deformation than dendrites.

Cracks caused by residual stresses are more commonly for L-PBF. Residual stresses in L-PBF are caused by two possible mechanisms, temperature gradient mechanism (TGM) and cool-down phase of the molten top layers. The first mechanism is illustrated in Figure 40. A steep temperature gradient is developed just beneath the laser spot when a laser beam is stroked onto the surface layer due to rapid heating and slow heat conduction. Compressive stresses in the upper layers are formed as the expansion of the upper layer is restricted by the cooler underlying solidified layer. The compressive stresses in the material cause plastic deformation when the yield strength is reached, which remain in the absence of mechanical constrain. During cooling, this compressive state is converted into residual tensile stresses and a bending angle towards the layer beam develops. Those residual stresses may induce cracking [171, 172]. The melted top layers tend to shrink due to the thermal contraction. This deformation is again prohibited by the underlying layers, thus introducing tensile stresses in the top layer and compressive stresses below [173, 174].

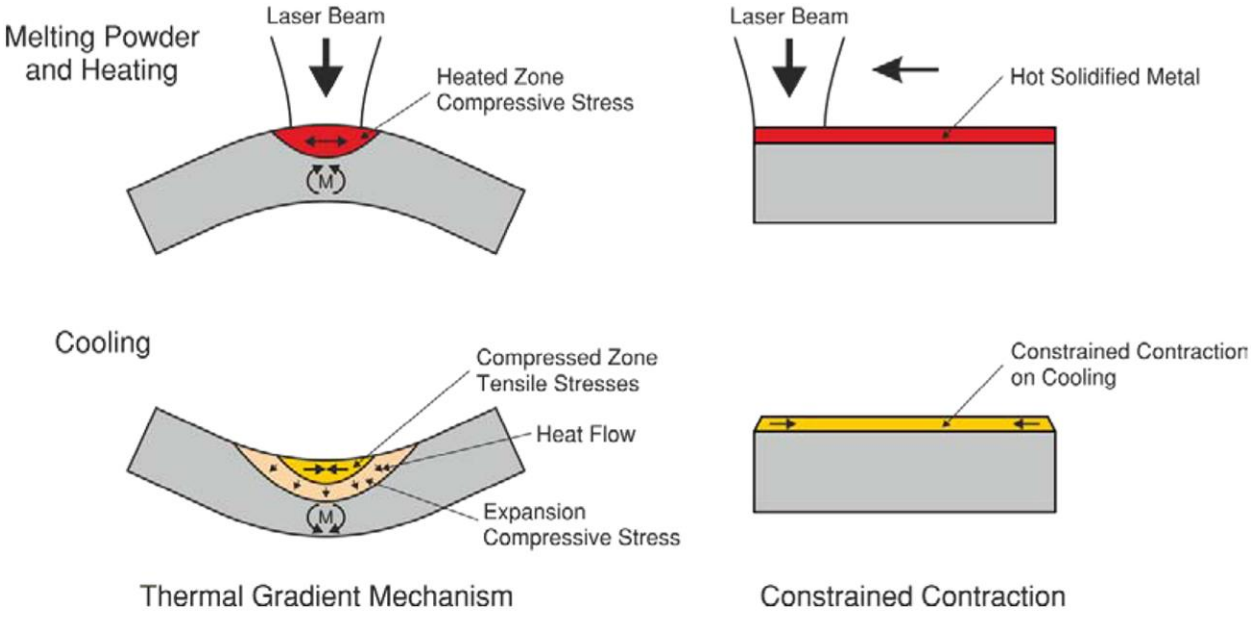

Figure 40 Temperature Gradient Mechanism in L-PBF [174].

Cracking and interlayer de-bonding can occur as residual stresses are larger in the direction perpendicular to the scanning direction than along scanning direction [69]. The level of residual

stress depends on material properties especially the elastic modulus and CTE. Thermal stresses in multiphase materials were discussed because of internal constraints caused by different CTE between the phases. If the thermal expansion is hindered by external constraints or uneven temperature distributions, bending stresses (σ_b) proportional to the average CTE are generated [175]:

$$\sigma_b = -\frac{6}{L^2}\int_{-L/2}^{L/2} E\alpha_t\,\Delta T X'\,dx \tag{5}$$

where L is the layer thickness, E is the elastic modulus, α_t is the average CTE of the composite, ΔT is the temperature difference and X' is equal to $x - L/2$, x is the distance measured from the layer surface. The average CTE of a multi-phase material (α_t) is derived as follows based on the Turner Equation:

$$\alpha_t = \frac{\alpha_1 V_1 K_1 + \alpha_2 V_2 K_2 + \alpha_3 V_3 K_3 + \cdots}{V_1 K_1 + V_2 K_2 + V_3 K_3 + \cdots} \tag{6}$$

where V is the volume fraction, K is the bulk modulus and α_i is the CTE of each phase. According to Eq. (10), lower elastic modulus and average CTE which depends on the particular CTE and volume fraction of the material constituents, favor less stress. Taking into consideration of the compatibility between the dissimilar metals for multi-metal processing, close CTE between them is preferred. This is also true for *in-situ* alloying by L-PBF as the constituent element particles that are unmelted can have restricted expansion and/or contraction, causing residual stresses. Crack formation was found to be reduced with increasing laser power and/or decreasing scanning speed, which correlates with increasing energy density. However, increasing energy input leads to the formation of keyhole porosity. Thus, there must be a balance between crack formation and porosity [64].

Crack formation is also attributed to high thermal stresses during L-PBF as a result of steep thermal gradients, fast cooling rates as well as CTE mismatch between the substrate and *in-situ*

alloying materials [64]. Mercelis *et al.* established a relationship between residual stresses and the height of the sample and substrate, scanning strategy, and heating conditions in 316L stainless steel [176]. Although the quantitative results cannot be simply extrapolated to other materials, most qualitative results can be generalized. For instance, the length and direction of scanning vectors can redistribute the stress profiles. Residual stresses can also be controlled by the preheating of the build substrate due to the decrease in the temperature gradient. This can be useful during multi-metal and *in-situ* alloying. Cracks at the interface and surface warpage are observed in 316L stainless/Cu10Sn samples, as shown in Figure 41. The crack initiations at the interface are said to be caused by rapid solidification of the liquid phase copper which sharply tore the solid phase steel due to a large difference in CTE [149]. Liu *et al.* also attributed the cracks formation due to the infiltration of copper into the austenitic grain boundaries of steel [14].

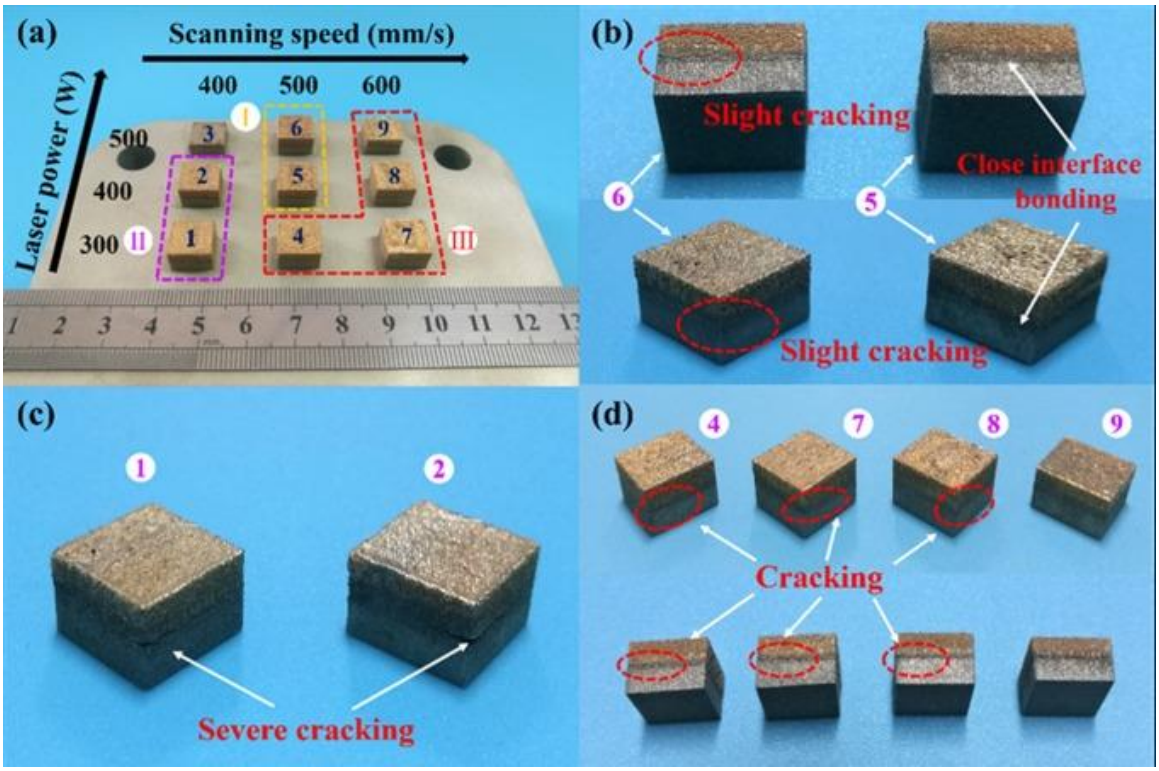

Figure 41 316L stainless steel/Cu10Sn specimens by L-PBF. (a) parameters used in L-PBF (b) Group I with slightly cracked interface (c) Group II with severe cracks at the interface and over melting at top surfaces (d) Group III with well-fused surfaces with varying degree of cracks [149].

Densification is facilitated by high temperature as the effect of low viscosity on wettability is compromised. However, cracks caused by residual stress is thus induced due to the high energy input and temperature gradient. Zhu *et al.* demonstrated that the thermal shrinkage during laser melting was increased with increased laser energy input under a cool-down phase mechanism [177].

L-PBF processing parameters should be manipulated with care to reduce the residual stresses. It is noted that the powder preparation also has an effect on residual stresses. Powder distribution will affect the thermal behavior, thus influencing the stability of the melt pools. However, more detailed research is needed as for now only AlMangour *et al.* found that ball-milled powders induce larger and more severe cracks than directly mixed powders, although the latter one revealed deep groove and pores [178].

Cracks and porosity can be formed due to the presence of uncompressed powders. It can be minimized by increasing the packing density of the powder with a roller compressor during the powder spreading process [179]. For in-plane multi-metal parts, the formation of cracks could also be due to the solidification-order of the dissimilar materials. Anstaett *et al.* investigated the in-plane joining of tool steel 1.2709 (X3NiCoMoTi18-9-5) and 2.1293 CuCr1Zr (CCZ) and they have found that cracks form only when CCZ is scanned first but no crack is observed when the tool steel is scanned first [139]. The crack formation within the CCZ section could be attributed to the inclusion of iron particles from the tool steel. Cracks can form when the multi-metal parts are not processed at an appropriate cooling rate. Beal *et al.* have shown the copper favours the formation of cracks within the linearly mixed compositional gradient of H13 tool steel and copper as it increases the cooling rate of the multi-metal parts [140]. Chen *et al.* showed that microcracks can form at high laser energy input due to the huge thermal gradient at the interface; whereas pores

can form at low laser energy input due to the inability of the high viscosity metal liquid to flow into the voids between the particles at a lower operating temperature [142]. The formation of large cracks between the two dissimilar materials can also be due to the low compatibility and miscibility of the two materials [144].

5.4 Loss of Alloying Element

Significant vaporization for volatile elements with higher equilibrium vapor pressure such as magnesium, zinc, lithium, and aluminum can occur during L-PBF due to the high temperature of melt pools. Figure 42 plots the equilibrium vapor pressure of some metals at different temperatures. Selective vaporization of elements will result in a change in the composition of the components and degrade the mechanical properties, such as reducing strength, elongation, hardness [180], corrosion resistance, and increasing crack susceptibility [181], which would affect the 3D printability. According to Collur *et al.*, the vaporization mechanism can be divided into three stages, transport of vaporization elements from the bulk to the surface of the melt pool, followed by the vaporization at the liquid/vapor interface and transport of the vaporized species into the surrounding gaseous phases [182].

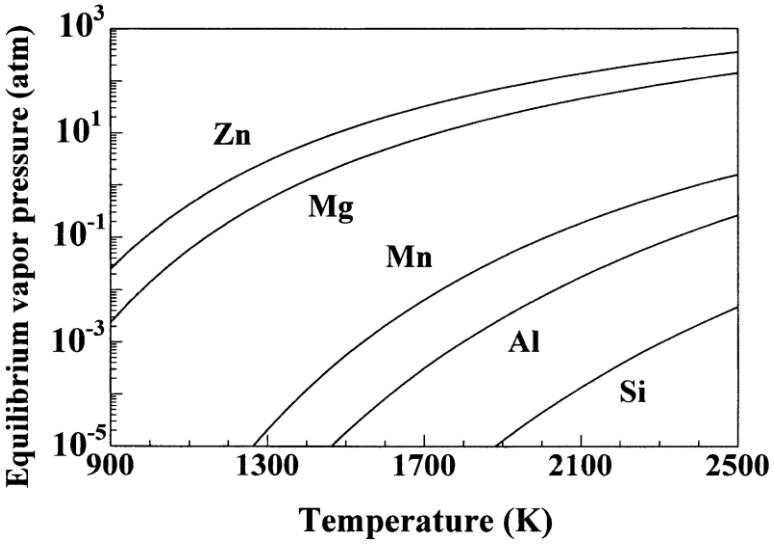

Figure 42 Equilibrium vapor pressure of metals at different temperatures [181].

Like welding process, the change in composition during L-PBF depends on the vaporization rate and the volume of the melt pools. Although the rate of vaporization increases with laser power, the change in composition is most pronounced at low laser powers because of the small size and, consequently, the high surface-to-volume ratio of the melt pools. The high scanning speed ensures a shorter time span of the melt pools and reduces vaporization [183].

In a study to *in-situ* alloy Al50Si (wt%), the resultant part shows higher silicon content due to aluminium evaporation [65]. It was observed that the extent of aluminium evaporation increases with the input ε. The hyper-eutectic composition resulted in microstructure with primary silicon and eutectic silicon. Like *in-situ* alloyed Al12Si, increasing ε leads to sustained melt pool which causes silicon precipitation out from the saturated Al(Si) solid solution. By lowering the cooling rate, the size of the primary silicon phase increases from a mean diameter of 3.12 μm to 7.31 μm with laser power from 260 W to 350 W. During L-PBF for Al 7075, evaporation of zinc and magnesium can occur and reduces the overall strength, however, the problem of volatile elements evaporation can be compensated via adjustment for the raw material used [71]. If ε was to be increased further to promote melting and mixing, the recoil pressure from vaporized metal can lead to the formation of keyhole porosities. During the *in-situ* alloying of nickel-titanium, an exothermic reaction between titanium and nickel can lead to turbulent melt pools and it was hypothesized that selective ejection of particles might have occurred during L-PBF, leading to depletion of titanium in the manufactured part [123]. In another study done using a magnesium-aluminium alloys system, it is found that with high energy input, the powder was evaporated due to the low boiling point of magnesium. These vapor magnesium then oxidised to form MgO. Lack of fusion was obtained at low energy input [133].

5.5 Oxide Inclusions

The densification and performance of L-PBF parts can deteriorate due to oxide inclusions. During L-PBF, oxidation can occur on the surface of the melt pools or as a result of entrapped gas due to the turbulent flow in the keyhole position through the reaction with the oxygen impurity in the shielding gas. Simonelli *et al.* compared the composition of starting particles of 316L stainless steel, AlSi10Mg, and Ti6Al4V directly with the laser spatters generated during L-PBF. Oxide films on the surfaces of 316L stainless steel and AlSi10Mg spatters are observed, however, there was no oxidation on that of Ti6Al4V [42]. The oxides are underpinned by surface enrichment of the most volatile element present in the alloys because no oxides were observed in the bulk microstructure of the spattered material. If these elements (manganese and silicon in 316L stainless steel, magnesium in AlSi10Mg) have a great affinity with oxygen, oxides can be formed. Magnesium oxide films in aluminum alloys contain spinel ($MgO.Al_2O_3$) and MgO depending on the magnesium contents. However, the protective oxide layers are thinner in 316L stainless steel and titanium alloys than in aluminum alloys and have a negligible effect on L-PBF, because they can be disrupted and stirred into the melt pool or vaporized by the laser beam [184]. Since aluminum has a greater affinity to oxygen and can form thicker oxide films, with dissociation pressure of alumina being rather low (10^{-52} pO2) at the melting point of aluminum, oxide films cannot be avoided at low oxygen concentration. Therefore, most researchers focus on aluminum components formed by L-PBF. There are two sides for oxide films, wetted side and dry side. The wetted sides may nucleate intermetallic compounds while the unwetted dry sides are potential nucleation sites for porosity. Hence, most oxide films are at the pore boundaries [57]. As aluminum dendrites may not grow through the dry side of oxide films, oxides may also be distributed at the grain boundaries. Oxide films are always folded dry side to dry side as observed in convectional castings and laser-welded aluminum alloys [185, 186].

Measures must be taken to eliminate the oxide films because they not only degrade the densification behavior but can also initiate cracks [187]. High energy density is required to break up the oxide films. However, only the oxide films at the bottom of the melt pools can be interrupted due to stronger Marangoni flow. Those at the sides of the melt pools remain intact, creating the oxides "walls". Therefore, new methods of controlling the oxidation process and disrupting oxide films formed within the components, for example, scanning strategy optimization, should be further developed. The higher energy density employed seems to be more effective in breaking up the oxide films though it induces a higher affinity to oxygen. However, no comparable data has been offered for *in-situ* alloying and multi-metal processing by L-PBF.

5.6 Interfacial Phases and Unmelted Particles

Interfacial phases and unmelted particles are common challenges for *in-situ* alloying and multi-metal processing by L-PBF. During the *in-situ* alloying of titanium-niobium, the amount of unmelted niobium decreases as the ε increases which leads to the formation of parts with better compositional homogeneity [105]. The trend of porosity and unmelted niobium with increasing ε are illustrated in Figure 43. When a certain minimum ε threshold is crossed, ε increment generally leads to a better dissolution of niobium particles but induces more keyhole porosity. It is of interest to note that the issue with *in-situ* alloying of titanium-niobium via L-PBF is that, the minimum porosity parameters do not necessarily lead to a homogenous part (Figure 44 SEM of Ti-40.5Nb at different energy density a) 39 J/mm³ b) 214 J/mm³). However, the formation of Marangoni convection induces capillary forces which are said to aid the dispersion of magnesium-aluminium alloys, improving homogeneity [133]. This leads to a seemingly limited process window in which the part's quality can only be partially optimized. It is also hard to decide on the optimal combination of keyhole porosity percentage and the amount of unmelted niobium in the L-PBF parts. Such a dilemma

between the need for unmelted particles reduction and keyhole porosity reduction remains a challenge, leading to a porosity-segregation dilemma that needs to be addressed.

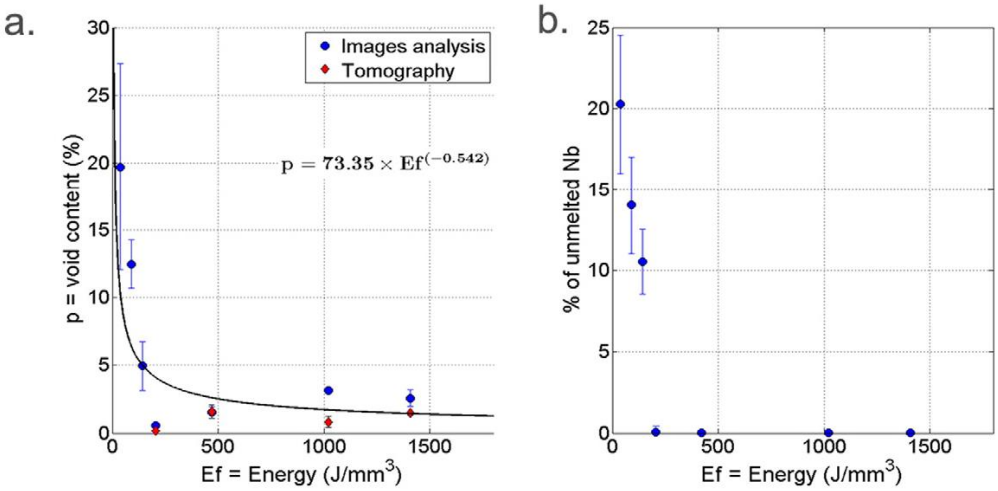

Figure 43 Typical defects of in-situ alloyed Ti-Nb binary alloy with increasing energy density a) porosity b) unmelted Nb [105].

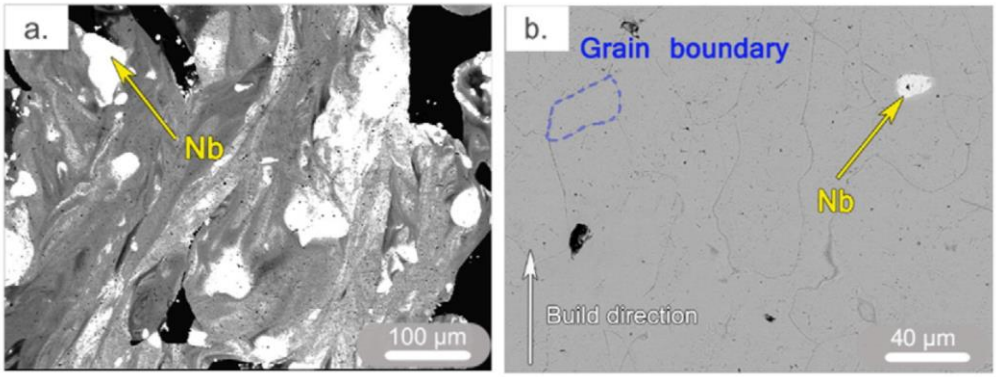

Figure 44 SEM of Ti-40.5Nb at different energy density a) 39 J/mm^3 b) 214 J/mm^3 [105].

Similarly, the *in-situ* alloyed Ti7.5Mo (wt%) system studied by Kang *et. al*. shows a similar influence of ε on the number of unmelted molybdenum particles and porosity [188]. The ε increment improved part's densification to a maximum of 99.7 % while minimizes the amount of unmelted molybdenum particles. However, the porosity type shown in the optimized part contains keyhole porosity, indicating that further reduction of unmelted molybdenum particles with increased ε will only lead to more keyhole porosity formation. This observation reinforces the need

to address the porosity-segregation dilemma. A study on *in-situ* alloyed Ti50Ta (wt%) by Sing *et. al*. also points towards a similar trend of density and unmelted tantalum particles with increased ε [94]. The optimized parts in the study contain unmelted particles which signify the possibility for improvement. It is difficult to eliminate the compositional segregation caused by unmelted tantalum particles while obtaining parts with no porosity. The issue of unmelted particles and compositional segregation is commonly seen in the *in-situ* alloying technique. This issue, however, is especially prominent when it comes to the *in-situ* alloying of biocompatible β-titanium. The main reason behind such occurrence is that biocompatible β-Ti stabilizers are mostly composed of refractory elements, in which the β-titanium stabilizers' melting point is very different from that of titanium. The properties of titanium and different β-titanium stabilizers are listed in Table 1.

Table 1 Melting point, boiling point, density, and the lower limit of Mo_{eq} β -Stabilization wt% associated with biocompatible elements commonly utilized in the in-situ alloying process via L-PBF.

Element	Melting Point (°C)	Boiling Point (°C)	Density (g/cm^3)	Mo_{eq} Based Critical β -Stabilization Lower Limit (wt%)
Ti	1668	3287	4.51	N/A
Mo	2623	4639	10.3	11.8
Nb	2468	4927	8.57	42.1
Ta	3017	5458	16.4	53.6

For reference, the molybdenum equivalent, Mo_{eq} (wt%) within the alloys can be calculated using [189]:

$$Mo_{eq} = 1.0\,Mo + 0.67\,V + 0.44\,W + 0.28\,Nb + 0.22\,Ta + 2.9\,Fe + 1.6\,Cr + 0.77\,Cu + 1.11\,Ni + 1.43\,Co + 1.54\,Mn + 0\,Sn + 0\,Zr - 1.0\,Al \quad (7)$$

The critical lower limit of Mo_{eq} for β stabilization is 6.25 at % or 11.8 wt %.

The mechanical properties of the multi-metal interfaces mostly depend on three factors, namely (1) the type of constituent phase/s, (2) the thickness of the detrimental phases, and (3) the morphology of the interfacial phases. Brittle intermetallic compounds normally act as crack initiation sites and impair the ductility of materials [190].

The diffusion of elements within the interface can result in intermetallic formation, as shown in a study using AlSi10Mg/C18400 copper alloy [141]. Al_2Cu intermetallic compounds are formed which are found to be detrimental to the mechanical properties of multi-metal structures. Interfaces with thick detrimental intermetallic layers normally fail in a brittle manner. Generally, iron-titanium intermetallic compounds have been proven to be the most detrimental to bond properties regardless of the type of joining techniques used. This is due to the formation of cracks at the interfaces as a result of the intermetallic compounds [191-193]. To improve the mechanical properties of the iron-titanium interface, copper [194, 195], nickel [196, 197], and silver-based [198, 199] interlayers have been incorporated to suppress the formation of iron-titanium intermetallic compounds between the titanium and steel alloys. However, copper-titanium and nickel-titanium intermetallic compounds are still found to be detrimental at the interface as they normally result in brittle failure across the interface. In contrast, AgTi is the only intermetallic that did not have a detrimental effect on the bond strength as the fracture of Ti/AgTi/Ag/SS interface happened within the ductile silver interlayer [198, 199]. In addition, the hardness of the silver-titanium intermetallic (164 HV) [198] is also much lower compared to that of the copper-titanium

(530 to 670 HV) [191], nickel-titanium (~662 HV) [197, 200], and iron- intermetallic compounds (> 1000 HV) [201]. Other frequently found detrimental phases includes σ-FeCrV phase (forms when stainless steel is excessively enriched with vanadium and/or chromium content) [202, 203], TiC (forms when titanium is bonded directly to steels with more than ~0.16w% carbon), and $\lambda(Cr,Fe)_2Ti$ [204, 205]. The diffusion of elements within the interface can result in intermetallic formation, as shown in a study using AlSi10Mg/C18400 copper alloy [141]. Al_2Cu intermetallic compounds are formed which are found to be detrimental to the mechanical properties of multi-metal structures. Interfaces with thick detrimental intermetallic layers normally fail in a brittle manner. Generally, iron-titanium intermetallic compounds have been proven to be the most detrimental to bond properties regardless of the type of joining techniques used. This is due to the formation of cracks at the interfaces as a result of the intermetallic compounds [191-193]. To improve the mechanical properties of the iron-titanium interface, copper [194, 195], nickel [196, 197], and silver-based [198, 199] interlayers have been incorporated to suppress the formation of iron-titanium intermetallic compounds between the titanium and steel alloys. However, copper-titanium and nickel-titanium intermetallic compounds are still found to be detrimental at the interface as they normally result in brittle failure across the interface. In contrast, AgTi is the only intermetallic that did not have a detrimental effect on the bond strength as the fracture of Ti/AgTi/Ag/SS interface happened within the ductile silver interlayer [198, 199]. In addition, the hardness of the silver-titanium intermetallic (164 HV) [198] is also much lower compared to that of the copper-titanium (530 to 670 HV) [191], nickel-titanium (~662 HV) [197, 200], and iron-intermetallic compounds (> 1000 HV) [201]. Other frequently found detrimental phases includes σ-FeCrV phase (forms when stainless steel is excessively enriched with vanadium and/or

chromium content) [202, 203], TiC (forms when titanium is bonded directly to steels with more than ~0.16 wt% carbon), and $\lambda(Cr,Fe)_2Ti$ [204, 205].

For the joining of Inconel 718 and 316L stainless steel using electron beam powder bed fusion (EB-PBF), Hinojos *et al.* have found that the amount of precipitate formed during the process is much lesser compared to conventional joining method [145]. However, a high amount of carbide and precipitate formation in regions like the fusion zone can reduce the corrosion resistance and cause embrittlement. In a separate study, Demir *et al.* explained that the formation of cracks at the multi-metal interface between Fe/Al12Si is due to the high fragility of the iron-aluminium intermetallic [144].

Apart from the inherent properties of the interfacial phases, the quantity of those phases also has a severe effect on the bond properties. The structural properties of multi-metal parts weaken when an excessive amount of detrimental phase is formed due to the disproportionate mixing of interlayers and base alloys. Therefore, the tensile strength of the diffusion bonded interfaces decreases with an increase in intermetallic thickness [194, 197]. In other words, the titanium/steel interface which contains iron-titanium intermetallic compounds can exhibit a high bond strength if the quantity of intermetallic compounds is greatly reduced. As such, the friction welded, and explosion welded titanium/steel interfaces are typically stronger compared to other joining techniques and failure typically happens at the base alloy instead of the interface [203, 206-209]. The formation of intermetallic compounds can be controlled by restricting the dilution between the materials and decreasing their interaction time. The interaction time can be reduced by lowering laser power, increasing scanning speed, or hatch spacing which controls the melt pool dimensions during L-PBF.

6. Potential Research for *In-Situ* Alloying and Multi-Metal Processing by Laser Powder Bed Fusion

6.1 Novel Fabrication Strategies

Microstructure developed during L-PBF tends to be strongly textured due to the directional heat flux and large thermal gradients [210]. While processing parameters that affect the energy input are proven to affect microstructure textures [211], manipulations by scanning strategies are supposed to be easier. To achieve a full density with controllable microstructures, multiple scanning strategies have been developed [212]. Three main basic strategies, namely unidirectional, bidirectional, chessboard, or island strategies, are well developed for L-PBF (Figure 45**Error! Reference source not found.**a, b, and d). There are some variants derived from these three basic strategies with rotation for a certain angle (e.g. 60 ^{o} [213], 67 ^{o} [214], or 90 ^{o} [215]) or shift for a certain distance between the layers [216]. However, the research done by Robinson *et al.* concluded that hatch rotation has little effect on the density, residual stresses, top surface roughness, and strength of L-PBF parts [174]. Unidirectional scanning is the simplest strategy and generally leads to the least densification and strongest texture while other variants show superior densification behavior [217]. The improvement on densification of other strategies depends more on materials and other processing parameters. For instance, an insignificant change was reported in work done by Thijs *et al.* [216]. In their study, five strategies (unidirectional scanning, bidirectional scanning, re-scanning based on bidirectional scanning with 90 ^{o} rotation of the scanning direction, island scanning, shifting the position of the scan vectors between the layers based on island) are used in AlSi10Mg, with a relative density of 99.0 %, 98.9 %, 99.4 %, 98.2 % and 98.7 % obtained, respectively. As full density has been achieved in unidirectional scanning strategy, an insignificant improvement was witnessed. However, the effect on microstructure texture is obvious. The texture index (TI, defined by

$$\mathrm{TI} = \int_{eulerspace} \left(f(g)\right)^2 dg, \tag{8}$$

where f is the orientation distribution function as a function of the Euler space coordinates g. For isotropic materials, TI is equal to unity) for these strategies was revealed to be 1.974, 1.982, 1.266, 1.127 and 1.079, respectively, which is consistent with the fact that rotation of scanning direction always eases texture by changing the heat flux.

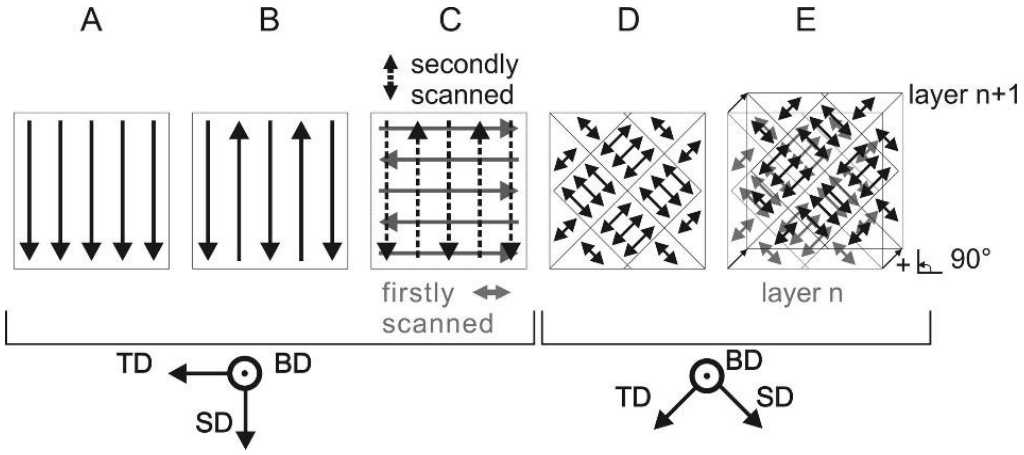

Figure 45 Overview of the scanning strategy used for the different samples. The building (BD), scanning (SD), and transverse direction (TD) are indicated. Sample A is scanned with long unidirectional vectors; sample B with long bidirectional vectors; sample C is first scanned with long bidirectional vectors in TD and secondly scanned with long bidirectional vectors in SD; sample D is scanned with island strategy with 90° rotation but without shift and sample E is scanned with island strategy with 90° rotation and 1 mm shift between the layers [216].

Layer thickness is one of the key parameters in multi-metal fabrication as it affects the penetration depth of the melt pools. A larger layer thickness will lead to thicker penetration depth and hence the formation of a greater amount of intermetallic compounds which results in lower mechanical strength of the multi-metal parts. As such, layer thickness should be kept to a minimum to avoid the formation of detrimental phases. A discussion on intermetallic compounds formation is included in later sections.

However, the layer and powder thicknesses can differ substantially for the first few build layers when the process has not reached the steady-state thicknesses. Figure 46 and Figure 47 depicts how the powder thickness varies across the initial build layers. In the beginning, the powder will

have a powder thickness of t_{p1} which is the physical gap width between the substrate and the lower tip of the recoater blade. After the loose powder in the first layer is melted, it consolidates into a dense layer with a thickness of t_{m1}. Thereafter, the build platform is dropped by a fixed displacement, *z*, and the powder is then deposited over the newly formed layer. If the thickness of the consolidated layer (t_{m1}) is smaller than the layer-wise displacement (*z*), then the thickness of the unconsolidated powder (t_{p2}, t_{p2} … t_{pm}) and layer thickness (t_{m2}, t_{m3} … t_{mn}) in the subsequent layers will increase towards steady-state values. The powder thickness and layer thickness for each build layers can be obtained using the following formula [218]:

$$t_{pn} = t_{p1} + (z - c \times t_{p1}) \sum_{i=0}^{n-2} (1 - c)^i \tag{9}$$

$$t_{mn} = c \times t_{pn} \tag{10}$$

Where *c* is the consolidation ratio defined in Equation (7). Given that the initial powder thickness (t_{p1}) and platform displacement (*z*) are known, experimental measurements of the layer thickness (t_{mn}) is required to obtain the consolidation ratio, *c*, through Equations (6) and (7). Similarly, the consolidation ratio can also be written as the product of the powder packing density (*p*) and a material loss coefficient (*l*).

$$c = {}^{t_{mn}}/_{t_{pn}} = p.(1 - l) \tag{11}$$

The consolidation ratio, *c*, is equal to the packing density, *p* under ideal conditions where there is no material loss. The powder particles can be ejected from the powder bed during the laser scanning process due to the spattering phenomenon. The spattering event can be attributed to the 1) induced argon gas flow towards the melt pool and 2) the intense metal vapor jet above the melt pool [219-222]. The induced argon flow carried the powder particles towards the melt pool while

the intense metal vapor jet imparts an upward momentum to eject the particles away from the melt pool. Considering the typical ranges for the powder density (0.4-0.6) and the consolidation ratio (~0.3) [218], the powder lost due to spattering can be calculated to be 0.25-0.5.

Figure 47 illustrates the variations of layer thickness and powder thickness using the equation above for an initial powder thickness (50 um), constant platform displacement of 50 um, and a consolidation ratio of 0.34. It can be observed that both powder and layer thicknesses rise gradually and reach approximately 90 % of its steady-state value within 6 build layers. For the first print layer, a low layer thickness and low laser energy input may be used to minimize the melt pool penetration and limit the dilution between dissimilar materials. With a few layers of dissimilar materials across the build, the composition of the top layer shifts towards that of the deposited material, and dilution control is no longer essential. Thereafter, the deposition rates can be increased by increasing the layer thickness and penetration depth.

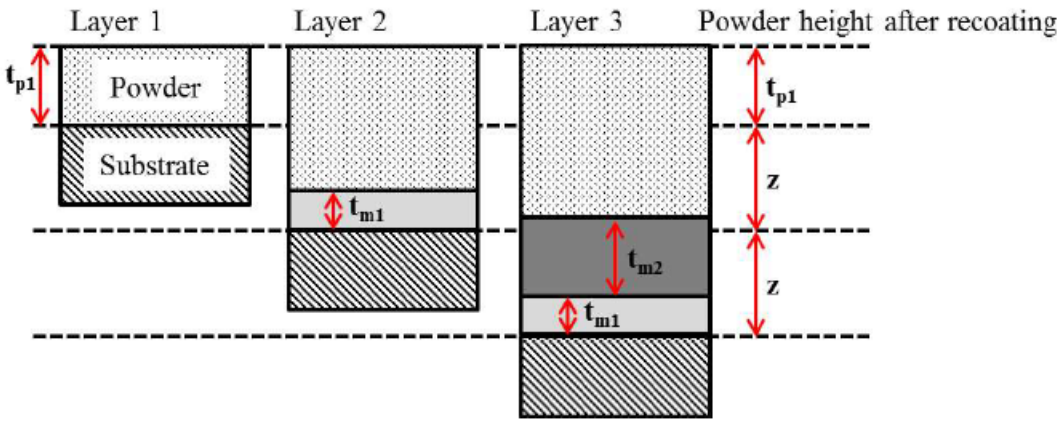

Figure 46 Illustration of layer thickness variation

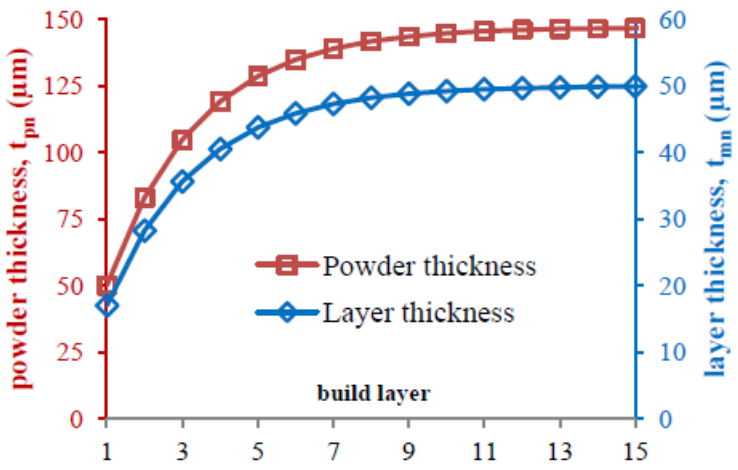

Figure 47 Powder and layer thickness variation across the initial build layers

Materials re-melting strategies, which refers to layer scanning twice or more before depositing a new powder layer, had shown their potentials in reducing porosity and surface roughness since they eliminate surface contaminants, removes oxide films, and produces a clean solid-liquid interface at the atomic level, especially when other parameters cannot achieve full density. In order to reduce residual stress and cracks, Li *et al.* proposed that re-melting should be carried out at a low laser energy density [223]. Smaller melt pools are formed because lesser laser energy is absorbed by the solidified bulk compared to powder materials even with the same scanning parameters, producing finer dendrites due to higher cooling rates. Nevertheless, investigation of re-melting on the un-melted previous layer and layers below is rare due to the complex thermal history. Yasa *et al.* studied multiple re-melting parameters and concluded that their effects on densification depend on careful parameter optimization. They reported that re-melting could remedy the porosity defects during the SLM process [224]. Similar conclusions are drawn in a study conducted by Yu *et al.* [225]. Besides, they also found re-melting decreases the surface roughness of L-PBF parts. Re-melting can also be applied only to the last layer or the outer skin of the part if the aim is to reduce the roughness or to enhance the surface properties. Re-melting

was done at every layer to improve the overall part's homogeneity for *in-situ* alloying of Ti6Al4V+1Cu (at%). As the ε required for Ti6Al4V and copper are similar, there is no unmelted copper found. Only copper enriched areas of up to 35 wt% can be observed due to incomplete diffusion of molten copper. Due to the density difference, the copper enriched area is often found at the bottom of the melt pools [82]. While research on scanning strategies has been carried out using single material systems, it is of interest to see the effect of different scanning strategies on the bonding and interface for multi-material processing due to the difference in melt pools and other physical phenomena resulted from these. It has been demonstrated that remelting strategies could not improve the bonding strength between CuSn and 18Ni300 as the interface became brittle, however, this requires further research for other material systems [150].

There is a need to come up with creative unconventional strategies to deal with the issue of compositional segregation without compromising the part's density to propel the *in-situ* alloying technique via L-PBF. To resolve this issue, a preliminary study by Huang *et. al.* demonstrated the effectiveness of laser re-melting strategy to address the porosity-segregation dilemma of *in-situ* alloyed binary alloys with elements of drastically different melting points [110]. The essence behind the laser re-melting strategy is to have multiple laser passes on the same layer, effectively giving more opportunity for the dissolution of refractory alloying elements without resorting to excessive ε that leads to keyhole porosity. Ti42Nb (wt%) parts were built in the study and it was found that laser re-melting strategy could enhance the part's homogeneity while maintaining the amount of keyhole porosity. The laser re-melting strategy was also studied by Brodie *et. al*. on *in-situ* alloyed Ti25Ta (wt%) [108]. It was shown that the effectiveness of the re-melting strategy to approach the porosity-segregation dilemma is highly dependent on the laser parameters choice. When the single scan parameters are optimized, pore-free parts can be achieved with a large

amount of area percentage unmelted tantalum (~0.75%). Utilization of laser re-melting further reduces the area percentage unmelted tantalum to ~0.25% without inducing additional porosity. Besides having a higher melting point, tantalum possesses higher thermal conductivity as compared to titanium. Tantalum particles essentially cool faster and have limited time for diffusion, in which the re-melting strategy provides a second chance for dissolution. Further investigation was also done by Brodie *et.al* on the Ti25Ta (wt%) manufactured via LPBF using conventional strategy and laser re-melting strategy to understand their low cycle fatigue behaviour [226]. It was found that the keyhole induced porosity is the dominant fatigue crack initiation site. No evidence has been found on unmelted tantalum particles to initiate fatigue crack, hence prompting for further investigation on the effect of localized inhomogenity. In some cases, the laser re-melting strategy can lead to more keyhole porosity at lower scanning speed (or when the ε is relatively high). For the fabrication of Ti37Nb6Sn (wt%) alloy via *in-situ* alloying, the increased ε leads to improved homogeneity but induces higher porosity due to more tin evaporation [120]. Moreover, it was found that the narrow melt pool produced by L-PBF only encircles a few powders and can contribute to macro-segregation due to localized inhomogeneity of the powder mixture [123]. However, *in-situ* alloying of Al-xCu leaves unmelted copper particles which can deteriorate tensile properties by acting as crack nucleation sites. To mitigate this problem, Martinez *et al.* proceeded with the preheating of the powder bed [74]. A density of more than 99.1% can be achieved for *in-situ* alloyed Al-xCu manufactured from both preheated and non-preheated powder bed. However, the preheated powder bed resulted in samples that are more chemically homogenous.

Compositional segregation is a common issue when *in-situ* alloying technique is used. One innovative approach by Zafari & Xia is to leverage such an inherent issue of *in-situ* alloying to achieve hybrid titanium alloy (HYTA) with enhanced mechanical properties [227]. As opposed to

having a homogenous material, Ti6Al4V (wt%) and Ti5Al5V5M3Cr (wt%) powder of equal mass were mixed and *in-situ* alloyed to intentionally achieve full dense parts with blocks of material portion retaining the composition of its raw materials. The approach leads to the retention of α' (Ti6Al4V) and β (Ti5Al5V5Mo3Cr) phases where each phase undergoes a series of work hardening mechanisms progressively that eventually improves the ultimate tensile strength to more than 1200 MPa and elongation to failure to more than 15%. The strain mismatch or stress concentration at α'/β interface is relieved by the activation of twinning at the interface as well as the smooth transfer of deformation from β to α' phase, hence achieving simultaneous strengthening and improvement in ductility. Additional study on HYTA has been done using equal mass of titanium (wt%), Ti6Al4V (wt%), and Ti5Al5V5Mo3Cr (wt%) powder [228]. The ternary HYTA has microstructure which is much more complex but with each phase having subtle differences in strength, eventually eliminating double yielding phenomena in binary HYTA to achieve a high yield strength of ~1000 MPa (UTS ~1100 MPa). The formation of highly heterogeneous microstructure leads to a large variety of deformation mechanisms such as slip, twinning, strain induced martensitic transformation and grain rotation activated. Accompanied by smooth transfer of deformation between phases, enhanced ductility of ~20% elongation to failure was achieved. Further heat treatment on HYTA can achieve tailored strength and ductility as needed, making the HYTA system a promising material to be used.Despite the tendency for incomplete melting of constituents during in-situ alloying, the parts produced using this approach have been shown to have comparable performance to parts formed using conventional pre-alloyed powders. Zhao *et al.* fabricated Cu15Ni8Sn samples using pre-alloyed powder and powder mixtures of Cu-Sn and Ni. Both types of powder were able to produce samples with high density of more than 99 % with similar microstructure and phases [229]. Chen *et al*. also found that the samples produced by in-

situ alloying possesses higher hardness and ultimate tensile strength compared to similar materials fabricated using pre-alloyed powder [230].

Vertical, inclined, and horizontal building orientations (Figure 48**Error! Reference source not found.**) are popular for parts with high length-to-height ratios for L-PBF. Rashid *et al.* coined a novel term, energy per layer (E_l), to predict the relative density while trying to quantify the relationship between relative density and build orientation [231]. E_l is given by:

$$E_l = E \times d \times A_p \tag{12}$$

where E_l is laser energy density supplied, d is powder layer thickness and A_p is printing area per layer. It was found that energy per layer in the range of 504 to 895 J yielded ≥ 99.8 % relatively dense Al12Si L-PBF samples. The anisotropy caused by building orientation is also investigated. For example, the fatigue resistance is higher in the horizontal direction than in the inclined and vertical direction [232]. Tolosa *et al.* compared mechanical tests of 316L stainless steel in all the possible build orientations in L-PBF and not only in three main directions [233]. For different materials, the detailed comparison between different build orientations needs further investigation. However, due to the nature of L-PBF, most of the multi-metal parts produced have variation along the vertical direction, which restricts the build orientation choices.

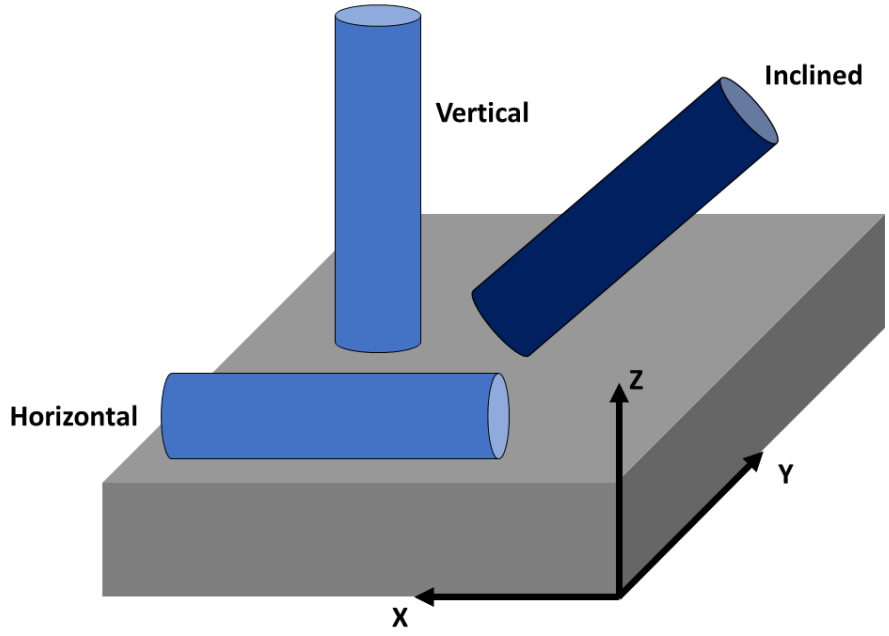

Figure 48 Schematic representation of three different orientations used.

6.2 Preventing Intermetallic Compounds Formation

A series of compatible interlayers can be introduced to the multi-metal interface to eliminate all the brittle phases. The binary phase diagrams of all the connected pairs of elements in Figure 49 Binary combinations of elements with no intermetallic compounds are free of brittle phases. In other words, a ductile fracture within the interface or weaker base alloy can be achieved using suitable choices of interlayers [205, 234]. Theoretically, there is no restriction on the numbers of interlayers and the composition of each interlayer. In other words, alloys may also be used as interlayers. However, it would be impractical to use too many interlayers for joining multi-metal structures as many alloys' compositions will have to be prepared. As such, the directed energy deposition process is among the most efficient way to achieve a wide range of compositions across the multi-metal interfaces as it allows mixing and deposition of distinct powders at arbitrary compositions [192, 202, 235].

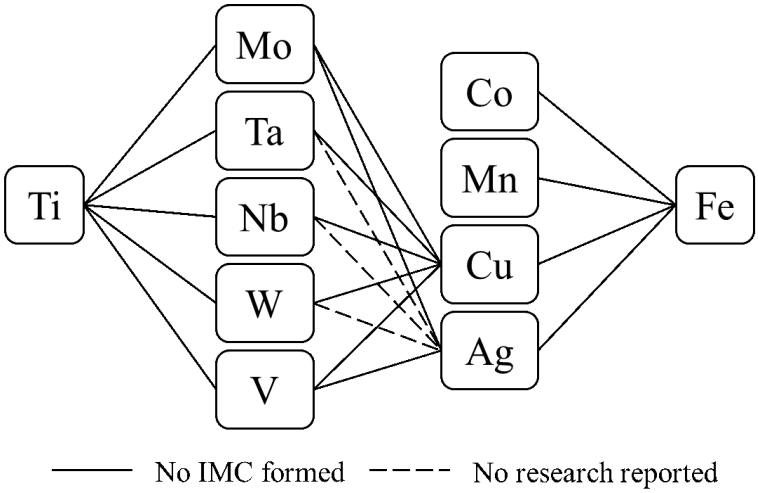

Figure 49 Binary combinations of elements with no intermetallic compounds [236]

Nonetheless, Tey *et al.* have attempted to prevent the intermetallic formation during multi-metal processing using L-PBF by introducing a copper alloy interlayer between Ti6Al4V and 316L stainless steel [237]. However, it was found that the titanium/copper interface contained three detrimental phases which limited the strength of the multi-metal part. Despite this, this method of introducing an interlayer is envisioned to improve multi-metal bonding.

6.3 New Material Systems

As mentioned previously, the materials available for L-PBF is limited due to restrictions by the feedstock production methods as well as 3D printability of pre-existing materials. As such, huge research effort has been devoted to expanding the materials library. One of the emerging research areas is high entropy alloys (HEAs). HEAs have high mixing configurational entropies that stabilise solid solutions based on simple underlying face-centered cubic (FCC), body-centered cubic (BCC), or hexagonal close-packed (HCP) structures. Using the composition-based definition, an HEA is composed of five or more elements with a concentration between 50 to 35 atomic percentage (at%). Some of the commonly used constituent elements of HEAs include copper,

chromium, cobalt, iron, manganese, nickel, tantalum, titanium, molybdenum, niobium, vanadium, zirconium, tungsten, zinc, aluminium, silicon and boron.

HEAs exhibit superior mechanical properties at high temperatures and exceptional strength, ductility, and fracture toughness at cryogenic temperatures. Hence, their popularity in multiple industries that require extreme temperature applications. For L-PBF, many studies have been conducted on HEAs, including CoCrFeMnNi [238-241], FeCoCrNi [242-244], FeCoNiCrN [243], AlCoCrFeNi [245], FeMnCoCrSi [246]. Systematic and comprehensive reviews have been done on HEAs processed by L-PBF [247, 248]. HEAs exhibit superior mechanical properties at high temperatures and exceptional strength, ductility and fracture toughness at cryogenic temperatures. Hence, their popularity in multiple industries that require extreme temperature applications.

As an emerging materials group for L-PBF, most of the work conducted have used pre-alloyed powders as feedstocks. However, *in-situ* alloying provides the opportunities for rapid modification of test compositions for the HEAs and lower the cost for production. To test te feasibility of compositions using more a more cost effective method, Luo et al. used powder mixtures of AlCrCuFeNi pre-alloyed powder with Ni powder [249]. Chen et al. fabricated CoCrFeMnNi HEA samples using a mixture of CoCrFeNi pre-alloyed powder and Mn elemental powder and showed the feasibility of in-situ alloying to form HEAs [230]. Ewald *et al.* used *in-situ* alloying to carry out a study on the AlCCoFeMnNi alloy system [250]. The experimental approach is shown in Figure 50. The study showed the possibility of processing complex powder blends with different morphologies, sizes by L-PBF. The manufacturing of parts with complex geometry, such as lattice structures is also shown in the same study.

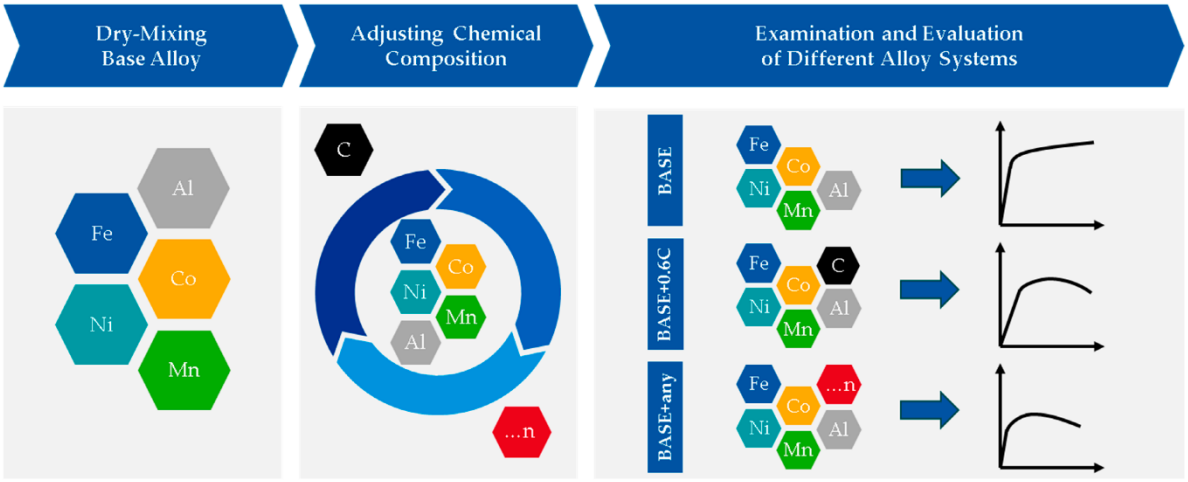

Figure 50 Schematic illustration of the rapid alloy development methodology using powder mixtures for the L-PBF, where "...n" is a placeholder for additional elements [250].

Unlike conventional joining techniques, AM features some unique capabilities which make it attractive for multi-metal processing. Firstly, with the appropriate dispensing mechanism, material compositions can be varied across the build layers by mixing different powders in various proportions. This allows the user to introduce any arbitrary number of interlayers between the base alloys. As such, it is possible to directly manipulate the composition, microstructure, and properties across the interface during the build process.

Secondly, by varying the material distribution within and across each build layer, multi-metal interfaces with a complex geometrical design and material variation in 3D can potentially be created (Figure 51 Illustration of interfaces with 1D, 2D, and 3D material variations.). This could allow interlocking mechanisms to be incorporated at the multi-metal interface for improved interfacial fracture toughness [251-253]. In comparison, friction welding and explosion welding are restricted to the bonding of near-planar and/or planar surfaces only. As a result, the distribution of material can only be varied in one-dimension (1D). Other joining techniques like laser welding, electron beam welding, diffusion bonding, brazing, transient liquid phase bonding, and friction stir welding have the capability to process non-planar surfaces featuring material variations in 2D.

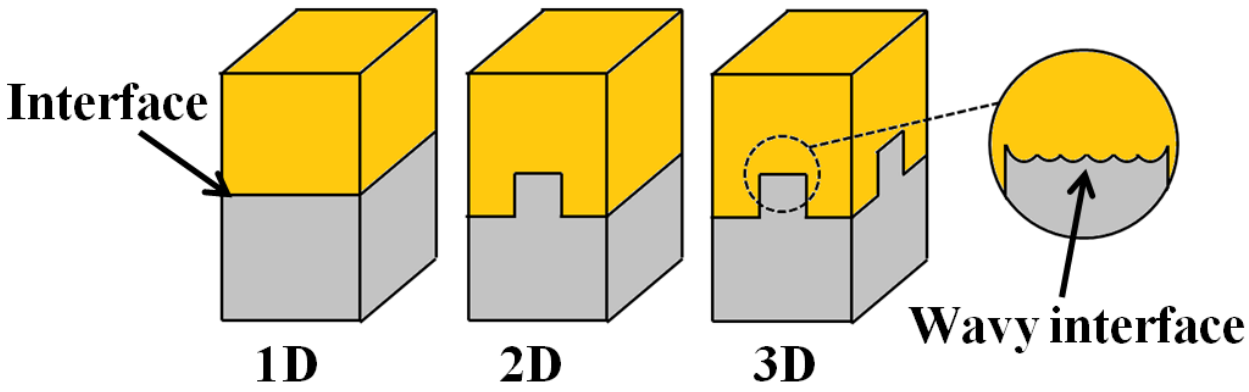

Figure 51 Illustration of interfaces with 1D, 2D, and 3D material variations.

Thirdly, the repeated stacking of melt pools within and across the build layers naturally induces microscale waviness (Figure 51 Illustration of interfaces with 1D, 2D, and 3D material variations.). This waviness could potentially increase the resistance to crack propagation and enhance fracture toughness [251-253]. In contrast, joining processes such as diffusion bonding, brazing, and transient liquid phase bonding produce joints with continuous and planar layers of intermetallic compounds which makes crack propagation relatively easy.

Lastly, the layer thickness and penetration depth of the melt pool in AM techniques can be varied to control the interfacial composition gradient (Figure 52). Low layer thickness and shallow penetration depth can be used to produce a narrow interface with limited dilution while a large layer thickness and penetration depth can be used to produce a thicker interface with a gradual transition in properties. By dynamically changing the penetration depth at selected layers, it is also possible to homogenize or create an arbitrary functional gradient across the interface (Figure 52). Such flexibility in altering the interface is not available to other joining techniques.

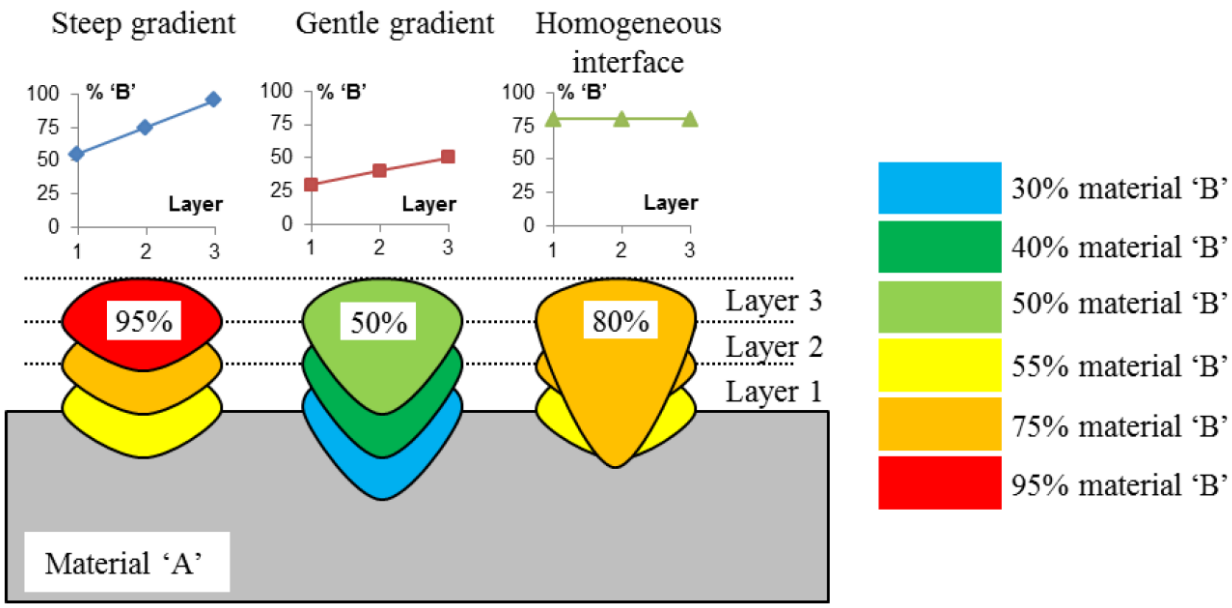

Figure 52 Effect of melt pool dimension on composition gradient.

Even though the above four capabilities are available to both the DED and L-PBF processes, each process excels differently in the respective areas. Specifically, DED excels in varying the material across and within each build layer while the L-PBF process requires an additional dispensing mechanism to realise such benefit [179, 254, 255]. However, the better resolution of the L-PBF process makes it superior in limiting interfacial dilution. Additionally, the L-PBF process also features higher cooling rates (10^6-10^7 K/s [37]) than DED due to its smaller laser spot diameter (~80 to 100 μm), lower layer thickness (20 to 100 μm), and higher laser scanning velocities (10^2 to 10^3 mm/s). Hence, the microstructure of the L-PBF interface is likely to be finer and may contain metastable phases which differ from a DED interface. Furthermore, the L-PBF may also produce a unique composite like interface due to imperfect mixing within the rapidly solidified melt pools [256]. The composite-like structure may contain regions belonging to the undiluted base alloy which could potentially act as a ductile reinforcement for the brittle interface. This, however, needs to be verified through further research.

Due to the lack of tensile test data for AM multi-metal parts, little is known about its capabilities and bond strength. In particular, the multi-metal processing potential of L-PBF has been largely overlooked thus far. Nevertheless, AM techniques possess a unique combination of characteristics that could make them compatible with multi-metal processing.

6.4 New Powder Deposition Methods

New powder deposition mechanisms for L-PBF are needed to achieve multi-metal processing and *in-situ* alloying. It is important for the active development of new deposition methods to achieve functionally graded materials (FGM) as well. For instances, Liu *et al.* introduced a partition to the powder recoating mechanism so that two different powder materials can be deposited at any build layer to produce multi-metal parts [14]. Wang *et al.* simply incorporated two hoppers into the build chamber (Figure 53). However, these methods only allow materials to be varied across the build layers but not within each layer. In order to achieve intra-layer material variation, a nozzle-based system has been incorporated into L-PBF so that different powders can be selectively deposited within each build layer [14, 141, 255].

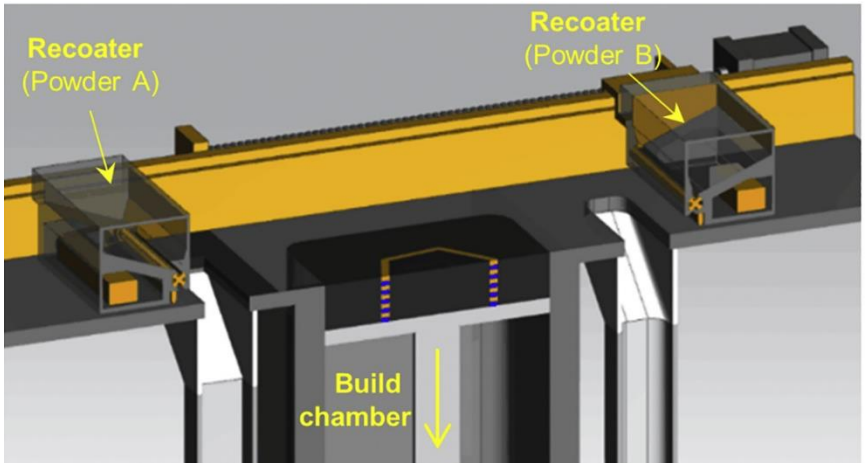

Figure 53 Schematic of multi-metal L-PBF with two hoppers in the build chamber [158]

Unlike typical L-PBF, a multiple powder delivery system was designed to enable multi-metal processing (Figure 54). This system includes two sets of powder feeders and two powder hoppers

that can load two metals at the sample time. The release of powder onto the powder bed can be controlled selectively by a switch.

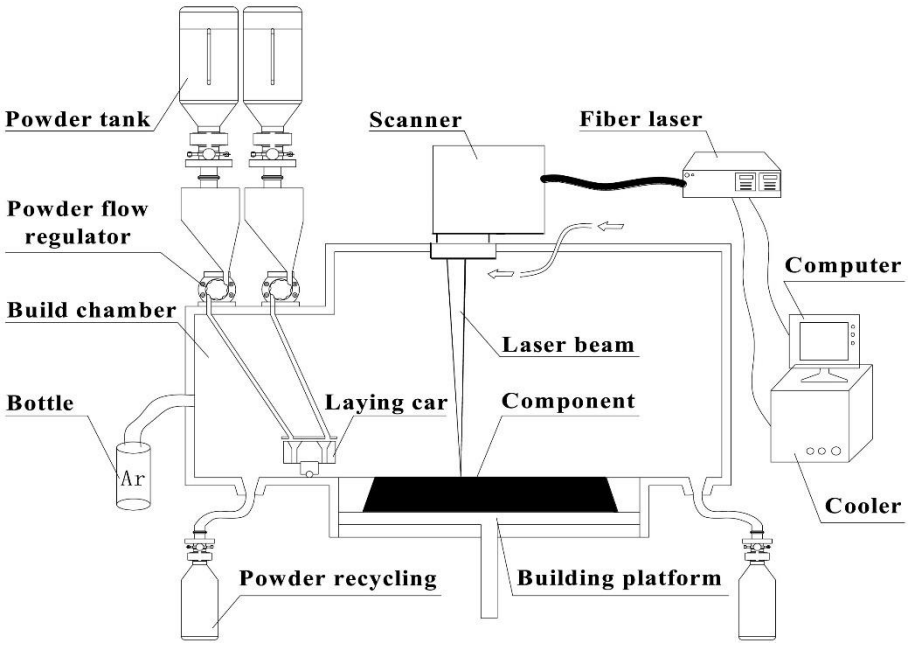

Figure 54 Schematic of the multi-material SLM machine [147].

Recognizing the needs from the industries to have both multi-metal processing capability in single layer and across the layers, a six channel ultrasonic powder delivery system is developed as shown in Figure 55 [257].

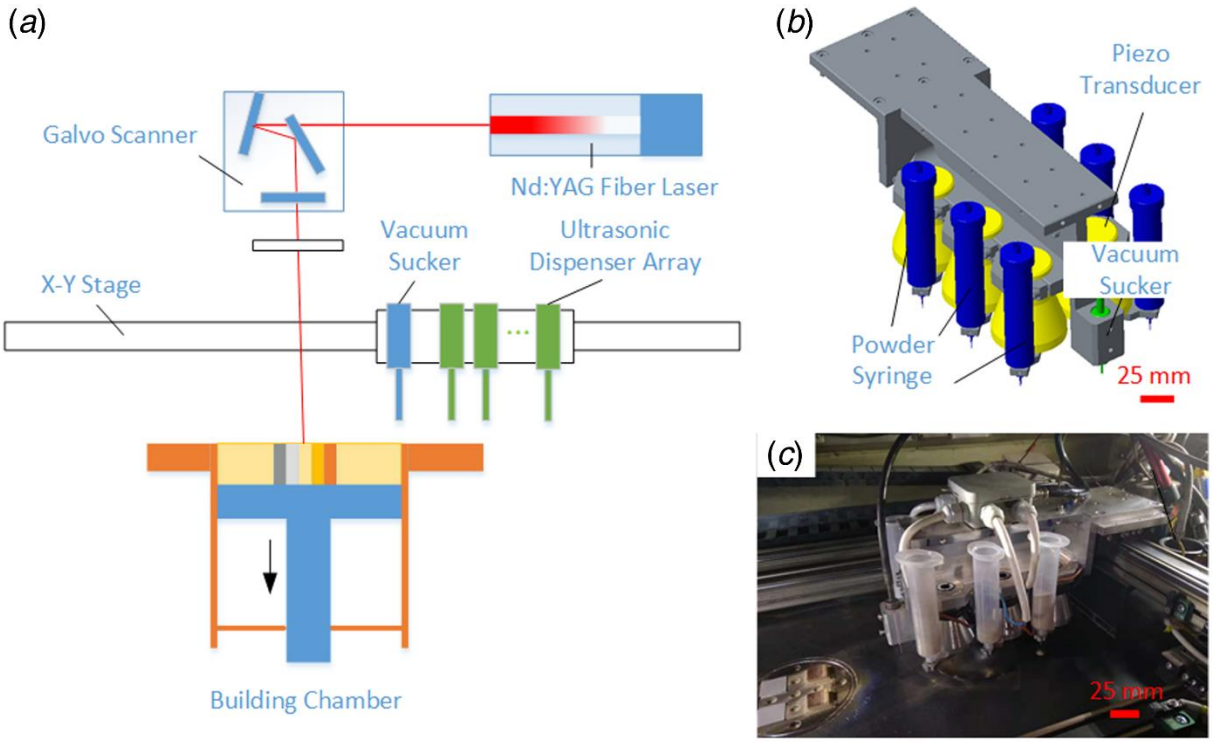

Figure 55 Schematic of the multi-material set up with six channel ultrasonic dispenser with (b) and (c) showing the 3D model and photograph of the ultrasonic powder dispenser array [257]

Another prototype for multi-material deposition is demonstrated for L-PBF [144], as shown in Figure 56. The method is used to fabricate specimens using pure iron and Al12Si, with components that consist of pure iron and Al12Si regions with a transition region of *in-situ* alloyed materials from these two constituents.

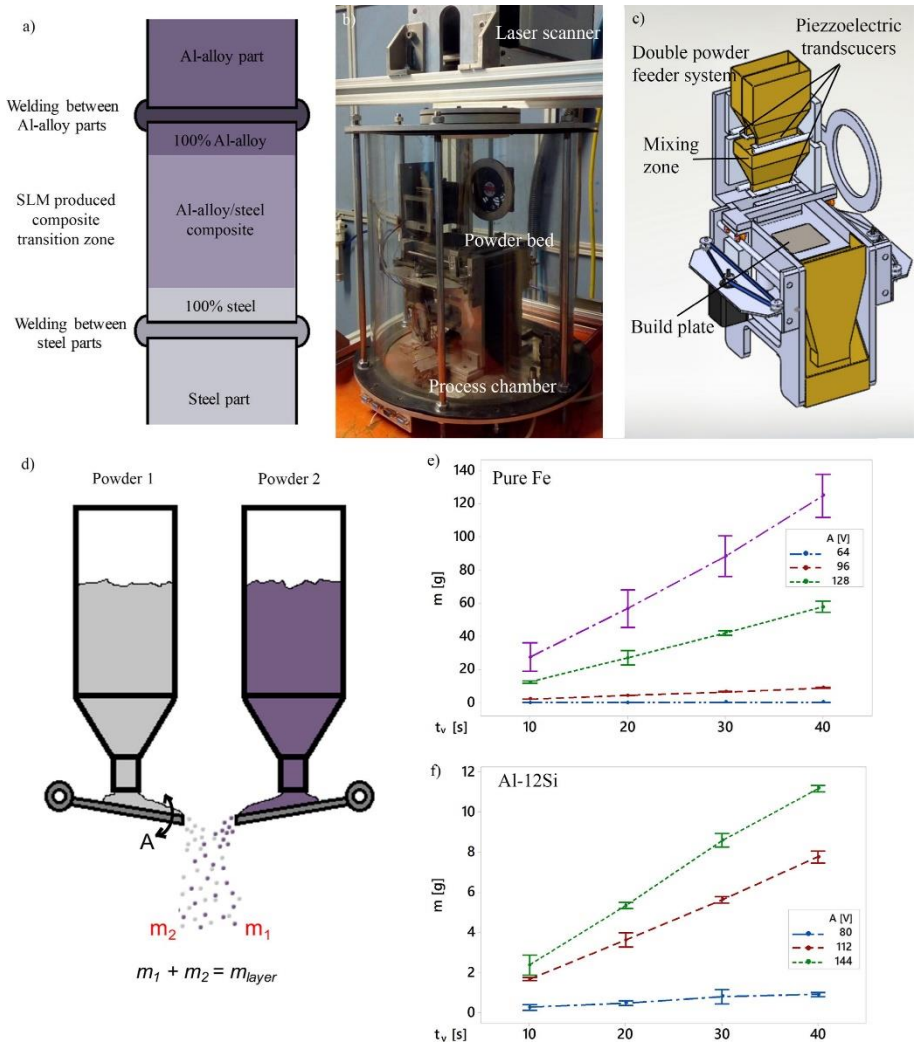

Figure 56 Concept of using multi-material transition zone for assembling Al-alloys with steel. (b) In-house built prototype L-PBF system with multi-material processing capability. (c) Design of the powder feeder system. (d) Working principle of the powder feeder for mixing powders. (e) Calibration curves of the delivered powder mass (*m*) of pure Fe and (f) Al12Si as a function of applied voltage (*A*) and vibration time (t_v). Error bars depict 95% confidence interval for the mean [144].

An innovative multi-material powder deposition system that utilizes vibration plate for powder metering was developed for EB-PBF [258], as shown in Figure 57. The utilization of a vibrating plate reduces the need for revolute pair, making it highly reliable in a dusty environment. The system was developed for the fabrication of Ti6Al4V/Ti47Al2Cr2Nb graded materials. Due to the similar process nature, the innovation can be adapted for L-PBF process with proper modification.

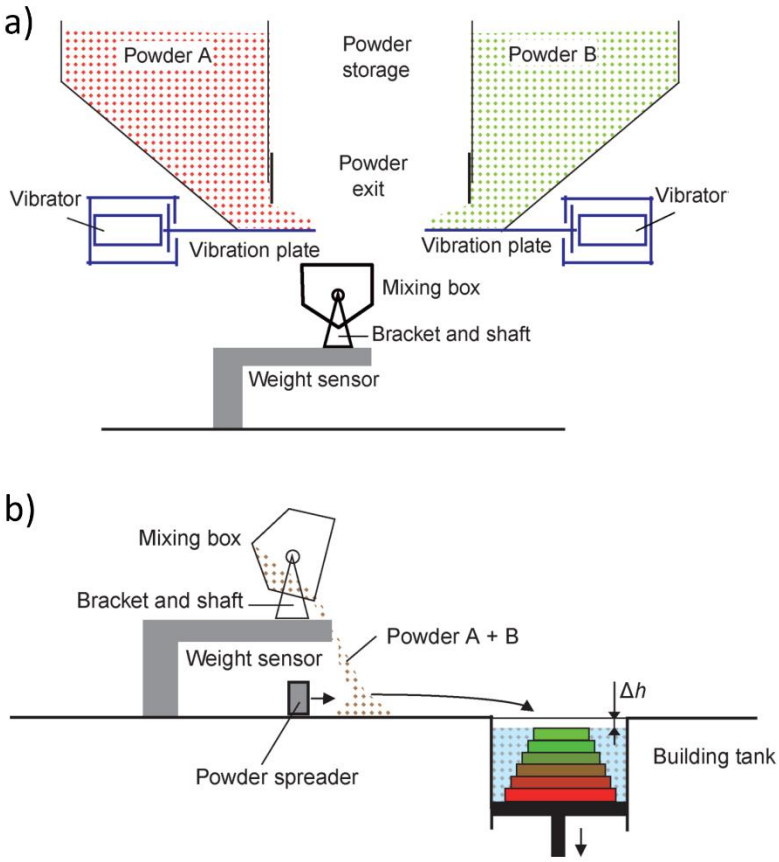

Figure 57 a) Powder supply with vibration plate into the mixing box. b) Application of mixed powder onto the powder bed [258]. a) Powder supply with vibration plate into the mixing box. b) Application of mixed powder onto the powder bed [258].

Zhang et al. developed an in-situ powder mixing system for L-PBF that allowed two different powders to be mixed and dispensed in a selected ratio (Figure 58). The core part of the system is the powder mixing and feeding system that has three sub-vibration systems to provide stable powder flows. Both types of powders can be mixed evenly by rotating the mixing box and then the mixture is released into the lower hopper for dispensing to the build platform [259]. This system also enables multi-metal processing as the mixing system can be deactivated while keeping the dispensing system operational which allows for the two materials to be deposited independently.

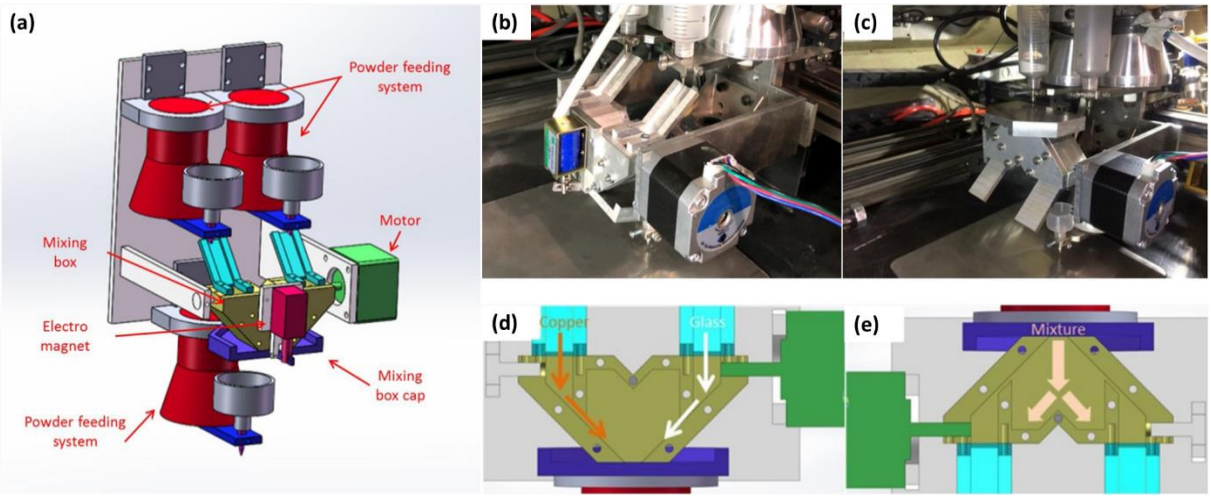

Figure 58 In-situ powder mixing system for L-PBF (a) detailed schematic of the system (b) delivering powders into a mixing box (c) mixing powders by motor controlled rotation of the box with (d) and (e) showing the mechanism of the mixing systems where powders were both vertically and horizontally merged and horizontally separated and vertically merged again respectively [259].

Recycling of materials from multi-metal processing is challenging as the unconsolidated powder cannot be easily recovered as they are interspersed within the common powder bed. To address this issue, Wei *et al.* incorporated a vacuum system to remove loose powder from selective regions in the powder bed which can help avoid cross-contamination of different powders when removing the materials [179, 257]. A similar concept is also proposed by Chivel [260]. Demir & Previtali suggested that AM industry can refer to electronics and pharmaceutical industries for powder recycling and separation methods. For example, magnetic powder separation method can be used and separation based on shape and density can also be employed [144]. Gravity separation techniques can also be derived from the mining industry to achieve separation by density difference [261]. Horn *et al.* investigated the possibility of using binary powder mixtures of different particle size distributions which can be sorted and recycled by screening after L-PBF. Firstly, they conditioned the powders in accordance with DIN 6615 to secure sortable powder size distributions that are sufficiently different from one another. After processing by L-PBF, the powders were sorted using two screening stages. It is found that the sorting process yields an

economic solution for powder recycling as the efficiency is only 10 % lower than typical recycling methods used for single material processing [262].

6.5 Simulations

Due to the complexity of the physical phenomena during L-PBF, simulations have been popular in trying to understand the process. Multiple research have been conducted using the discrete element method [263], thermo-fluid dynamics [264, 265], finite element method [266, 267], and phase-field model [268, 269]. Comprehensive reviews on simulations for L-PBF have been published [270-272]. Despite extensive work on simulations for L-PBF, limited information is available for multi-metal processing and *in-situ* alloying.

A multi-layer finite element model was proposed to investigate the thermal behaviour for TiB_2/Ti6Al4V multi-metal processing by L-PBF [142]. A schematic of the simulations is shown in Figure 59 Schematic overview of the SLM physical model (a) the established finite element model (b) and laser scanning strategy (c) during the SLM process (point 1 at the center of the Ti6Al4V layer; point 2 at the center of the TiB_2 layer) [142]..

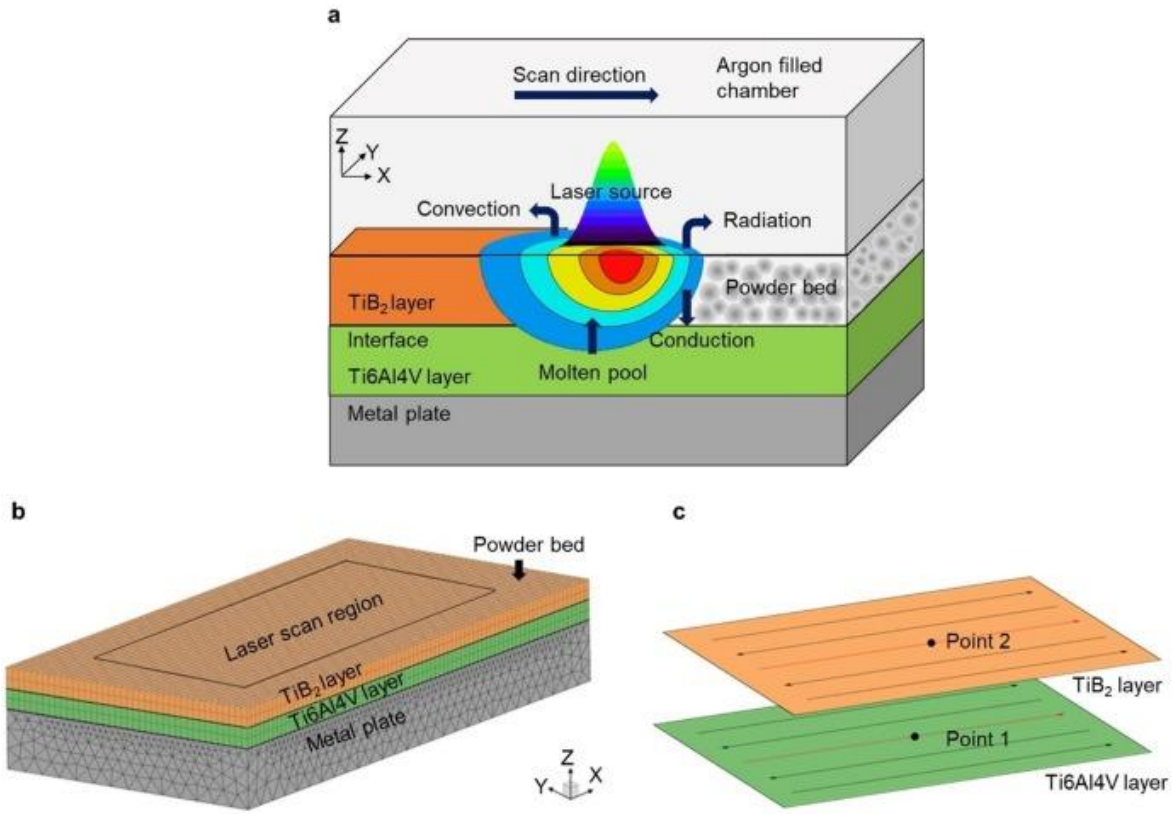

Figure 59 Schematic overview of the SLM physical model (a) the established finite element model (b) and laser scanning strategy (c) during the SLM process (point 1 at the center of the Ti6Al4V layer; point 2 at the center of the TiB_2 layer) [142].

In the model, the element birth and death method was applied to simulate the multi-layers during L-PBF. The simulation results showed that the maximum temperature gradient was located at the interface between TiB_2 and Ti6Al4V, and the interface temperature and melt pool lifetime are important for the wettability at the interface. In another study, molecular dynamics were used to simulate the L-PBF melting process between iron and aluminium for multi-metal processing [273]. It is observed that aluminium experienced a higher melting rate compared to iron and the two metals can fuse with each other after melting. Discrete element method was used to simulate the melt pools' evolvement and melt track morphology for multi-metal deposited in the same and across different layers (Figure 60) [274].

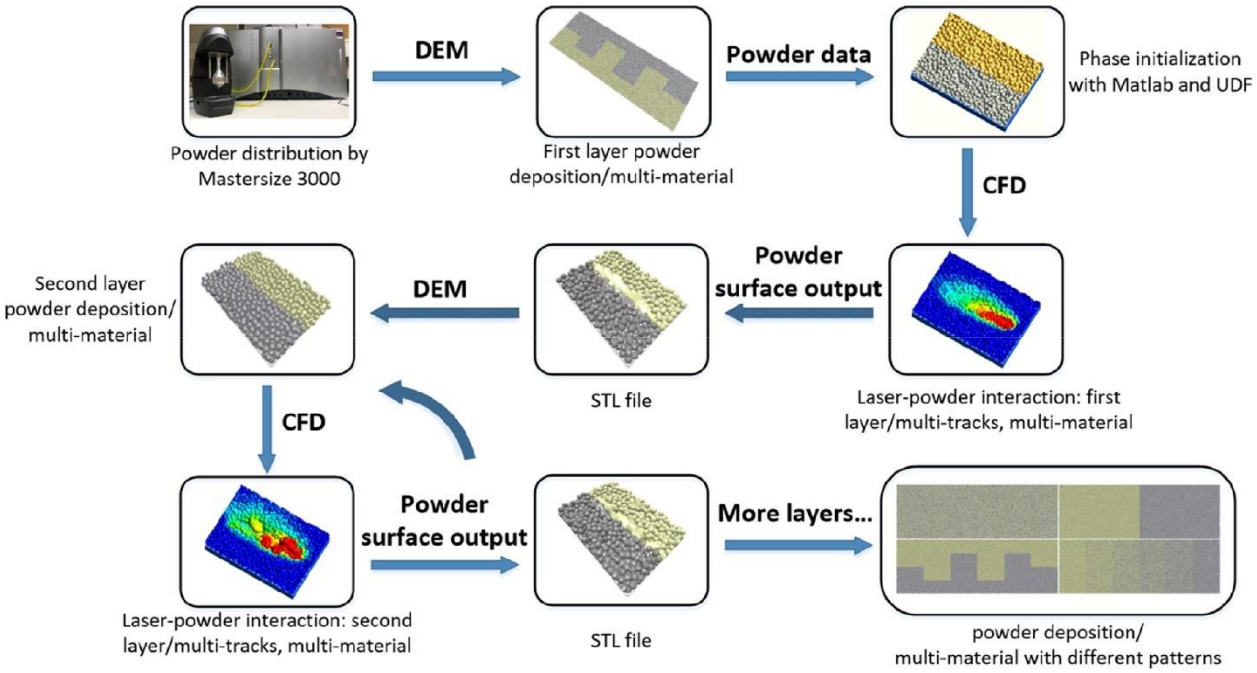

Figure 60 Framework for multi-track, multi-layer, and multi-metal L-PBF modelling [274]. Framework for multi-track, multi-layer and multi-metal L-PBF modelling [274].

The simulations can visualise the interface between 316L stainless steel and Cu10Sn. Due to their different thermal properties, melt pool development appear differently when the same energy density was applied and 316L stainless steel melted first which results in the melting of Cu10Sn by conduction and convection flow from the liquid 316L stainless steel. Phase migration at the interface was found to be related to the convection within the melt pools which contributed to the mixing and elemental diffusion (Figure 61). Meanwhile, multi-material simulation has been done based on the EB-PBF technology with a multi-scale simulation, in which, the melting of particles with different materials were considered [275]. Nevertheless, the homogenization process of *in-situ* alloying through particles mixing process based on Marangoni convection as well as particles dissolution process based on diffusion are not well studied.

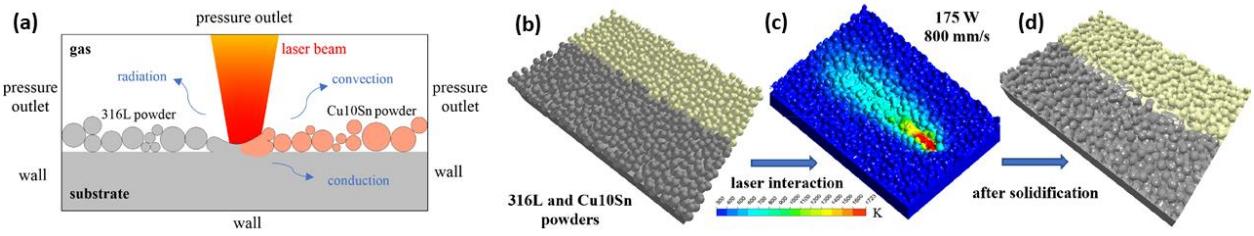

Figure 61 Simulations for multi-metal L-PBF (a) thermal boundary conditions of the calculation domain (b) 316L and Cu10Sn powders with clear boundary (c) laser beam applied on the boundary with 175 W and 800 mm/s (d) track morphology after solidification [274].

Sun *et al.* presented a mesoscopic model based on a volume of fluid (VOF) method. In their work, they simulated L-PBF with mixed and unmixed dissimilar powders which make their model applicable for both multi-metal processing and in-situ alloying. The initial powder beds for different scenarios are shown in Figure 62. For mixed powders, non-homogenous temperature distribution is observed due to the different thermal-physical properties of the two materials. The model also showed partially melted or unmelted particles embedded in a fully melted matrix which results in significant fluctuation of the track width. For the melting of unmixed powder beds, an asymmetrical melt pool is observed at the interface [276].

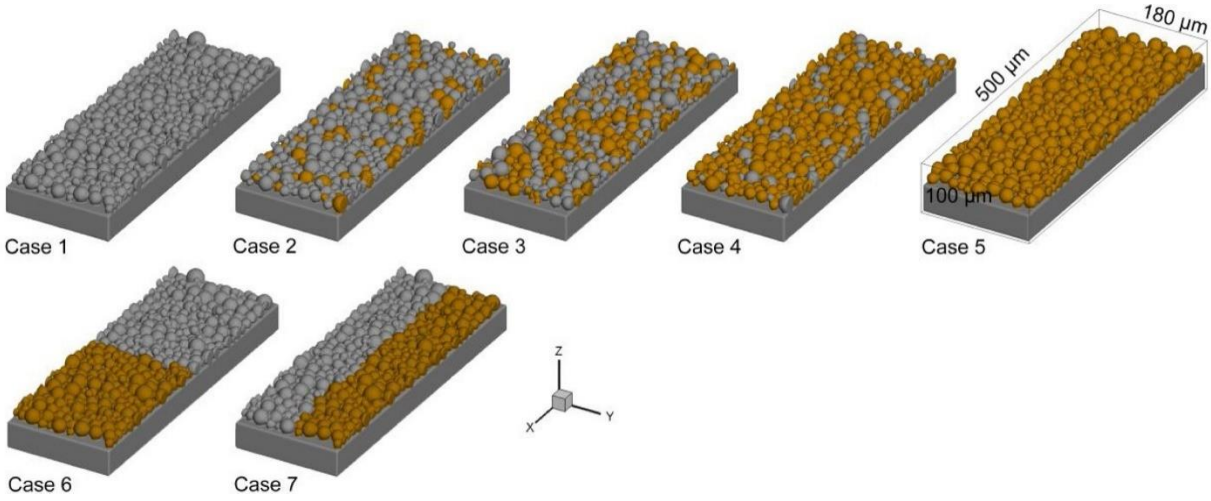

Figure 62 Initial powder beds for different sceneroir with Case 1 and 5 for single material, Case 2, 3 and 4 for in-situ alloying and Case 6 and 7 for multi-metal processing [276].

There has been limited available literature on simulations for *in-situ* alloying by L-PBF. However, numerous researches have been done on simulations for metal matrix composites using L-PBF [277-282]. Like *in-situ* alloying, powder mixtures are typically used in composites, and thus, several aspects of these simulations can be adapted in future research.

6.6 Machine Learning and Artificial Intelligence

While simulations allow a deeper understanding of L-PBF, there are still unresolved challenges such as process variability and lack of standards. Such variations result in difficulty in process planning which restricted widespread adoption of L-PBF in the industry. Machine learning and artificial intelligence can be used to enhance and complement simulations in achieving higher part quality [283]. Machine learning is often utilized to capture process behaviour using measurement data.

Typically for processing parameters optimisation, experiments are done to identify the process windows to avoid certain defects. This is time-consuming and cost-intensive, in addition to material and even equipment specific. Hence, optimised parameters usually cannot be generalised for L-PBF. Data-driven framework is used to detect layer-wise anomalies observed by thermal imaging for L-PBF [284] A spatial statistics model is then used with supervised and unsupervised machine learning techniques to detect defects within the layer.

Machine learning methods were applied to measured data to establish input and output relationships between the process parameters and surface texture. Predictive models using genetic programming and neural network modelling for process planning purposes are achieved for L-PBF of Inconel 625 [285]. Deep neural networks are used to interpret the image classification problem using melt pools in order to predict the defects due to L-PBF [286, 287]. Comprehensive reviews on machine learning for additive manufacturing are available [288, 289].

By combining simulations and machine learning, it is possible to predict or optimise process parameters to achieve desired part properties. Self-learning was also made possible [290, 291]. A conceptual framework on the combination of statistical analysis, mathematical modelling, and machine learning techniques has been proposed [292]. These will be useful for multi-metal processing and *in-situ* alloying for L-PBF as more variables such as materials selection, powder size distribution, and differences in material properties are involved which make L-PBF more complex.

7. Summary

An analysis of the available literature on the *in-situ* alloying and multi-metal processing by L-PBF has revealed their importance and explores the possibilities they offer in expanding L-PBF applications. L-PBF will be increasingly employed for fabricating high quality, low cost, repeatable, and reliable functional parts. With these new approaches, L-PBF enhances manufacturing and engagement in the industry. *In-situ* alloying allows the expansion of the materials library that is available for processing by L-PBF as it also allows rapid feasibility studies of different composition of alloys. It has also been highlighted that in-situ alloyed parts have comparable, if not superior, part properties compared to the same materials formed using pre-alloyed powder by L-PBF. With new materials with comparable performance, it should encourage higher adaptation rate in the industry. For multi-metal processing, it allows for functional parts that often require combination of different materials properties to be directly fabricated using L-PBF. As such, with multi-metal process capability, industry can then enhance their manufacturing capabilities with direct fabrication of wider range of products. This review brings deep insights into the fabrication, challenges, and potentials in using *in-situ* alloying and multi-metal processing by L-PBF.

Fabrication using these routes is considered from the perspectives of materials and processing parameters. Although much progress has been achieved in modifying 3D printability of metals, limited alloys are available nowadays. Although various methods have been adopted to prepare the feedstock, more efficient and economic processes are in demand, especially for industrial production. This review addressed the influence of heat transfer and fluid flow in *in-situ* alloying and multi-metal processing. Defects associated with L-PBF need to be carefully controlled as complexity is added to the process for these approaches. Balling effect, porosity, crack, loss of alloying elements, oxide inclusions, intermetallic phases, and unmelted particles are all discussed. More investigations are necessary to overcome these challenges.

Ultimately, L-PBF offers to advance materials science and manufacturing technology in the future. By using *in-situ* alloying and multi-metal processing make it more promising for high-performance products. However, research in this field is relatively new and in the infancy stage, there is a need for accelerated trials and investigations for real-time applications to come to fruition.

Acknowledgement

The authors acknowledge the support from the National Research Foundation, Prime Minister's Office, Singapore under its Medium-Sized Centre funding scheme. S. Huang also acknowledge the Nanyang President's Graduate Scholarship from Nanyang Technological University, Singapore for funding the Ph.D. studies.

CRediT Author Statement

S. L. Sing: Conceptualization, Methodology, Writing – Original Draft, Writing – Review & Editing, Visualization, Supervision, Project Administration. **S. Huang:** Conceptualization, Methodology, Writing – Original Draft, Writing – Review & Editing. **G. D. Goh:** Writing – Review & Editing. **G. L. Goh:** Writing – Review & Editing. **C. F. Tey:** Writing – Original Draft. **J. H. K. Tan:** Writing – Original Draft. **W. Y. Yeong:** Conceptualization, Supervision, Project Administration, Funding Acquisition.

References

[1] Liu ZH, Zhang DQ, Chua CK, Leong KF. Crystal structure analysis of M2 high speed steel parts produced by selective laser melting. Materials Characterization. 2013;84:72-80.

[2] Sing SL, Yeong WY, Wiria FE, Tay BY. Characterization of titanium lattice structures fabricated by selective laser melting using an adapted compressive test method. Experimental Mechanics. 2016;56:735-48.

[3] Herzog D, Seyda V, Wycisk E, Emmelmann C. Additive manufacturing of metals. Acta Materialia. 2016;117:371-92.

[4] Sing SL, Yeong WY, Wiria FE, Tay BY, Zhao Z, Zhao L, et al. Direct selective laser sintering and melting of ceramics: a review. Rapid Prototyping Journal. 2017;23:611-23.

[5] Yap CY, Chua CK, Dong ZL, Liu ZH, Zhang DQ, Loh LE, et al. Review of selective laser melting: Materials and applications. Applied Physics Reviews. 2015;2:041101.

[6] Bogue R. Nanocomposites: a review of technology and applications. Assembly Automation. 2011;31:106-12.

[7] Yu WH, Sing SL, Chua CK, Kuo CN, Tian XL. Particle-Reinforced Metal Matrix Nanocomposites Fabricated by Selective Laser Melting: A State of the Art Review. Progress in Materials Science. 2019;104:330-79.

[8] Wu W, Tor SB, Chua CK, Leong KF, Merchant A. Investigation on processing of ASTM A131 Eh36 high tensile strength steel using selective laser melting. Virtual and Physical Prototyping. 2015;10:187-93.

[9] Meng L, Zhao J, Lan X, Yang H, Wang Z. Multi-objective optimisation of bio-inspired lightweight sandwich structures based on selective laser melting. Virtual and Physical Prototyping. 2020;15:106-19.

[10] Concli F, Gilioli A. Numerical and experimental assessment of the mechanical properties of 3D printed 18-Ni300 steel trabecular structures produced by Selective Laser Melting – a lean design approach. Virtual and Physical Prototyping. 2019;14:267-76.

[11] Anandan S, Hussein RM, Spratt M, Newkirk J, Chandrashekhara K, Misak H, et al. Failure In metal honeycombs manufactured by selective laser melting of 304 L stainless steel under compression. Virtual and Physical Prototyping. 2019;14:114-22.

[12] Sing SL, Huang S, Yeong WY. Effect of solution heat treatment on microstructure and mechanical properties of laser powder bed fusion produced cobalt-28chromium-6molybdenum. Materials Science and Engineering: A. 2020;769:138511.

[13] Yang J, Yu H, Yin J, Gao M, Wang Z, Zeng X. Formation and control of martensite in Ti-6Al-4V alloy produced by selective laser melting. Materials & Design. 2016;108:308-18.

[14] Liu ZH, Zhang DQ, Sing SL, Chua CK, Loh LE. Interfacial characterization of SLM parts in multi-material processing: Metallurgical diffusion between 316L stainless steel and C18400 copper alloy. Materials Characterization. 2014;94:116-25.

[15] Yang C, Zhao YJ, Kang LM, Li DD, Zhang WW, Zhang LC. High-strength silicon brass manufactured by selective laser melting. Materials Letters. 2018;210:169-72.

[16] Attar H, Bönisch M, Calin M, Zhang L-C, Zhuravleva K, Funk A, et al. Comparative study of microstructures and mechanical properties of in situ Ti–TiB composites produced by selective laser melting, powder metallurgy, and casting technologies. Journal of Materials Research. 2014;29:1941-50.

[17] Zhang LC, Xu J, Eckert J. Thermal stability and crystallization kinetics of mechanically alloyed TiC/Ti-based metallic glass matrix composite. Journal of Applied Physics. 2006;100:033514.

[18] Liu LH, Yang C, Wang F, Qu SG, Li XQ, Zhang WW, et al. Ultrafine grained Ti-based composites with ultrahigh strength and ductility achieved by equiaxing microstructure. Materials & Design. 2015;79:1-5.

[19] Kühn U, Mattern N, Gebert A, Kusy M, Boström M, Siegel U, et al. Nanostructured Zr-and Ti-based composite materials with high strength and enhanced plasticity. Journal of Applied Physics. 2005;98:054307.

[20] DebRoy T, Wei HL, Zuback JS, Mukherjee T, Elmer JW, Milewski JO, et al. Additive manufacturing of metallic components – Process, structure and properties. Progress in Materials Science. 2018;92:112-224.

[21] Gu DD, Meiners W, Wissenbach K, Poprawe R. Laser additive manufacturing of metallic components: materials, processes and mechanisms. International Materials Reviews. 2013;57:133-64.

[22] Olakanmi EO, Cochrane RF, Dalgarno KW. A review on selective laser sintering/melting (SLS/SLM) of aluminium alloy powders: Processing, microstructure, and properties. Progress in Materials Science. 2015;74:401-77.

[23] Sercombe TB, Li X. Selective laser melting of aluminium and aluminium metal matrix composites: a review. Materials Technology. 2016;31:77-85.

[24] Yadroitsev I, Gusarov AV, Yadroitsava I, Smurov I. Single track formation in selective laser melting of metal powders. Journal of Materials Processing Technology. 2010;210:1624-31.

[25] Markl M, Körner C. Multiscale Modeling of Powder Bed–Based Additive Manufacturing. Annual Review of Materials Research. 2016;46:93-123.

[26] AlMangour B, Grzesiak D, Borkar T, Yang J-M. Densification behavior, microstructural evolution, and mechanical properties of TiC/316L stainless steel nanocomposites fabricated by selective laser melting. Materials & Design. 2018;138:119-28.

[27] Ahn IH, Moon SK, Hwang J, Bi G. Characteristic length of the solidified melt pool in selective laser melting process. Rapid Prototyping Journal. 2017;23:370-81.

[28] Wang XC, Laoui T, Bonse J, Kruth J-P, Lauwers B, Froyen L. Direct selective laser sintering of hard metal powders: experimental study and simulation. The International Journal of Advanced Manufacturing Technology. 2002;19:351-7.

[29] Scharowsky T, Osmanlic F, Singer RF, Körner C. Melt pool dynamics during selective electron beam melting. Applied Physics A. 2013;114:1303-7.

[30] Arafune K, Hirata A. Thermal and solutal Marangoni convection in In–Ga–Sb system. Journal of Crystal Growth. 1999;197:811-7.

[31] Kovalev OB, Gurin AM. Multivortex convection of metal in molten pool with dispersed impurity induced by laser radiation. International Journal of Heat and Mass Transfer. 2014;68:269-77.

[32] Chan CL, Mazumder J, Chen MM. Effect of surface tension gradient driven convection in a laser melt pool: Three-dimensional perturbation model. Journal of Applied Physics. 1988;64:6166-74.

[33] Rongy L, De Wit A. Steady Marangoni flow traveling with chemical fronts. The Journal of Chemical Physics. 2006;124:164705.

[34] Fabbro R, Hamadou M, Coste F. Metallic vapor ejection effect on melt pool dynamics in deep penetration laser welding. Journal of Laser Applications. 2004;16:16-9.

[35] Fabbro R, Slimani S, Doudet I, Coste F, Briand F. Experimental study of the dynamical coupling between the induced vapour plume and the melt pool for Nd–Yag CW laser welding. Journal of Physics D: Applied Physics. 2006;39:394.

[36] Liu Y, Yang Y, Mai S, Wang D, Song C. Investigation into spatter behavior during selective laser melting of AISI 316L stainless steel powder. Materials & Design. 2015;87:797-806.

[37] Loh LE, Chua CK, Yeong WY, Song J, Mapar M, Sing SL, et al. Numerical investigation and an effective modelling on the Selective Laser Melting (SLM) process with aluminium alloy 6061. International Journal of Heat and Mass Transfer. 2015;80:288-300.

[38] Mahamood RM, Akinlabi ET. Effect of the Scanning Speed of Treatment on the Microstructure, Microhardness, Wear, and Corrosion Behavior of Laser Metal-Deposited Ti–6AL–4V/TiC Composite. Materials Science. 2017;53:76-85.

[39] Sing SL, Wiria FE, Yeong WY. Selective laser melting of lattice structures: A statistical approach to manufacturability and mechanical behavior. Robotics and Computer-Integrated Manufacturing. 2018;49:170-80.

[40] Thijs L, Verhaeghe F, Craeghs T, Humbeeck JV, Kruth J-P. A study of the microstructural evolution during selective laser melting of Ti–6Al–4V. Acta Materialia. 2010;58:3303-12.

[41] Saedi S, Shayesteh Moghaddam N, Amerinatanzi A, Elahinia M, Karaca HE. On the effects of selective laser melting process parameters on microstructure and thermomechanical response of Ni-rich NiTi. Acta Materialia. 2018;144:552-60.

[42] Simonelli M, Tuck C, Aboulkhair NT, Maskery I, Ashcroft I, Wildman RD, et al. A study on the laser spatter and the oxidation reactions during selective laser melting of 316L stainless steel, Al-Si10-Mg, and Ti-6Al-4V. Metallurgical and Materials Transactions A. 2015;46:3842-51.

[43] Yap CY, Chua CK, Dong ZL. An effective analytical model of selective laser melting. Virtual and Physical Prototyping. 2016;11:21-6.

[44] Yang J, Han J, Yu H, Yin J, Gao M, Wang Z, et al. Role of molten pool mode on formability, microstructure and mechanical properties of selective laser melted Ti-6Al-4V alloy. Materials & Design. 2016;110:558-70.

[45] Yadroitsev I, Krakhmalev P, Yadroitsava I. Selective laser melting of Ti6Al4V alloy for biomedical applications: Temperature monitoring and microstructural evolution. Journal of Alloys and Compounds. 2014;583:404-9.

[46] Kuo CN, Chua CK, Peng PC, Chen YW, Sing SL, Huang S, et al. Microstructure evolution and mechanical property response via 3D printing parameter development of Al-Sc alloy. Virtual and Physical Prototyping. 2020;15:120-9.

[47] Qiu C, Panwisawas C, Ward M, Basoalto HC, Brooks JW, Attallah MM. On the role of melt flow into the surface structure and porosity development during selective laser melting. Acta Materialia. 2015;96:72-9.

[48] Mishra P, Ilar T, Brueckner F, Kaplan A. Energy efficiency contributions and losses during selective laser melting. Journal of Laser Applications. 2018;30:032304.

[49] Yang Y, Wen S, Wei Q, Li W, Liu J, Shi Y. Effect of scan line spacing on texture, phase and nanohardness of TiAl/TiB 2 metal matrix composites fabricated by selective laser melting. Journal of Alloys and Compounds. 2017;728:803-14.

[50] Li R, Shi Y, Wang Z, Wang L, Liu J, Jiang W. Densification behavior of gas and water atomized 316L stainless steel powder during selective laser melting. Applied Surface Science. 2010;256:4350-6.

[51] Zhang S, Wei Q, Cheng L, Li S, Shi Y. Effects of scan line spacing on pore characteristics and mechanical properties of porous Ti6Al4V implants fabricated by selective laser melting. Materials & Design. 2014;63:185-93.

[52] Yadroitsev I, Thivillon L, Bertrand P, Smurov I. Strategy of manufacturing components with designed internal structure by selective laser melting of metallic powder. Applied Surface Science. 2007;254:980-3.

[53] Di W, Yongqiang Y, Xubin S, Yonghua C. Study on energy input and its influences on single-track, multi-track, and multi-layer in SLM. The International Journal of Advanced Manufacturing Technology. 2012;58:1189-99.

[54] Ma M, Wang Z, Gao M, Zeng X. Layer thickness dependence of performance in high-power selective laser melting of 1Cr18Ni9Ti stainless steel. Journal of Materials Processing Technology. 2015;215:142-50.

[55] Gu D, Shen Y. Processing and microstructure of submicron WC–Co particulate reinforced Cu matrix composites prepared by direct laser sintering. Materials Science and Engineering: A. 2006;435:54-61.

[56] Tang M, Pistorius PC, Beuth J. Geometric model to predict porosity of part produced in powder bed system. Materials Science and Technology Proceedings. 2015:129-35.

[57] Tang M, Pistorius PC. Oxides, porosity and fatigue performance of AlSi10Mg parts produced by selective laser melting. International Journal of Fatigue. 2017;94:192-201.

[58] Tang M. Inclusions, Porosity, and Fatigue of AlSi10Mg Parts Produced by Selective Laser Melting: Carnegie Mellon University; 2017.

[59] Gusarov AV, Yadroitsev I, Bertrand P, Smurov I. Heat transfer modelling and stability analysis of selective laser melting. Applied Surface Science. 2007;254:975-9.

[60] Li R, Liu J, Shi Y, Wang L, Jiang W. Balling behavior of stainless steel and nickel powder during selective laser melting process. The International Journal of Advanced Manufacturing Technology. 2011;59:1025-35.

[61] Kang N, Coddet P, Dembinski L, Liao H, Coddet C. Microstructure and strength analysis of eutectic Al-Si alloy in-situ manufactured using selective laser melting from elemental powder mixture. Journal of Alloys and Compounds. 2017;691:316-22.

[62] Kang N, Coddet P, Liao H, Baur T, Coddet C. Wear behavior and microstructure of hypereutectic Al-Si alloys prepared by selective laser melting. Applied Surface Science. 2016;378:142-9.

[63] Gode C, Yilmazer H, Ozdemir I, Todaka Y. Microstructural refinement and wear property of Al–Si–Cu composite subjected to extrusion and high-pressure torsion. Materials Science and Engineering: A. 2014;618:377-84.

[64] Hanemann T, Carter LN, Habschied M, Adkins NJE, Attallah MM, Heilmaier M. In-situ alloying of AlSi10Mg+Si using Selective Laser Melting to control the coefficient of thermal expansion. Journal of Alloys and Compounds. 2019;795:8-18.

[65] Kang N, Coddet P, Chen C, Wang Y, Liao H, Coddet C. Microstructure and wear behavior of in-situ hypereutectic Al–high Si alloys produced by selective laser melting. Materials & Design. 2016;99:120-6.

[66] Kang N, Coddet P, Liao H, Coddet C. Macrosegregation mechanism of primary silicon phase in selective laser melting hypereutectic Al – High Si alloy. Journal of Alloys and Compounds. 2016;662:259-62.

[67] Kang N, Coddet P, Ammar M-R, Liao H, Coddet C. Characterization of the microstructure of a selective laser melting processed Al-50Si alloy: Effect of heat treatments. Materials Characterization. 2017;130:243-9.

[68] Prashanth KG, Scudino S, Klauss HJ, Surreddi KB, Löber L, Wang Z, et al. Microstructure and mechanical properties of Al–12Si produced by selective laser melting: Effect of heat treatment. Materials Science and Engineering: A. 2014;590:153-60.

[69] Suryawanshi J, Prashanth KG, Scudino S, Eckert J, Prakash O, Ramamurty U. Simultaneous enhancements of strength and toughness in an Al-12Si alloy synthesized using selective laser melting. Acta Materialia. 2016;115:285-94.

[70] Martin JH, Yahata BD, Hundley JM, Mayer JA, Schaedler TA, Pollock TM. 3D printing of high-strength aluminium alloys. Nature. 2017;549:365.

[71] Montero-Sistiaga ML, Mertens R, Vrancken B, Wang X, Van Hooreweder B, Kruth J-P, et al. Changing the alloy composition of Al7075 for better processability by selective laser melting. Journal of Materials Processing Technology. 2016;238:437-45.

[72] Zhang H, Zhu H, Nie X, Yin J, Hu Z, Zeng X. Effect of Zirconium addition on crack, microstructure and mechanical behavior of selective laser melted Al-Cu-Mg alloy. Scripta Materialia. 2017;134:6-10.

[73] Wang P, Deng L, Prashanth KG, Pauly S, Eckert J, Scudino S. Microstructure and mechanical properties of Al-Cu alloys fabricated by selective laser melting of powder mixtures. Journal of Alloys and Compounds. 2018;735:2263-6.

[74] Martinez R, Todd I, Mumtaz K. In situ alloying of elemental Al-Cu12 feedstock using selective laser melting. Virtual and Physical Prototyping. 2019;14:242-52.

[75] Bartkowiak K, Ullrich S, Frick T, Schmidt M. New Developments of Laser Processing Aluminium Alloys via Additive Manufacturing Technique. Physics Procedia. 2011;12:393-401.

[76] Vora P, Mumtaz K, Todd I, Hopkinson N. AlSi12 in-situ alloy formation and residual stress reduction using anchorless selective laser melting. Additive Manufacturing. 2015;7:12-9.

[77] Vora P, Martinez R, Hopkinson N, Todd I, Mumtaz K. Customised Alloy Blends for In-Situ Al339 Alloy Formation Using Anchorless Selective Laser Melting. Technologies. 2017;5:24.

[78] Simonelli M, Aboulkhair NT, Cohen P, Murray JW, Clare AT, Tuck C, et al. A comparison of Ti-6Al-4V in-situ alloying in Selective Laser Melting using simply-mixed and satellited powder blend feedstocks. Materials Characterization. 2018;143:118-26.

[79] Simonelli M, McCartney DG, Barriobero-Vila P, Aboulkhair NT, Tse YY, Clare A, et al. The Influence of Iron in Minimizing the Microstructural Anisotropy of Ti-6Al-4V Produced by Laser Powder-Bed Fusion. Metallurgical and Materials Transactions A. 2020;51:2444-59.

[80] Vrancken B, Thijs L, Kruth JP, Van Humbeeck J. Microstructure and mechanical properties of a novel β titanium metallic composite by selective laser melting. Acta Materialia. 2014;68:150-8.

[81] Huber F, Papke T, Scheitler C, Hanrieder L, Merklein M, Schmidt M. In Situ Formation of a Metastable β-Ti Alloy by Laser Powder Bed Fusion (L-PBF) of Vanadium and Iron Modified Ti-6Al-4V. Metals. 2018;8:1067.

[82] Krakhmalev P, Yadroitsev I, Yadroitsava I, de Smidt O. Functionalization of Biomedical Ti6Al4V via In Situ Alloying by Cu during Laser Powder Bed Fusion Manufacturing. Materials. 2017;10:1154.

[83] Macpherson A, Li X, McCormick P, Ren L, Yang K, Sercombe TB. Antibacterial Titanium Produced Using Selective Laser Melting. JOM. 2017;69:2719-24.

[84] Qiu C, Fones A, Hamilton HGC, Adkins NJE, Attallah MM. A new approach to develop palladium-modified Ti-based alloys for biomedical applications. Materials & Design. 2016;109:98-111.

[85] Sing SL, An J, Yeong WY, Wiria FE. Laser and electron-beam powder-bed additive manufacturing of metallic implants: a review on processes, materials and designs. Journal of Orthopaedic Research. 2016;34:369-85.

[86] Ridzwan MIZ, Shuib S, Hassan AY, Shokri AA, Ibrahim MNM. Problem of stress shielding and improvement to the hip implant designs: a review. Journal of Medical Sciences. 2007;7:460-7.

[87] Wolff J. Das gesetz der transformation der knochen. A Hirshwald. 1892;1:1-152.

[88] Li Y, Yang C, Zhao H, Qu S, Li X, Li Y. New developments of Ti-based alloys for biomedical applications. Materials. 2014;7:1709-800.

[89] Niinomi M. Recent metallic materials for biomedical applications. Metallurgical and Materials Transactions A. 2002;33:477.

[90] Sundfeldt M, V Carlsson L, B Johansson C, Thomsen P, Gretzer C. Aseptic loosening, not only a question of wear: A review of different theories. Acta Orthopaedica. 2006;77:177-97.

[91] Wapner KL. Implications of metallic corrosion in total knee arthroplasty. Clinical Orthopaedics and Related Research. 1991;271:12-20.

[92] Kuroda D, Niinomi M, Morinaga M, Kato Y, Yashiro T. Design and mechanical properties of new β type titanium alloys for implant materials. Materials Science and Engineering: A. 1998;243:244-9.

[93] Zhuravleva K, Bönisch M, Prashanth K, Hempel U, Helth A, Gemming T, et al. Production of porous β-type Ti–40Nb alloy for biomedical applications: comparison of selective laser melting and hot pressing. Materials. 2013;6:5700-12.

[94] Sing SL, Wiria FE, Yeong WY. Selective laser melting of titanium alloy with 50 wt% tantalum: Effect of laser process parameters on part quality. International Journal of Refractory Metals and Hard Materials. 2018;77:120-7.

[95] Yang Y, Wang G, Liang H, Gao C, Peng S, Shen L, et al. Additive manufacturing of bone scaffolds. International Journal of Bioprinting. 2019;5:148.

[96] Al-Tamimi AA, Peach C, Bartolo P. Topology optimization of metallic locking compression plates produced using electron beam melting. The International Journal of Advanced Manufacturing Technology 2018;104:195-210.

[97] Aleixo GT, Afonso C, Coelho A, Caram R. Effects of Omega Phase on Elastic Modulus of Ti-Nb Alloys as a Function of Composition and Cooling Rate. Solid State Phenomena: Trans Tech Publ; 2008. p. 393-8.

[98] Sun Z, Tan X, Tor SB, Chua CK. Simultaneously enhanced strength and ductility for 3D-printed stainless steel 316L by selective laser melting. NPG Asia Materials. 2018;10:127-36.

[99] Ozaki T, Matsumoto H, Watanabe S, Hanada S. Beta Ti Alloys with Low Young's Modulus. Materials Transactions. 2004;45:2776-9.

[100] Hon Y-H, Wang J-Y, Pan Y-N. Composition/Phase Structure and Properties of Titanium-Niobium Alloys. Materials Transactions. 2003;44:2384-90.

[101] Collings EW. The physical metallurgy of titanium alloys. Metals Park Ohio. 1984;3.

[102] Long M, Rack HJ. Titanium alloys in total joint replacement—a materials science perspective. Biomaterials. 1998;19:1621-39.

[103] Kim HY, Miyazaki S. Martensitic Transformation and Superelastic Properties of Ti-Nb Base Alloys. Materials Transactions. 2015;56:625-34.

[104] Wang Q, Han C, Choma T, Wei Q, Yan C, Song B, et al. Effect of Nb content on microstructure, property and in vitro apatite-forming capability of Ti-Nb alloys fabricated via selective laser melting. Materials & Design. 2017;126:268-77.

[105] Fischer M, Joguet D, Robin G, Peltier L, Laheurte P. In situ elaboration of a binary Ti–26Nb alloy by selective laser melting of elemental titanium and niobium mixed powders. Materials Science and Engineering: C. 2016;62:852-9.

[106] Huang S, Sing SL, de looze G, Wilson R, Yeong WY. Laser powder bed fusion of titanium-tantalum alloys: Compositions and designs for biomedical applications. Journal of the Mechanical Behavior of Biomedical Materials. 2020;108:103775.

[107] Zhao D, Han C, Li Y, Li J, Zhou K, Wei Q, et al. Improvement on mechanical properties and corrosion resistance of titanium-tantalum alloys in-situ fabricated via selective laser melting. Journal of Alloys and Compounds. 2019;804:288-98.

[108] Brodie EG, Medvedev AE, Frith JE, Dargusch MS, Fraser HL, Molotnikov A. Remelt processing and microstructure of selective laser melted Ti25Ta. Journal of Alloys and Compounds. 2020;820:153082.

[109] Sing SL, Yeong WY, Wiria FE. Selective laser melting of titanium alloy with 50 wt% tantalum: Microstructure and mechanical properties. Journal of Alloys and Compounds. 2016;660:461-70.

[110] Huang S, Sing SL, Yeong WY. Selective Laser Melting of Ti42Nb Composite Powder and the Effect of Laser Re-Melting. Key Engineering Materials. 2019;801:270-5.

[111] Wang JC, Liu YJ, Qin P, Liang SX, Sercombe TB, Zhang LC. Selective laser melting of Ti–35Nb composite from elemental powder mixture: Microstructure, mechanical behavior and corrosion behavior. Materials Science and Engineering: A. 2019;760:214-24.

[112] Nagase T, Hori T, Todai M, Sun S-H, Nakano T. Additive manufacturing of dense components in beta-titanium alloys with crystallographic texture from a mixture of pure metallic element powders. Materials & Design. 2019;173:107771.

[113] Chlebus E, Kuźnicka B, Dziedzic R, Kurzynowski T. Titanium alloyed with rhenium by selective laser melting. Materials Science and Engineering: A. 2015;620:155-63.

[114] Majchrowicz K, Pakieła Z, Brynk T, Romelczyk-Baishya B, Płocińska M, Kurzynowski T, et al. Microstructure and mechanical properties of Ti–Re alloys manufactured by selective laser melting. Materials Science and Engineering: A. 2019;765:138290.

[115] Zhao D, Han C, Li J, Liu J, Wei Q. In situ fabrication of a titanium-niobium alloy with tailored microstructures, enhanced mechanical properties and biocompatibility by using selective laser melting. Materials Science and Engineering: C. 2020:110784.

[116] Liang H, Zhao D, Feng X, Ma L, Deng X, Han C, et al. 3D-printed porous titanium scaffolds incorporating niobium for high bone regeneration capacity. Materials & Design. 2020;194:108890.

[117] Yan L, Yuan Y, Ouyang L, Li H, Mirzasadeghi A, Li L. Improved mechanical properties of the new Ti-15Ta-xZr alloys fabricated by selective laser melting for biomedical application. Journal of Alloys and Compounds. 2016;688:156-62.

[118] Schwab H, Prashanth K, Löber L, Kühn U, Eckert J. Selective laser melting of Ti-45Nb alloy. Metals. 2015;5:686-94.

[119] Schulze C, Weinmann M, Schweigel C, Keßler O, Bader R. Mechanical Properties of a Newly Additive Manufactured Implant Material Based on Ti-42Nb. Materials. 2018;11:124.

[120] Chen W, Chen C, Zi X, Cheng X, Zhang X, Lin YC, et al. Controlling the microstructure and mechanical properties of a metastable β titanium alloy by selective laser melting. Materials Science and Engineering: A. 2018;726:240-50.

[121] Xie F, He X, Cao S, Mei M, Qu X. Influence of pore characteristics on microstructure, mechanical properties and corrosion resistance of selective laser sintered porous Ti–Mo alloys for biomedical applications. Electrochimica Acta. 2013;105:121-9.

[122] Azizi H, Zurob H, Bose B, Reza Ghiaasiaan S, Wang X, Coulson S, et al. Additive manufacturing of a novel Ti-Al-V-Fe alloy using selective laser melting. Additive Manufacturing. 2018;21:529-35.

[123] Wang C, Tan XP, Du Z, Chandra S, Sun Z, Lim CWJ, et al. Additive manufacturing of NiTi shape memory alloys using pre-mixed powders. Journal of Materials Processing Technology. 2019;271:152-61.

[124] Zhang B, Chen J, Coddet C. Microstructure and Transformation Behavior of in-situ Shape Memory Alloys by Selective Laser Melting Ti–Ni Mixed Powder. Journal of Materials Science & Technology. 2013;29:863-7.

[125] Liu S, Han S, Zhang L, Chen L-Y, Wang L, Zhang L, et al. Strengthening mechanism and micropillar analysis of high-strength NiTi–Nb eutectic-type alloy prepared by laser powder bed fusion. Composites Part B: Engineering. 2020;200:108358.

[126] Grigoriev A, Polozov I, Sufiiarov V, Popovich A. In-situ synthesis of Ti2AlNb-based intermetallic alloy by selective laser melting. Journal of Alloys and Compounds. 2017;704:434-42.

[127] Polozov I, Sufiiarov V, Popovich A, Masaylo D, Grigoriev A. Synthesis of Ti-5Al, Ti-6Al-7Nb, and Ti-22Al-25Nb alloys from elemental powders using powder-bed fusion additive manufacturing. Journal of Alloys and Compounds. 2018;763:436-45.

[128] Bolzoni L, Weissgaerber T, Kieback B, Ruiz-Navas EM, Gordo E. Mechanical behaviour of pressed and sintered CP Ti and Ti–6Al–7Nb alloy obtained from master alloy addition powder. Journal of the Mechanical Behavior of Biomedical Materials. 2013;20:149-61.

[129] Barriobero-Vila P, Gussone J, Stark A, Schell N, Haubrich J, Requena G. Peritectic titanium alloys for 3D printing. Nature Communications. 2018;9:3426.

[130] Kang N, El Mansori M, Guittonneau F, Liao H, Fu Y, Aubry E. Controllable mesostructure, magnetic properties of soft magnetic Fe-Ni-Si by using selective laser melting from nickel coated high silicon steel powder. Applied Surface Science. 2018;455:736-41.

[131] Shuai C, He C, Feng P, Guo W, Gao C, Wu P, et al. Biodegradation mechanisms of selective laser-melted Mg-xAl-Zn alloy: grain size and intermetallic phase. Virtual and Physical Prototyping. 2018;13:59-69.

[132] Long T, Zhang X, Huang Q, Liu L, Liu Y, Ren J, et al. Novel Mg-based alloys by selective laser melting for biomedical applications: microstructure evolution, microhardness and in vitro degradation behaviour. Virtual and Physical Prototyping. 2017;13:71-81.

[133] Zhang B, Liao H, Coddet C. Effects of processing parameters on properties of selective laser melting Mg–9%Al powder mixture. Materials & Design. 2012;34:753-8.

[134] Shuai C, Yang W, Yang Y, Gao C, He C, Pan H. A continuous net-like eutectic structure enhances the corrosion resistance of Mg alloys. International Journal of Bioprinting. 2019;5:207.

[135] Yang Y, Yuan F, Gao C, Feng P, Xue L, He S, et al. A combined strategy to enhance the properties of Zn by laser rapid solidification and laser alloying. Journal of the Mechanical Behavior of Biomedical Materials. 2018;82:51-60.

[136] Erinc M, Sillekens WH, Mannens RGTM, Werkhoven RJ. Applicability of existing magnesium alloys as biomedical implant materials. 2009.

[137] Shuai C, Xue L, Gao C, Yang Y, Peng S, Zhang Y. Selective laser melting of Zn–Ag alloys for bone repair: microstructure, mechanical properties and degradation behaviour. Virtual and Physical Prototyping. 2018;13:146-54.

[138] Jones JB, Cooper DE, Wimpenny DI, Gibbons GJ. Gateways Toward Dissimilar Multi-material Parts. RAPID 2012 and 3D Imaging Conferences & Exposition2012.

[139] Anstaett C, Seidel C, Reinhart G. Fabrication of 3D multi-material parts using laser-based powder bed fusion. Proceedings of the 28th Annual International Solid Freeform Fabrication Symposium2017.

[140] Beal VE, Erasenthiran P, Hopkinson N, Dickens P, Ahrens CH. Fabrication of x-graded H13 and Cu powder mix using high power pulsed Nd: YAG laser. Proceedings of Solid Freeform Fabrication Symposium2004.

[141] Sing SL, Lam LP, Zhang DQ, Liu ZH, Chua CK. Interfacial characterization of SLM parts in multi-material processing: Intermetallic phase formation between AlSi10Mg and C18400 copper alloy. Materials Characterization. 2015;107:220-7.

[142] Chen C, Gu D, Dai D, Du L, Wang R, Ma C, et al. Laser additive manufacturing of layered TiB2/Ti6Al4V multi-material parts: Understanding thermal behavior evolution. Optics & Laser Technology. 2019;119:105666.

[143] Nadimpalli VK, Dahmen T, Valente EH, Mohanty S, Pedersen DB. Multi-material additive manufacturing of steels using laser powder bed fusion. Euspen's 19th International Conference & Exhibition: The European Society for Precision Engineering and Nanotechnology; 2019. p. 240-3.

[144] Demir AG, Previtali B. Multi-material selective laser melting of Fe/Al-12Si components. Manufacturing letters. 2017;11:8-11.

[145] Hinojos A, Mireles J, Reichardt A, Frigola P, Hosemann P, Murr LE, et al. Joining of Inconel 718 and 316 Stainless Steel using electron beam melting additive manufacturing technology. Materials & Design. 2016;94:17-27.

[146] Terrazas CA, Gaytan SM, Rodriguez E, Espalin D, Murr LE, Medina F, et al. Multi-material metallic structure fabrication using electron beam melting. The International Journal of Advanced Manufacturing Technology. 2014;71:33-45.

[147] Chen J, Yang Y, Song C, Wang D, Wu S, Zhang M. Influence mechanism of process parameters on the interfacial characterization of selective laser melting 316L/CuSn10. Materials Science and Engineering: A. 2020.

[148] Chen J, Yang Y, Song C, Zhang M, Wu S, Wang D. Interfacial microstructure and mechanical properties of 316L /CuSn10 multi-material bimetallic structure fabricated by selective laser melting. Materials Science and Engineering: A. 2019;752:75-85.

[149] Chen K, Wang C, Hong Q, Wen S, Zhou Y, Yan C, et al. Selective laser melting 316L/CuSn10 multi-materials: Processing optimization, interfacial characterization and mechanical property. Journal of Materials Processing Technology. 2020;283:116701.

[150] Zhang M, Yang Y, Wang D, Song C, Chen J. Microstructure and mechanical properties of CuSn/18Ni300 bimetallic porous structures manufactured by selective laser melting. Materials & Design. 2019;165:107583.

[151] Bai Y, Zhang J, Zhao C, Li C, Wang H. Dual interfacial characterization and property in multi-material selective laser melting of 316L stainless steel and C52400 copper alloy. Materials Characterization. 2020;167:110489.

[152] Mei X, Wang X, Peng Y, Gu H, Zhong G, Yang S. Interfacial characterization and mechanical properties of 316L stainless steel/inconel 718 manufactured by selective laser melting. Materials Science and Engineering: A. 2019;758:185-91.

[153] Shakerin S, Hadadzadeh A, Amirkhiz BS, Shamsdini S, Li J, Mohammadi M. Additive manufacturing of maraging steel-H13 bimetals using laser powder bed fusion technique. Additive Manufacturing. 2019;29:100797.

[154] Gorny B, Niendorf T, Lackmann J, Thoene M, Troester T, Maier HJ. In situ characterization of the deformation and failure behavior of non-stochastic porous structures processed by selective laser melting. Materials Science and Engineering: A. 2011;528:7962-7.

[155] Yan C, Hao L, Hussein A, Young P, Raymont D. Advanced lightweight 316L stainless steel cellular lattice structures fabricated via selective laser melting. Materials & Design. 2014;55:533-41.

[156] Böhm C, Werz M, Weihe S. Dilution Ratio and the Resulting Composition Profile in Dissimilar Laser Powder Bed Fusion of AlSi10Mg and Al99.8. Metals. 2020;10:1222.

[157] Hadadzadeh A, Amirkhiz BS, Shakerin S, Kelly J, Li J, Mohammadi M. Microstructural investigation and mechanical behavior of a two-material component fabricated through selective laser melting of AlSi10Mg on an Al-Cu-Ni-Fe-Mg cast alloy substrate. Additive Manufacturing. 2020;31:10937.

[158] Wang R, Gu D, Chen C, Dai D, Ma C, Zhang H. Formation mechanisms of TiB2 tracks on Ti6Al4V alloy during selective laser melting of ceramic-metal multi-material. Powder Technology. 2020;367:597-607.

[159] Wei K, Zeng X, Li F, Liu M, Deng J. Microstructure and Mechanical Property of Ti-5Al-2.5Sn/Ti-6Al-4V Dissimilar Titanium Alloys Integrally Fabricated by Selective Laser Melting. JOM. 2020;72:1031-8.

[160] Bartolomeu F, Costa MM, Alves N, Miranda G, Silva FS. Additive manufacturing of NiTi-Ti6Al4V multi-material cellular structures targeting orthopedic implants. Optics & Laser Technology. 2020;134:106208.

[161] Gu D, Shen Y. Balling phenomena in direct laser sintering of stainless steel powder: Metallurgical mechanisms and control methods. Materials & Design. 2009;30:2903-10.

[162] Loh LE, Liu ZH, Zhang DQ, Mapar M, Sing SL, Chua CK, et al. Selective laser melting of aluminium alloy using a uniform beam profile. Virtual and Physical Prototyping. 2014;9:11-6.

[163] Qi H, Azer M, Ritter A. Studies of standard heat treatment effects on microstructure and mechanical properties of laser net shape manufactured Inconel 718. Metallurgical and Materials Transactions A. 2009;40:2410-22.

[164] Zhou J, Tsai H-L. Porosity formation and prevention in pulsed laser welding. Journal of Heat Transfer. 2007;129:1014-24.

[165] Panwisawas C, Qiu CL, Sovani Y, Brooks JW, Attallah MM, Basoalto HC. On the role of thermal fluid dynamics into the evolution of porosity during selective laser melting. Scripta Materialia. 2015;105:14-7.

[166] Khairallah SA, Anderson AT, Rubenchik A, King WE. Laser powder-bed fusion additive manufacturing: Physics of complex melt flow and formation mechanisms of pores, spatter, and denudation zones. Acta Materialia. 2016;108:36-45.

[167] Kasperovich G, Haubrich J, Gussone J, Requena G. Correlation between porosity and processing parameters in TiAl6V4 produced by selective laser melting. Materials & Design. 2016;105:160-70.

[168] Katayama S. Introduction: fundamentals of laser welding. Handbook of Laser Welding Technologies: Elsevier; 2013. p. 3-16.

[169] Weingarten C, Buchbinder D, Pirch N, Meiners W, Wissenbach K, Poprawe R. Formation and reduction of hydrogen porosity during selective laser melting of AlSi10Mg. Journal of Materials Processing Technology. 2015;221:112-20.

[170] Dai D, Gu D. Effect of metal vaporization behavior on keyhole-mode surface morphology of selective laser melted composites using different protective atmospheres. Applied Surface Science. 2015;355:310-9.

[171] Chahal V, Taylor RM. A review of geometric sensitivities in laser metal 3D printing. Virtual and Physical Prototyping. 2020;15:227-41.

[172] Salmi A, Atzeni E. Residual stress analysis of thin AlSi10Mg parts produced by Laser Powder Bed Fusion. Virtual and Physical Prototyping. 2020;15:49-61.

[173] Kempen K, Thijs L, Vrancken B, Buls S, Van Humbeeck J, Kruth JP. Producing crack-free, high density M2 Hss parts by selective laser melting: pre-heating the baseplate. Proceedings of the 24th International Solid Freeform Fabrication Symposium2013. p. 131-9.

[174] Robinson JH, Ashton IRT, JOnes E, Fox P, Sutcliffe C. The effect of hatch angle rotation on parts manufactured using selective laser melting. Rapid Prototyping Journal. 2019;25:289-98.

[175] Gåård A, Krakhmalev P, Bergström J. Microstructural characterization and wear behavior of (Fe, Ni)–TiC MMC prepared by DMLS. Journal of Alloys and Compounds. 2006;421:166-71.

[176] Mercelis P, Kruth J-P. Residual stresses in selective laser sintering and selective laser melting. Rapid Prototyping Journal. 2006;12:254-65.

[177] Zhu HH, Lu L, Fuh JYH. Study on shrinkage behaviour of direct laser sintering metallic powder. Proceedings of the Institution of Mechanical Engineers, Part B: Journal of Engineering Manufacture. 2006;220:183-90.

[178] AlMangour B, Grzesiak D. Selective laser melting of TiC reinforced 316L stainless steel matrix nanocomposites: Influence of starting TiC particle size and volume content. Materials & Design. 2016;104:141-51.

[179] Wei C, Li L, Zhang X, Chueh Y-H. 3D printing of multiple metallic materials via modified selective laser melting. CIRP Annals. 2018;67:245-8.

[180] Ramasamy S, Albright CE. CO2 and Nd: YAG laser beam welding of 6111-T4 aluminum alloy for automotive applications. Journal of Laser Applications. 2000;12:101-15.

[181] Zhao H, DebRoy T. Weld metal composition change during conduction mode laser welding of aluminum alloy 5182. Metallurgical and Materials Transactions B. 2001;32:163-72.

[182] Collur MM, Paul A, DebRoy T. Mechanism of alloying element vaporization during laser welding. Metallurgical Transactions B. 1987;18:733-40.

[183] Pastor M, Zhao H, Martukanitz R, DebRoy T. Porosity, underfill and magnesium lose during continuous wave Nd: YAG laser welding of thin plates of aluminum alloys 5182 and 5754. Welding Journal. 1999;78:207-S-16-S.

[184] Louvis E, Fox P, Sutcliffe CJ. Selective laser melting of aluminium components. Journal of Materials Processing Technology. 2011;211:275-84.

[185] Cao X, Wallace W, Immarigeon J-P, Poon C. Research and progress in laser welding of wrought aluminum alloys. II. Metallurgical microstructures, defects, and mechanical properties. Materials and Manufacturing Processes. 2003;18:23-49.

[186] Katayama S, Seto N, Mizutani M, Matsunawa A. Formation mechanism of porosity in high power YAG laser welding. Proceedings of the International Congress on Applications of Lasers and Electro-optics: ICALEO: Springer-Verlag; 2000. p. 200016.

[187] Read N, Wang W, Essa K, Attallah MM. Selective laser melting of AlSi10Mg alloy: Process optimisation and mechanical properties development. Materials & Design. 2015;65:417-24.

[188] Kang N, Li Y, Lin X, Feng E, Huang W. Microstructure and tensile properties of Ti-Mo alloys manufactured via using laser powder bed fusion. Journal of Alloys and Compounds. 2019;771:877-84.

[189] Lu Y, Dong Y, Jiang L, Wang T, Li T, Zhang Y. A criterion for topological close-packed phase formation in high entropy alloys. Entropy. 2015;17:2355-66.

[190] Tan C, Zhang X, Dong D, Attard B, Wang D, Kuang M, et al. In-situ synthesised interlayer enhances bonding strength in additively manufactured multi-material hybrid tooling. International Journal of Machine Tools and Manufacture. 2020;155:103592.

[191] Ting W, Zhang B-G, Feng J-C. Influences of different filler metals on electron beam welding of titanium alloy to stainless steel. Transactions of Nonferrous Metals Society of China. 2014;24:108-14.

[192] Bobbio LD, Otis RA, Borgonia JP, Dillon RP, Shapiro AA, Liu Z-K, et al. Additive manufacturing of a functionally graded material from Ti-6Al-4V to Invar: Experimental characterization and thermodynamic calculations. Acta Materialia. 2017;127:133-42.

[193] Sahasrabudhe H, Harrison R, Carpenter C, Bandyopadhyay A. Stainless steel to titanium bimetallic structure using LENS™. Additive Manufacturing. 2015;5:1-8.

[194] Kundu S, Ghosh M, Laik A, Bhanumurthy K, Kale GB, Chatterjee S. Diffusion bonding of commercially pure titanium to 304 stainless steel using copper interlayer. Materials Science and Engineering: A. 2005;407:154-60.

[195] Tomashchuk I, Sallamand P, Andrzejewski H, Grevey D. The formation of intermetallics in dissimilar Ti6Al4V/copper/AISI 316 L electron beam and Nd: YAG laser joints. Intermetallics. 2011;19:1466-73.

[196] Muralimohan CH, Ashfaq M, Ashiri R, Muthupandi V, Sivaprasad K. Analysis and characterization of the role of Ni interlayer in the friction welding of titanium and 304 austenitic stainless steel. Metallurgical and Materials Transactions A. 2016;47:347-59.

[197] Sam S, Kundu S, Chatterjee S. Diffusion bonding of titanium alloy to micro-duplex stainless steel using a nickel alloy interlayer: interface microstructure and strength properties. Materials & Design. 2012;40:237-44.

[198] Lee JG, Lee M-K. Microstructure and mechanical behavior of a titanium-to-stainless steel dissimilar joint brazed with Ag-Cu alloy filler and an Ag interlayer. Materials Characterization. 2017;129:98-103.

[199] Deng Y, Sheng G, Xu C. Evaluation of the microstructure and mechanical properties of diffusion bonded joints of titanium to stainless steel with a pure silver interlayer. Materials & Design. 2013;46:84-7.

[200] Cheepu M, Ashfaq M, Muthupandi V. A new approach for using interlayer and analysis of the friction welding of titanium to stainless steel. Transactions of the Indian Institute of Metals. 2017;70:2591-600.

[201] Kundu S, Sam S, Chatterjee S. Interfacial reactions and strength properties in dissimilar titanium alloy/Ni alloy/microduplex stainless steel diffusion bonded joints. Materials Science and Engineering: A. 2013;560:288-95.

[202] Reichardt A, Dillon RP, Borgonia JP, Shapiro AA, McEnerney BW, Momose T, et al. Development and characterization of Ti-6Al-4V to 304L stainless steel gradient components fabricated with laser deposition additive manufacturing. Materials & Design. 2016;104:404-13.

[203] Ishida K, Gao Y, Nagatsuka K, Takahashi M, Nakata K. Microstructures and mechanical properties of friction stir welded lap joints of commercially pure titanium and 304 stainless steel. Journal of Alloys and Compounds. 2015;630:172-7.

[204] Aleman B, Gutiérrez L, Urcola JJ. Interface microstructures in diffusion bonding of titanium alloys to stainless and low alloy steels. Materials Science and Technology. 1993;9:633-41.

[205] Song TF, Jiang XS, Shao ZY, Fang YJ, Mo DF, Zhu DG, et al. Microstructure and mechanical properties of vacuum diffusion bonded joints between Ti-6Al-4V titanium alloy and AISI316L stainless steel using Cu/Nb multi-interlayer. Vacuum. 2017;145:68-76.

[206] Mudali UK, Rao BMA, Shanmugam K, Natarajan R, Raj B. Corrosion and microstructural aspects of dissimilar joints of titanium and type 304L stainless steel. Journal of Nuclear Materials. 2003;321:40-8.

[207] Chiba A, Nishida M, Morizono Y, Imamura K. Bonding characteristics and diffusion barrier effect of the TiC phase formed at the bonding interface in an explosively welded titanium/high-carbon steel clad. Journal of Phase Equilibria. 1995;16:411-5.

[208] Nishida M, Chiba A, Honda Y, Hirazumi J-i, Horikiri K. Electron microscopy studies of bonding interface in explosively welded Ti/steel clads. ISIJ International. 1995;35:217-9.

[209] Liao J, Yamamoto N, Liu H, Nakata K. Microstructure at friction stir lap joint interface of pure titanium and steel. Materials Letters. 2010;64:2317-20.

[210] Wei HL, Elmer JW, DebRoy T. Origin of grain orientation during solidification of an aluminum alloy. Acta Materialia. 2016;115:123-31.

[211] Li XP, Van Humbeeck J, Kruth JP. Selective laser melting of weak-textured commercially pure titanium with high strength and ductility: A study from laser power perspective. Materials & Design. 2017;116:352-8.

[212] Sing SL, Yeong WY. Laser powder bed fusion for metal additive manufacturing: perspectives on recent developments. Virtual and Physical Prototyping. 2020;15:359-70.

[213] Thijs L, Montero Sistiaga ML, Wauthle R, Xie Q, Kruth J-P, Van Humbeeck J. Strong morphological and crystallographic texture and resulting yield strength anisotropy in selective laser melted tantalum. Acta Materialia. 2013;61:4657-68.

[214] Gu D, Guo M, Zhang H, SUn Y, Wang R, Zhang L. Effects of laser scanning strategies on selective laser melting of pure tungsten. International Journal of Extreme Manufacturing. 2020;2:025001.

[215] AlMangour B, Grzesiak D, Yang J-M. Scanning strategies for texture and anisotropy tailoring during selective laser melting of TiC/316L stainless steel nanocomposites. Journal of Alloys and Compounds. 2017;728:424-35.

[216] Thijs L, Kempen K, Kruth J-P, Van Humbeeck J. Fine-structured aluminium products with controllable texture by selective laser melting of pre-alloyed AlSi10Mg powder. Acta Materialia. 2013;61:1809-19.

[217] Aboulkhair NT, Everitt NM, Ashcroft I, Tuck C. Reducing porosity in AlSi10Mg parts processed by selective laser melting. Additive Manufacturing. 2014;1:77-86.

[218] Bidare P, Maier RRJ, Beck RJ, Shephard JD, Moore AJ. An open-architecture metal powder bed fusion system for in-situ process measurements. Additive Manufacturing. 2017;16:177-85.

[219] Bidare P, Bitharas I, Ward RM, Attallah MM, Moore AJ. Fluid and particle dynamics in laser powder bed fusion. Acta Materialia. 2018;142:107-20.

[220] Matthews MJ, Guss G, Khairallah SA, Rubenchik AM, Depond PJ, King WE. Denudation of metal powder layers in laser powder bed fusion processes. Acta Materialia. 2016;114:33-42.

[221] Guo Q, Zhao C, Escano LI, Young Z, Xiong L, Fezzaa K, et al. Transient dynamics of powder spattering in laser powder bed fusion additive manufacturing process revealed by in-situ high-speed high-energy x-ray imaging. Acta Materialia. 2018;151:169-80.

[222] Gunenthiram V, Peyre P, Schneider M, Dal M, Coste F, Koutiri I, et al. Experimental analysis of spatter generation and melt-pool behavior during the powder bed laser beam melting process. Journal of Materials Processing Technology. 2018;251:376-86.

[223] Li XP, Kang CW, Huang H, Sercombe TB. The role of a low-energy–density re-scan in fabricating crack-free Al85Ni5Y6Co2Fe2 bulk metallic glass composites via selective laser melting. Materials & Design. 2014;63:407-11.

[224] Yasa E, Deckers J, Kruth JP. The investigation of the influence of laser re-melting on density, surface quality and microstructure of selective laser melting parts. Rapid Prototyping Journal. 2011;17:312-27.

[225] Yu WH, Sing SL, Chua CK, Tian XL. Influence of re-melting on surface roughness and porosity of AlSi10Mg parts fabricated by selective laser melting. Journal of Alloys and Compounds. 2019;792:574-81.

[226] Brodie EG, Richter J, Wegener T, Niendorf T, Molotnikov A. Low-cycle fatigue performance of remelted laser powder bed fusion (L-PBF) biomedical Ti25Ta. Materials Science and Engineering: A. 2020;798:140228.

[227] Zafari A, Xia K. High Ductility in a fully martensitic microstructure: a paradox in a Ti alloy produced by selective laser melting. Materials Research Letters. 2018;6:627-33.

[228] Zafari A, Lui EW, Jin S, Li M, Molla TT, Sha G, et al. Hybridisation of microstructures from three classes of titanium alloys. Materials Science and Engineering: A. 2020;788:139572.

[229] Zhao C, Wang Z, Li D, Xie M, Kollo L, Luo Z, et al. Comparison of additively manufacturing samples fabricated from pre-alloyed and mechanically mixed powders. Journal of Alloys and Compounds. 2020;830:154603.

[230] Chen P, Li S, Zhou Y, Yan M, Attallah MM. Fabricating CoCrFeMnNi high entropy alloy via selective laser melting in-situ alloying. Journal of Materials Science & Technology. 2020;43:40-3.

[231] Rashid R, Masood SH, Ruan D, Palanisamy S, Rahman Rashid RA, Elambasseril J, et al. Effect of energy per layer on the anisotropy of selective laser melted AlSi12 aluminium alloy. Additive Manufacturing. 2018;22:426-39.

[232] Brandl E, Heckenberger U, Holzinger V, Buchbinder D. Additive manufactured AlSi10Mg samples using Selective Laser Melting (SLM): Microstructure, high cycle fatigue, and fracture behavior. Materials & Design. 2012;34:159-69.

[233] Tolosa I, Garciandía F, Zubiri F, Zapirain F, Esnaola A. Study of mechanical properties of AISI 316 stainless steel processed by "selective laser melting", following different manufacturing strategies. The International Journal of Advanced Manufacturing Technology. 2010;51:639-47.

[234] Li P, Li J, Xiong J, Zhang F, Raza SH. Diffusion bonding titanium to stainless steel using Nb/Cu/Ni multi-interlayer. Materials Characterization. 2012;68:82-7.

[235] Hofmann DC, Roberts S, Otis R, Kolodziejska J, Dillon RP, Suh J-o, et al. Developing gradient metal alloys through radial deposition additive manufacturing. Scientific Reports. 2014;4:5357.

[236] Wang T, Zhang B, Chen G, Feng J. High strength electron beam welded titanium–stainless steel joint with V/Cu based composite filler metals. Vacuum. 2013;94:41-7.

[237] Tey CF, Tan X, Sing SL, Yeong WY. Additive manufacturing of multiple materials by selective laser melting: Ti-alloy to stainless steel via a Cu-alloy interlayer. Additive Manufacturing. 2020;31:100970.

[238] Li R, Niu P, Yuan T, Cao P, Chen C, Zhou K. Selective laser melting of an equiatomic CoCrFeMnNi high-entropy alloy: Processability, non-equilibrium microstructure and mechanical property. Journal of Alloys and Compounds. 2018;746:125-34.

[239] Ren J, Mahajan C, Liu L, Follette D, Chen W, Mukherjee S. Corrosion Behavior of Selectively Laser Melted CoCrFeMnNi High Entropy Alloy. Metals. 2019;9:1029.

[240] Kim Y-K, Choe J, Lee K-A. Selective laser melted equiatomic CoCrFeMnNi high-entropy alloy: Microstructure, anisotropic mechanical response, and multiple strengthening mechanism. Journal of Alloys and Compounds. 2019;805:680-91.

[241] Xu Z, Zhang H, Li W, Mao A, Wang L, Song G, et al. Microstructure and nanoindentation creep behavior of CoCrFeMnNi high-entropy alloy fabricated by selective laser melting. Additive Manufacturing. 2019;28:766-71.

[242] Lin D, Xu L, Jing H, Han Y, Zhao L, Minami F. Effects of annealing on the structure and mechanical properties of FeCoCrNi high-entropy alloy fabricated via selective laser melting. Additive Manufacturing. 2020;32:101058.

[243] Song M, Zhou R, Gu J, Wang Z, Ni S, Liu Y. Nitrogen induced heterogeneous structures overcome strength-ductility trade-off in an additively manufactured high-entropy alloy. Applied Materials Today. 2020;18:100498.

[244] Sun Z, Tan XP, Descoins M, Mangelinck D, Tor SB, Lim CS. Revealing hot tearing mechanism for an additively manufactured high-entropy alloy via selective laser melting. Scripta Materialia. 2019;168:129-33.

[245] Niu PD, Li RD, Yuan TC, Zhu SY, Chen C, Wang MB, et al. Microstructures and properties of an equimolar AlCoCrFeNi high entropy alloy printed by selective laser melting. Intermetallics. 2019;104:24-32.

[246] Agrawal P, Thapliyal S, Nene SS, Mishra RS, McWilliams BA, Cho KC. Excellent strength-ductility synergy in metastable high entropy alloy by laser powder bed additive manufacturing. Additive Manufacturing. 2020;32:101098.

[247] Han C, Fang Q, Shi Y, Tor SB, Chua CK, Zhou K. Recent Advances on High-Entropy Alloys for 3D Printing. Advanced Materials. 2020:1903855.

[248] Chen S, Tong Y, Liaw PK. Additive Manufacturing of High-Entropy Alloys: A Review. Entropy. 2018;20:937.

[249] Luo S, Zhao C, Su Y, Liu Q, Wang Z. Selective laser melting of dual phase AlCrCuFeNix high entropy alloys: Formability, heterogeneous microstructures and deformation mechanisms. Additive Manufacturing. 2020;31:100925.

[250] Ewald S, Kies F, Hermsen S, Voshage M, Hasse C, Schleifenbaum JH. Rapid Alloy Development of Extremely High-Alloyed Metals Using Powder Blends in Laser Powder Bed Fusion. Materials. 2019;12:1706.

[251] Cordisco FA, Zavattieri PD, Hector Jr. LG, Bower AF. Toughness of a patterned interface between two elastically dissimilar solids. Engineering Fracture Mechanics. 2012;96:192-208.

[252] Cordisco FA, Zavattieri PD, Hector Jr. LG, Carlson BE. Mode I fracture along adhesively bonded sinusoidal interfaces. International Journal of Solids and Structures. 2016;83:45-64.

[253] Li B-W, Zhao H-P, Qin Q-H, Feng X-Q, Yu S-W. Numerical study on the effects of hierarchical wavy interface morphology on fracture toughness. Computational Materials Science. 2012;57:14-22.

[254] Al-Jamal OM, Hinduja S, Li L. Characteristics of the bond in Cu-H13 tool steel parts fabricated using SLM. CIRP Annals. 2008;57:239-42.

[255] Yang S, Evans JRG. A multi-component powder dispensing system for three dimensional functional gradients. Materials Science and Engineering: A. 2004;379:351-9.

[256] Hegge HJ, De Hosson JTM. The influence of convection on the homogeneity of laser-applied coatings. Journal of Materials Science. 1991;26:711-4.

[257] Wei C, Sun Z, Chen Q, Liu Z, Li L. Additive Manufacturing of Horizontal and 3D Functionally Graded 316L/Cu10Sn Components via Multiple Material Selective Laser Melting Journal of Manufacturing Science and Engineering. 2019;141:081014.

[258] Guo C, Ge W, Lin F. Dual-Material Electron Beam Selective Melting: Hardware Development and Validation Studies. Engineering. 2015;1:124-30.

[259] Zhang X, Chuen Y-h, Wei C, Sun Z, Yan J, Li L. Additive manufacturing of three-dimensional metal-glass functionally gradient material components by laser powder bed fusion with in situ powder mixing. Additive Manufacturing. 2020;33:101113.

[260] Chivel Y. New Approach to Multi-material Processing in Selective Laser Melting. Physics Procedia. 2016;83:891-8.

[261] Chapter 16 - Gravity Separation. In: Gupta A, Yan D, editors. Mineral Processing Design and Operations (Second Edition). Amsterdam: Elsevier; 2016. p. 563-628.

[262] Horn M, Prestel L, Schmitt M, Binder M, Schlick G, Seidel C, et al. Multi-Material Additive Manufacturing – Recycling of binary Metal Powder Mixtures by Screening. Procedia CIRP. 2020;93:50-5.

[263] Wu Y-C, San C-H, Chang C-H, Lin H-J, Marwan R, Baba S, et al. Numerical modeling of melt-pool behavior in selective laser melting with random powder distribution and experimental validation. Journal of Materials Processing Technology. 2018;254:72-8.

[264] Leitz K-H, Grohs C, Singer P, Tabernig B, Plankensteiner A, Kestler H, et al. Fundamental analysis of the influence of powder characteristics in Selective Laser Melting of molybdenum based on a multi-physical simulation model. International Journal of Refractory Metals and Hard Materials. 2018;72:1-8.

[265] Ding X, Wang L. Heat transfer and fluid flow of molten pool during selective laser melting of AlSi10Mg powder: Simulation and experiment. Journal of Manufacturing Processes. 2017;26:280-9.

[266] Bruna-Rosso C, Demir AG, Previtali B. Selective laser melting finite element modeling: Validation with high-speed imaging and lack of fusion defects prediction. Materials & Design. 2018;156:143-53.

[267] Arısoy YM, Criales LE, Özel T. Modeling and simulation of thermal field and solidification in laser powder bed fusion of nickel alloy IN625. Optics & Laser Technology. 2019;109:278-92.

[268] Wang X, Chou K. Microstructure simulations of Inconel 718 during selective laser melting using a phase field model. The International Journal of Advanced Manufacturing Technology. 2019;100:2147-62.

[269] Radhakrishnan B, Gorti SB, Turner JA, Acharya R, Sharon JA, Staroselsky A, et al. Phase Field Simulations of Microstructure Evolution in IN718 Using a Surrogate Ni–Fe–Nb Alloy during Laser Powder Bed Fusion†. Metals. 2019;9:14.

[270] Kyogoku H, Ikeshoji T-T. A review of metal additive manufacturing technologies: Mechanism of defects formation and simulation of melting and solidification phenomena in laser powder bed fusion process. Mechanical Engineering Reviews. 2020;7:19-00182.

[271] Schoinochoritis B, Chantzis D, Salonitis K. Simulation of metallic powder bed additive manufacturing processes with the finite element method: A critical review. Proceedings of the Institution of Mechanical Engineers, Part B: Journal of Engineering Manufacture. 2015;231:96-117.

[272] Tan JHK, Sing SL, Yeong WY. Microstructure modelling for metallic additive manufacturing: a review. Virtual and Physical Prototyping. 2020;15:87-105.

[273] Sorkin A, Tan JL, Wong CH. Multi-material modelling for selective laser melting. Procedia Engineering. 2017;216:51-7.

[274] Gu H, Wei C, Li L, Han Q, Setchi R, Ryan M, et al. Multi-physics modelling of molten pool development and track formation in multi-track, multi-layer and multi-material selective laser melting. International Journal of Heat and Mass Transfer. 2020;151:119458.

[275] Yan W, Ge W, Smith J, Lin S, Kafka OL, Lin F, et al. Multi-scale modeling of electron beam melting of functionally graded materials. Acta Materialia. 2016;115:403-12.

[276] Sun Z, Chuen Y-h, Li L. Multiphase mesoscopic simulation of multiple and functionally gradient materials laser powder bed fusion additive manufacturing processes. Additive Manufacturing. 2020;35:101448.

[277] Li X, Willy HJ, Chang S, Lu W, Herng TS, Ding J. Selective laser melting of stainless steel and alumina composite: Experimental and simulation studies on processing parameters, microstructure and mechanical properties. Materials & Design. 2018;145:1-10.

[278] Gan J, Gao H, Wen S, Zhou Y, Tan S, Duan L. Simulation, forming process and mechanical property of Cu-Sn-Ti/diamond composites fabricated by selective laser melting. International Journal of Refractory Metals and Hard Materials. 2020;87:105144.

[279] Xia M, Gu D, Ma C, Zhang H, Dai D, Chen H, et al. Fragmentation and refinement behavior and underlying thermodynamic mechanism of WC reinforcement during selective laser melting of Ni-based composites. Journal of Alloys and Compounds. 2019;777:693-702.

[280] Gu D, Yang Y, Xi L, Yang J, Xia M. Laser absorption behavior of randomly packed powder-bed during selective laser melting of SiC and TiB2 reinforced Al matrix composites. Optics & Laser Technology. 2019;119:105600.

[281] Dai D, Gu D, Ge Q, Li Y, Shi X, Sun Y, et al. Mesoscopic study of thermal behavior, fluid dynamics and surface morphology during selective laser melting of Ti-based composites. Computational Materials Science. 2020;177:109598.

[282] Gu D, Xia M, Dai D. On the role of powder flow behavior in fluid thermodynamics and laser processability of Ni-based composites by selective laser melting. International Journal of Machine Tools and Manufacture. 2019;137:67-78.

[283] Goh GD, Sing SL, Yeong WY. A review on machine learning in 3D printing: applications, potential, and challenges. Artificial Intelligence Review. 2020.

[284] Mahmoudi M, Ezzat AA, Elwany A. Layerwise Anomaly Detection in Laser Powder-Bed Fusion Metal Additive Manufacturing. Journal of Manufacturing Science and Engineering. 2019;141:031002.

[285] Özel T, Altay A, Kaftanoğlu B, Leach R, Senin N, Donmez A. Focus Variation Measurement and Prediction of Surface Texture Parameters Using Machine Learning in Laser Powder Bed Fusion. Journal of Manufacturing Science and Engineering. 2020;12:011008.

[286] Kwon O, Kim HG, Ham MJ, Kim W, Kim G-H, Cho J-H, et al. A deep neural network for classification of melt-pool images in metal additive manufacturing. Journal of Intelligent Manufacturing. 2020;31:375-86.

[287] Kunkel MH, Gebhardt A, Mpofu K, Kallweit S. Quality assurance in metal powder bed fusion via deep-learning-based image classification. Rapid Prototyping Journal. 2019;26:259-66.

[288] Meng L, McWilliams B, Jarosinski W, Park H-Y, Jung Y-G, Lee J, et al. Machine Learning in Additive Manufacturing: A Review. JOM. 2020;72:2363-77.

[289] Qi X, Chen G, Li Y, Cheng X, Li C. Applying Neural-Network-Based Machine Learning to Additive Manufacturing: Current Applications, Challenges, and Future Perspectives. Engineering. 2019;5:721-9.

[290] Rudolph J-P, Emmelmann C. Self-learning Calculation for Selective Laser Melting. Procedia CIRP. 2018;67:185-90.

[291] Renken V, Albinger S, Goch G, Neef A, Emmelmann C. Development of an adaptive, self-learning control concept for an additive manufacturing process. CIRP Journl of Manufacturing Science and Technology. 2017;19:57-61.

[292] Baturynska I, Semeniuta O, Martinsen K. Optimization of process parameters for powder bed fusion additive manufacturing by combination of machine learning and finite element method: A conceptual framework. Procedia CIRP. 2018;67:227-32.